POLITECNICO DI MILANO
DEPARTMENT OF PHYSICS
DOCTORAL PROGRAMME IN PHYSICS

MULTI-ANALYTICAL APPROACH FOR THE STUDY OF MODERN SEMICONDUCTOR PIGMENTS

Doctoral Dissertation of:
Sara Bellei

Supervisor:
Dr. Austin Benjamin Nevin

Tutor:
Prof. Rinaldo Cubeddu

The Chair of the Doctoral Program:
Prof. Paola Taroni

XXIX Cycle

Abstract

A multi-analytical protocol of investigation for the understanding of optical properties of historical semiconductor pigments was established. The analysis protocol included elemental and morphological microscopy techniques such as high-resolution Scanning Electron Microscopy with Energy Dispersive X-Ray Analysis (SEM-EDX), spectrally- and lifetime- resolved photoluminescence (PL) techniques, and Electron Paramagnetic Resonance (EPR) spectroscopy. Two different type of materials were investigated, both belonging to the class of modern semiconductor pigments.

Lithopone white pigment consists of a coprecipitation of zinc sulfide and barium sulfate ($ZnS + BaSO_4$). ZnS was obtained by chemical process of its primary ore Sphalerite. In Sphalerite, fluorescence usually occurs when specific impurities are present within the mineral. Under the hypothesis that historical lithopones were produced using non perfect synthesis processes, it can be considered that these impurities were not completely eliminated during the manufacturing of the pigment, acting therefore as luminescent inclusions. Multispectral imaging of the PL emission from microsamples revealed the presence of different luminescence centres emitting in the visible spectrum, which we have hypothesized as metal impurities unintentionally introduced into the ZnS crystal lattice during synthesis, which act as deep traps for electrons. The microsecond dynamics of the emission confirmed the trap-state nature of the luminescence centres, reinforcing the hypothesis that luminescence in historical lithopone is due to metal ions impurities embedded into the crystal lattice. EPR confirmed

the presence of Cu^{2+} and Mn^{2+} into ZnS matrix which could not be detected by common elemental analysis such as bulk X-ray fluorescence.

A similar protocol of investigation was applied to the study of a set of seven historical cadmium yellow pigments. Cadmium yellows are modern yellow colors composed of cadmium sulfide (CdS) or cadmium-zinc sulfide ($Cd_{1-x}Zn_xS$). A gradual fading of cadmium yellow from exposure to light and atmospheric agents has been observed on several painting; chemical degradation paths of cadmium colors have been therefore widely studied in the past years. Nevertheless, few studies related with optical properties of historical cadmium pigments. The samples under investigation showed an unexpected heterogeneity of the PL emission when observed under the microscope. Different hypotheses were proposed for the explanation of the observed results. In future, the complex composition of historical cadmium pigments should be taken into account for the understanding of their degradation paths.

The multi-analytical approach presented in this thesis for the study of optical properties of semiconductor pigments encourages further exploration of the same protocol for the study of the intrinsic heterogeneity of other painting materials.

Riassunto

In questa tesi descrivo un metodo di indagine per lo studio delle proprietà ottiche di pigmenti inorganici moderni. Il metodo descritto include analisi elementali e morfologiche quali microscopia elettronica a scansione ad alta risoluzione (FESEM), spettroscopia EDX, imaging di fotoluminescenza, fotoluminescenza risolta in tempo, e risonanza paramagnetica elettronica (EPR). Tale protocollo è stato applicato allo studio di campioni storici di pigmenti moderni di due diversi tipi.

Il litopone è un pigmento, di colore bianco, costituito da un coprecipitato di solfuro di zinco e solfato di bario (ZnS+$BaSO_4$). Le proprietà ottiche del litopone dipendono da quelle del suo principale costituente, il solfuro di zinco, un materiale semiconduttore ottenuto dalla lavorazione del minerale Sfalerite. La Sfalerite si presenta sovente come materiale fluorescente, a causa della presenza di piccolissime quantità di impurezze metalliche drogande. Campioni storici di litopone fluorescente sono stati analizzati seguendo il metodo sopra descritto. Dopo aver implementato un dispositivo per imaging multispettrale di fluorescenza su scala microscopica, ho osservato la presenza di inclusioni luminescenti a diverse lunghezze d'onda in tutti i campioni storici analizzati. Mediante imaging di fotoluminescenza risolta in tempo ho caratterizzato la cinetica di tali inclusioni, confermandone la natura di stato trappola. La spettroscopia EPR, infine, ha permesso di identificare tali centri emettitori come inclusioni di Cu^{2+} e Mn^{2+} nella matrice di ZnS.

Per lo studio di campioni storici di giallo di cadmio (CdS e $Cd_{1-x}Zn_xS$) è stato applicato un metodo di indagine simile, basato sull'osservazione

delle proprietà di fluorescenza dei campioni a livello microscopico. I pigmenti storici analizzati hanno mostrato anch'essi una notevole eterogeneità dell'emissione di fotoluminescenza, caratterizzata dalla presenza di centri luminescenti catalogabili come stati trappola, con caratteristiche variabili al variare della fluenza di eccitazione. Non è stato possibile identificare univocamente la natura chimica di tali centri emittenti, viene perciò discussa in dettaglio la possibile presenza di difetti complessi non rilevabili mediante EPR, e il loro eventuale ruolo nei processi di degrado del giallo di cadmio.

List of Abbreviations

CCD	Charge-Coupled Device
CW	Continuous Wavelength
EDX	Energy Dispersive X-Ray (Spectroscopy)
EPR	Electron Paramagnetic Resonance
FESEM	Field Emission Scanning Electron Microscopy
MCP	Micro Channel Plate
PC	Personal Computer
PL	Photoluminescence
RT	Room Temperature
SEM	Scanning Electron Microscopy
TRPL	Time-Resolved Photoluminescence
XRD	X-Ray Power Diffraction
XRF	X-Ray Fluorescence Spectroscopy

Contents

Introduction

THIS thesis is intended to provide some insights into the optical properties of historical lithopone white ($ZnS + BaSO_4$) and cadmium sulfide yellow ($CdS, Cd_{1-x}Zn_xS$) pigments, with a particular attention to the study and identification of trace impurities and other emitting centres observed under fluorescence microscopy investigation. The works presented in this thesis benefitted from international collaborations with research institutes and infrastructures, which provided access to advanced analytical techniques and expertise. In particular, access to Electron Paramagnetic Resonance (EPR) and Field-Emission Scanning Electron Microscopy (FESEM) facilities was established through an accepted proposal submitted to the Central European Research Infrastructure (CERIC-ERIC) consortium.

A presentation of the research context will be provided in the following paragraphs, together with the statement of the purposes of this thesis, and the structure of the written.

0.1 Modern Semiconductor Pigments

The 19^{th} Century has been a period of huge changes in paint and pigment technology that have seen the introduction of a wide variety of new materials for arts. The flowering of inorganic chemistry, the subsequent chemical industrial expansion, and the parallel growth in mineralogical and metallurgical research led to the discover of new elements such as zinc, cadmium, cobalt, and the optimization of processes by which mineral forms of these

metals could be extracted from the Earth. A new range of synthetic pigments derived from advances in chemistry and modern methods of industrial production. The first modern synthetic pigment produced was prussian blue ($Fe_7(CN)_{18}$.), accidentally formed by colourmaker Dieasbach in about 1704, in Berlin, while experimenting with the oxidation of iron. In the 19^{th} Century cobalt blue ($CoAl_2O_4$), viridian ($Cr_2O_32H_2O$), ultramarine ($Na_6Al_4Si_6S_4O_20$), and cadmium yellows and reds (CdS; $Cd_xZn_{1-x}S$; $Cd(S, Se)$) emerged [1]. In the 20^{th} Century, white pigments such as zinc oxide (ZnO), zinc sulfide (ZnS), and lithopone ($ZnS + BaSO_4$) came to the market and started to be extensively used to replace the toxic lead white. Modern inorganic pigments significantly changed the colour industry. When a new pigment was discovered or synthetized, the first beneficiaries were the building and textile industries. Manufacturers invested huge resources to develop new processes of synthesis for obtaining pigments with a reduced production cost and suitable properties for their specific application. As a result, manufactured pigment compounds soon became cheaper and available in larger quantities than natural inorganic pigments. Artist-quality pigments were usually manufactured later, following improved standards of production, and were characterized by a higher purity, more homogeneous particle size, and reproducibility of the colour between different batches. Synthetic inorganic pigments introduced new shades of colour characterized by brighter, more saturated hues. Together with the first-time use of paint tubes, invented by the American painter John Rand (1841), which brought artists outside their atelier, the introduction of synthetic colors in artist palettes influenced the way artists approached their work, and played a key role in the emerging of new artistic currents such as Impressionism, based on the use of colour, used for "drawing" the motifs without resorting to line. The quality of these new colours depended not only on their chemical composition, but also on their physical appearance, and to a greater extent, on the manufacturing methods. From the material point of view, these compounds are often impure and composites of their precursors; their degradation processes constitute a challenging problem which is of specific interest to heritage conservation science. The use of physical methods of investigation to study modern inorganic pigments has undergone a steep increase over the past years. Their characterization is fundamental for defining proper conservation protocols with a non-invasive approach, and for understanding their manufacturing technology. Nevertheless, analysis of historical inorganic pigments can be particularly challenging due to several factors. Some of those pigments were synthetized following different industrial processes. For example, at least

three preparation methods are known for the manufacturing of the pigment zinc oxide [2] and these processes differ between each other consistently; furthermore, different zinc sources such as metallic zinc or zinc ores could be employed to obtain zinc oxide by oxidation or chemical precipitation. The variety of manufacturing methods led to the introduction of several impurities into the final product; impurities, even if present as traces, can influence the properties of the material and introduce new forms of degradation. The manufacturing conditions such as the pH of the reaction or the temperature in the furnace influenced the final appearance and composition of the pigment, as well as its chemical and physical properties like the crystalline phase. Manufactures sold pigments under ambiguous names, or adulterated their products by adding fillers and extenders to decrease cost, achieving the desired color shade, and increasing pigment's usefulness. In many cases, no correspondence between the commercial name of the pigment and its chemical composition was found. The exact composition of a historical commercial pigment or paint tube is therefore difficult to establish, and even more challenging is the non-invasive identification of a certain pigment mixed in a layer of paint. For all these reasons, there is still a need to establish effective methods able to characterise modern inorganic pigments, preferably in a non-destructive manner.

0.2 Context of the Research Problem

Lithopone is a modern inorganic white pigment composed of a coprecipitate of zinc sulfide (ZnS) and barium sulfate ($BaSO_4$). The first patent for a pigment called lithopone was registered in Belgium by a manufacturer named Leger, although its first commercialization occurred in England by John B. Orr in 1874, under the name of Charlton White or Orr's white [3]. Since that date, numerous improvements in the manufacture of lithopone were made, and several patents for novel processes of synthesis, both in the Continental Europe (principally in Germany, Austria and Belgium) and in the United States were published. The pigment sold under various names such as Ponolith, Beckton White, Jersey Lily White, Oleum White, or Zinc Sulfide White. Since that date, numerous improvements in the manufacture of lithopone were made, and several patents for novel process of synthesis both in the Continental Europe (principally in Germany, Austria and Belgium) and in the United States were published. The pigment was sold under various names such as Ponolith, Beckton White, Jersey Lily White, Oleum White, or Zinc Sulfide White. Lithopone was easy and cheap to manufacture, and non-toxic. For these reasons, the pigment represented

an attractive alternative for paint industry, mainly as interior paint, both as an oil- and water- based paint as an alternative to the toxic lead white. Despite its whiteness, high body, opacity, and hiding power, the pigment never gained a strong reputation in fine arts over its main competitor zinc oxide. The main reason behind lithopone's weak fortune probably was its property of darkening in sunlight, ascribable to a reduction reaction, and subsequent oxidation that produced metallic zinc, catalyzed by alkali metal chloride impurities typically found in zinc sources [3]. Manufacturers tried to elude lithopone discolouration by preparing the pigment from chloride-free zinc sources, until it was discovered that adding small quantity of a compound of cobalt, varying from 0.02% to 0.5% of the zinc content, rendered the pigment fast to light [4]. Despite the capability of producing a light-stable version of the pigment, lithopone's production after 1928 did not improved, probably due to the bad reputation gained, and the contemporary diffusion of titanium dioxide (TiO_2) white. It is believed that lithopone was likely used as a cheap extender for other white pigments like ZnO, or sold under ambiguous names and then involuntarily used by artists. For all these reasons, its usage as an artists' pigment remains nowadays difficult to establish; lithopone therefore has not been widely studied. In 2009 Boselli et al. [5] proposed a method for the investigation of a white pigment discovered in a box containing pictorial materials belonged to the artist Baccio Maria Bacci (Florence, 1888-1974). Micro-Raman analysis reported vibration bands characteristic of ZnS, $BaSO_4$, and ZnO. By means of fiber optics reflectance spectroscopy (FORS) bulk analysis, the authors revealed again the presence of both ZnO and ZnS absorption edges. A further absorption in the red band, ascribable to the presence of cobalt ions inZnS, allowed to confirm the presence of lithopone pigment produced in the late 1920s, mixed with other zinc compounds. Lithopone gained again the attention of researchers in 2012, when an unusual emission from a white pigment was observed during in-situ investigation of Vincent Van Gogh's painting on paper "Les bretonnes et le pardon de pont Aven" [6]. The analysis campaign was conducted with the aid of two different portable luminescence imaging devices for measuring both temporal decay and spectral properties. The white pigment showed an intense luminescence at 520 nm, and a microsecond dynamics typical of zinc chalcogenides doped with metal ions. In 2014, Capua discussed the discovery of fluorescent lithopone on watercolour drawing dated from 1890 to 1905 by the American artist John La Farge [3]. In this manuscript, insight into the historical synthesis process of lithopone and its usage as pigment were given. Data acquired during the investigation campaign on Van Gogh's painting, together with

the studies conducted by Capua, corroborated the hypothesis that historical lithopone pigments were produced using non-perfect synthesis process, and contain metal impurities which can act as luminescent centres. These results highlighted the need for further research into the optical properties of lithopone pigments.
The work presented in this thesis was therefore designed to accomplish three goals: validate the hypothesis that ZnS could give rise to microsecond emission properties observed in paintings, complete the study of optical properties of lithopone, and the design of a protocol of investigation that could be applied in future to heritage materials with similar characteristics.

Cadmium sulfide (CdS) yellows are inorganic pigments from synthetic origin, ranging in colour from orange to a greenish yellow. A natural version of these pigments was sporadically derived from its only mineral source Greenokite during prehistoric times, but it is only after artificial synthesis occurred in the early 18^{th} Century that cadmium sulfides were introduced as artists' pigments [7]. Cadmium yellows appeared in the market starting from the 1840, under different commercial names such as Cadmium Yellow, Yellow Lemon, or Yellow Deep. Due to the excellent tinting power, high chroma, and wide commercial applications including plastics, ceramic, paints and enamels, cadmium yellows have been widely used, and are still in use today. Cadmium yellows can be found in many paintings between the 1880s and 1920s, being particularly appreciated by some of the history's most famous artists such as Claude Monet, Pablo Picasso, and Henry Matisse. [8].

Previous researches on cadmium yellow pigments focused on their identification when present in complex mixtures of paint, and on the understanding of their degradation paths. Cadmium yellow paints are known to discolour under the influence of humidity and sunlight, but the mechanism of degradation is still not clear. With aging, the damaged layer of paint undergoes darkening and fading, leaving a chalky surface behind. Degradation of cadmium yellows strongly depends on their composition, and occurs more frequently in the lighter shades. An exhaustive interpretation of cadmium paint degradation was provided by Pouyet et al. [9] in 2015. Two paintings of Henry Matisse, "The Joy of Life" and "Flower Piece", which presented several alteration in the yellow paint, were analyzed by synchrotron-based micro-X ray spectroscopy and micro-Fourier Transform Infrared spectroscopy (μ-FTIR). The authors suggested that the presence of cadmium carbonate ($CCdO_3$) and other cadmium compounds responsibles of discolouration processes can be ascribed both to photo-degradation and

unreacted starting agents. Luminescence spectroscopy in the visible and near-infrared range has been employed with the aim to differentiate among cadmium pigments on the basis of their spectral features [10]. In 2016, Rosi et al. developed a nondestructive method for the determination of the chemical composition of cadmium-zinc sulfide pigments by exploiting a combination of electronic and vibrational (micro-Raman) spectroscopies [11]. The authors suggested that poorly crystalline CdS is more prone to degradation, and that in general non-perfect synthesis conditions influence the stability of historical cadmium yellows. The non-linear behaviour of the luminescence was previously demonstrated by PL experiments at different irradiance, showing that the capacity of exciting band edge or trap emission depends on the excitation intensity [12]. High excitation irradiance promotes the trap state saturation and allows for observation of the band edge emission, while the emission from the traps is observed at low irradiance.

In the study presented in this thesis, the optical properties of a group of historical cadmium pigments from the beginning of the 20^{th} Century were analyzed using micro-UV photography, PL spectroscopy, and EPR spectroscopy. As in the case of lithopone pigments, it was hypothesized that non-perfectly controlled reaction parameters can introduce defects and disorders in the crystal lattice. Unexpectedly, a great heterogeneity of the luminescence was observed on historical samples for both excitation regimes. Different hypotheses are proposed for the explanation of the observed results.

0.3 Organization of the dissertation

This dissertation is organized as follows. Chapter 1 describes and justifies the methods and techniques used to gather data for the analysis of historical semiconductor pigments and real artworks. For each technique employed, a theoretical background which shows the basic principles of operation, a description of the experimental apparatus used, and a discussion of the data processing models is provided. Chapters 2 and Chapter 3 contain results from analysis of historical lithopone and cadmium yellows respectively. Information about the historical manufacturing of the pigments, as well a detailed review of the specific literature necessary for the understanding their optical properties are described in each chapter. Chapter 4 s dedicated to the study of the fluorescence emission of zinc white painting layer in the Picasso painting "Harlequin" (1927). Chapter 5 contains a more general summary and discussion of the findings, positive and negative aspects of

the employed protocols of investigation, as well as recommendations for future works.

CHAPTER 1

Methods and Techniques

THIS chapter provides an overview of the research methods used for this thesis. Photoluminescence spectroscopy and imaging are the primary techniques employed for the characterization of the optical properties of modern pigments. The first part of this chapter is dedicated to the description of basic principles of photoluminescence and time-resolved photoluminescence spectroscopy and imaging, followed by a description of the experimental apparatuses used. The second part of the chapter shortly describes a range of other research methodologies that were employed as a support of photoluminescence results.

1.1 Photoluminescence (PL) techniques

PL spectroscopy is a contactless, non-destructive method of probing the optical properties of semiconductor pigments. The basic of every PL experiment consists in irradiating the sample with a beam of light (excitation beam) and recording the electromagnetic radiation emitted from the sample with a suitable detector. In semiconductors, the de-excitation process occurs when the material is excited above the forbidden energy gap. Photons

from the excitation beam are absorbed by the material, promoting electrons from the valence to the conduction band which leave excited holes behind. The system, which is now in a non-equilibrium state, releases the exceeding energy to phonons by inelastic scattering. This process is non-radiative, and known as $thermalization$. The system achieves equilibrium by radiative recombination of carriers, which return to the ground state creating photons at energies close to the energy gap E_g. Other radiative decay paths involve electrons excited from an impurity level into the conduction band, or electrons excited from the top of the valence band into an impurity level. The final result of a PL measurement is the emission spectrum which consists, in the most general case, of recorded emission intensity plotted as a function of the emission wavelength. Other features, such as the luminescence quantum yield (the ratio between photons absorbed and photons emitted) and the lifetime of the luminescence (the rate of luminescence decay after optical excitation) depend on the nature and chemical state of the luminophore involved in the transition. Cultural heritage materials, and therefore historical semiconductor pigments, are usually heterogeneous and composites at many length scales; for these materials, different luminous centres contribute to the overall luminescence signal.

1.1.1 Steady-state PL techniques

In steady-state experiments the excitation source is a CW beam of light, and the emission recorded is a time-averaged intensity of wavelength-resolved signal, hence is a steady emission from a system in equilibrium. The basic of a steady-state PL experiment requires a CW excitation source, a detector, and some optics in-between. For the experiments presented in this thesis, a CW laser (UV Ultracompact CrystaLaser) was employed as excitation source. The excitation wavelength at 375 nm was above the bandgap energy of both Zn-based and Cd-based materials (Table 1.1).

Material	E_g (eV) at RT	E_g (nm) at RT
ZnS	3.54 (cubic)	350 (cubic)
	3.91 (hexagonal)	317 (hexagonal)
CdS	2.42 (cubic)	512 (cubic)
	2.3 (hexagonal)	539 (hexagonal)

Table 1.1: *Energy gap (E_g) of ZnS and CdS at room temperature (RT), expressed both in eV and nm.*

The laser beam was sent on the sample through a multi-mode optical

fiber (0.22 NA, 400 μm diameter) passing first through a dichroic 50/50 beam splitter which focused the light on the sample to a spot of 1 mm diameter, at an angle of 45°. The average output power was 495 mW. The emitted light was collected frontally by a 1000 μm fiber optic directly connected to a compact spectrometer (TM-CCD C10083CA-2100, Hamamatsu Photonics). The spectrometer mounted a back thinned CCD image sensor and a 600 grooves/mm grating, suitable for recording in the range 320-1100 nm with a spectral resolution of 6 nm. PL spectra were obtained after automatic background subtraction and correction for the spectral efficiency of the device. Due to the compactness of the whole PL setup, it was employed both as a laboratory system, or carried outside for in-situ measurements.

Multispectral PL micro-imaging and UV photography

Imaging of the PL emission at a microscale was employed for the study of historical pigment samples. In PL imaging, image data of the fluorescence were taken at specific wavelengths across the electromagnetic spectrum following UV excitation. Spectral imaging was performed on pigment samples with the aid of an optical microscope in order to extract information about the spatial distribution of the luminescent centres.

An optical microscope (Leica DMRE) equipped for epi-fluorescence was used. A CW illumination source was obtained by selecting the 365 nm line of a high-pressure mercury lamp with a suitable filter mounted on a microscope cube (ET365/10 and ZT390dclp, Chroma Technology Corporation). The cube mounted a dichroic filter to selectively transmit the emitted light through the microscope. A set of seven band-pass filters from 400 to 700 nm with 40 nm bandpass was used to restrict the passed light to the spectral band of interest (FKB-VIS-40, Thorlabs Inc.). Filters were changed manually after recording every image using 20x or 50x objectives. The images were recorded with a low-noise monochrome CCD camera (Retiga 2000R, QImaging, Canada) connected to a PC. Home-made software allowed to correct for the detector emission, and to reconstruct the colour image of the emission on the basis of the RGB colour space. The spectral emission of each of the filter was assumed as a Dirac delta function peaked on the central wavelength. Sampling pitch for 20x or 50x objectives was respectively of 1.8 and 0.7 μm. After data acquiring, it was possible to extract emission spectra at all points of the field of view with the aid of MATLAB scripts. For simple PL photography on the microscale, a Nikon digital camera was mounted on the microscope using a c-mount adapter for 1/3" chip. Table 1.2 describes the experimental conditions for each class of

material analyzed.

Case of study	Technique	Experimental conditions
Historical lithopones	Multispectral PL μ-imaging	CW Exc@365 nm BP filters (400-700) nm 20x, 50x objectives
Historical Cd yellows	UV μ-photography	Pulsed Exc@355nm or CW Exc@365 nm LP filter 420 nm 20x objective

Table 1.2: *Multispectral PL micro-imaging and UV photograpy experimental conditions.*

1.1.2 Time-resolved PL techniques

In steady-state spectroscopy the sample is irradiated with a CW beam of light; excited states are continuously created and eliminated, and eventually a steady-state is reached where their concentration remains constant. If the sample is illuminated by a short pulse of light, electron-hole pairs are still generated following each flash of light, and then decay to lower energy levels emitting light under the form of photoluminescence. However, the fluctuation of the light source –the intensity of which changes as a function of time– creates a population of luminescent species that also change over time, changing the equilibrium condition of the system. The emission can now be monitored as a function of time, providing a way to measure the kinetic parameters of the system. The decay of the excited state to the ground state is expressed by the following equation:

$$I(t) = I_0 e^{-\frac{t}{\tau}}$$

Where I_0 is the intensity of the emission at the time of the laser pulse, and τ is the lifetime, defined as the average time the system stays in the excited state before returning to the minimum energy state, emitting a photon. The lifetime is therefore defined by the intensity to decrease to $1/e$ (37%) of its initial value I_0. For an exponential decay of a pure compound, the lifetime is equal to the ratio of the quantum yield ϕ by the radiative rate κ:

$$\tau = \frac{\phi}{k_r}; \phi = \frac{k_r}{k_r + k_{nr}} \Rightarrow \tau = \frac{1}{k_r + k_{nr}}$$

Which shows the lifetime dependence on both the radiative (κ_r) and non-radiative (κ_{nr}) processes.

This decay law is based on a first order exponential; in practice, due to the intrinsic chemical complexity of heritage samples, fluorescence decays usually exhibit a multiexponential behaviour. For the works presented in this thesis, PL decay curves were analyzed with multiexponential fits with a maximum of three components:

$$f(x) = \sum_{i=1}^{3} A_i(1 - e^{-\frac{w}{\tau_i}})e^{-\frac{t}{\tau}}$$

Where $f(x)$ represents the decay curve fitted, τ_i and A_i are the lifetime and the intensity of the i^{th} decay component, and w is the width of the experimental gate, which was set by the operator according to the dynamic range of the emission of the sample under investigation. The mean lifetime τ_{mean}, which is the average time a system spends in the excited state, was calculated from the kinetic components by weighing the lifetime over the number of photons originating from each decay path:

$$\tau_{mean} = \frac{\sum_i A_i \tau_i^2}{\sum_i A_i \tau_i}$$

After the fitting procedure, information about the emission dynamics of the sample was obtained. For heritage materials under investigation, the lifetime varied from ps to μs.

Compared to simple luminescence experiments, time-resolved PL techniques provide many advantages in the study of cultural heritage materials. The decay time depends on both radiative and non-radiative de-excitation processes, which both influence the population of the excited state. The measurement of the fluorescence lifetime, providing information about the microenvironment surrounding the fluorophore, unravels changes arising from chemical modification, such as oxidation, ageing, and interactions between different materials, even when such interactions have no measurable effect on the PL spectra. The lifetime is an intrinsic molecular property, and is mostly independent on the concentration of fluorophores, making possible to distinguish the presence of specific emitters even at very low concentration. This is particularly useful in the case of semiconductor pigments which show distinctive long-living emission: lifetime spectroscopy and imaging are valuable tool for their identification and mapping of their distribution in a real artwork even when present in little amount. The study

of the dynamic behavior helps in distinguish between materials in a composite sample, and provides a tool for monitoring chemical modification in a non-invasive way.

Four different TRPL setups were used as part of this work. The four systems represent different approaches which reflected the necessity of measuring materials characterized by dynamics ranging from picosecond to microsecond, at a macro- and micro- scale. The setups are described below in order of development.

Portable setup for Fluorescence Lifetime Imaging at a macro-scale

The portable setup yields images of the fluorescence emission at different delays after the excitation pulse. It was employed for the analysis of artworks conserved in museums or archives, without the need of moving them to the laboratory. The system was developed at the Politecnico di Milano laboratories prior to the onset of this thesis [13].

The apparatus was composed of a pulsed laser system (Q-switched frequency tripled diode-pumped Nd:YAG laser, FTSS 355-50 Crylas GmbH, Berlin, Germany) emitting pulses at λ_{exc} =355 nm of 1.0 ns duration, and pulse energy of 70 μJ. In some cases, the second harmonic of the laser (λ_{exc}=532 nm) was used as excitation. The ns pulse duration allowed to excite materials with a characteristic emission from few ns to μs, which is the typical lifetime range for heritage materials. A small portion of the laser beam was sent to a home-made trigger unit that converted the optical signal into an electric square wave signal, and sent it to a delay generator (DG535 Stanford Research System, Sunnyvale, CA, USA). The delay generator was connected to the input of a detector for time-resolved PL which was composed of a gated-MCP intensifier (C9546-03, Hamamatsu Photonics, Hamamatsu City, Japan) and a mono-colour CCD camera suitable for detection of all photons emitted in the 380-850 nm spectral range (QImaging Retiga 2000R fast, Cooled Mono 12-bit, Surrey, BC, Canada). The delay unit, after receiving the signal from the laser-trigger system, adjusted the time to start with the image capturing of the luminescence decay with a maximum temporal jitter of 0.5 ns. Fluorescence from the artwork was excited with the laser through an optical system composed of a silica optical fiber of 600 μm diameter, 40 m length, and a telescope capable of magnifying the illumination on a circular area of about 25 cm in diameter. The choice of a long optical fiber had two advantages: it allowed an easy synchronization of the electronic gate with laser pulses, and permitted remote access even in difficult measuring conditions. The fluorescence, collected

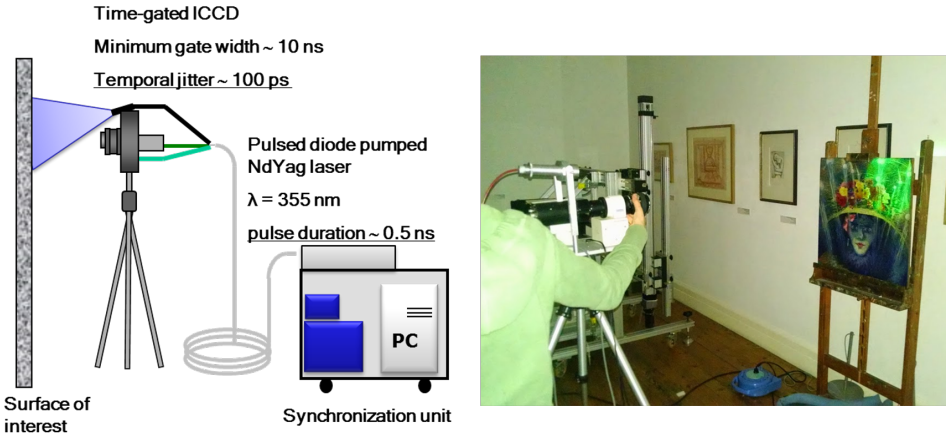

Figure 1.1: *Simplified schematic of the portable setup for fluorescence lifetime imaging (left) and image of the instrument taken during in-situ analysis of futurist paintings at the Estorick Collection of Modern Italian Art, London (right).*

by the gated-CCD unit, was temporally sampled by the image intensifier by electronic closing and opening of a shutter at different delays after the excitation pulses, with a gate width adjustable from 3 ns to continuous mode. A schematic of the setup is given in Figure 1.1. The whole system could be transported in flight cases and assembled directly in the museum on a portable rack of about 60 x 60 x 70 cm.

The final result was a stack of images of the fluorescence taken at selected delays, which were successively processed with C and LABWINDOWS based software. Based on a monoexponential fitting of the decay data, the software reconstructed, pixel-by-pixel, the effective lifetime map (Figure 1.2). Although dynamics of heritage material is never monoexponential, this choice was the simplest for fast data displays, and allowed a qualitative estimation of the lifetimes distribution independently from the intensity of the signal (due to the favorable S/N ratio of a monoexponential fit). Lifetimes on the map were displayed in a false colour representation. The map of the lifetimes allowed a preliminary observation of the differences in lifetime on the investigated artwork, and to discriminate between different emitting materials on the surface of the painting.

Once a preliminary observation of the decay map was completed, the software allowed to extract the decay curve of a selected region of the map for more refined data fitting with MATLAB, according to the theoretical model explained above. It is important to mention that this device is not spectrally resolved since all the photons in the visible spectrum are detected

by the intensified gated-camera. Band pass optical filters were therefore used when only a desired part of the spectrum was selected. The filter was mounted in front of the image intensifier.

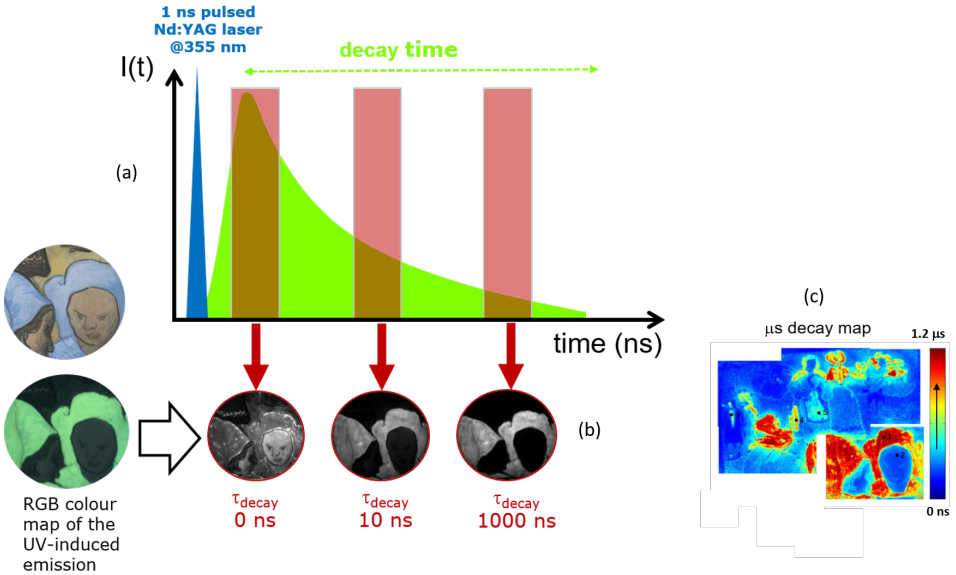

Figure 1.2: *(a) Pulsed laser excitation (in blue), luminescent emission (in green), and operation of the intensifier gate are showed. (b) Meanwhile the intensity of the luminescence decreases in time, images of the luminescence are taken at selected delays with respect to the laser pulse. (c) The effective lifetime map is then reconstructed based on a monoexponential fitting of the decay data.*

Time-resolved PL with the streak-camera system

A traditional laboratory streak-camera system for TRPL spectroscopy was employed for measuring the dynamics of the fast-decay of the energy gap for cadmium yellow pigments. The streak-camera system, in fact, is suitable for the measurement of excited states with lifetimes of less than 10 ns. This facility was implemented at the Center for Nano-Science and Technology @POLIMI, Istituto Italiano di Tecnologia, Milano (Italy).

A typical streak-camera setup is comprised of a detector and a counter, which form together a system that can resolve both wavelength and time. The system acts first as a photomultiplier which converts the photons into electron through photoelectric effect, and accelerates them in a region where an external electric field is present. The electric field is modulated with a

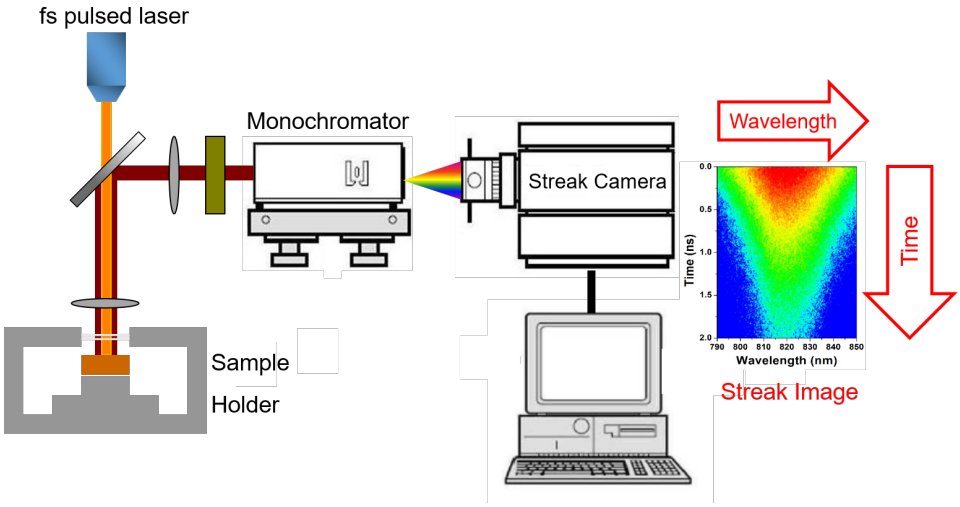

Figure 1.3: *Typical streak-camera setup.*

sinusoidal-varying potential voltage which matches the frequency of the excitation source. The modulation is precisely controlled by a delay generator which receives a small portion of the excitation beam and acts as a trigger. The electron trajectory is therefore modified in a way such that electron arriving in the streak tube at different times are deflected at different angles from the straight path. After passing through a monochromator and a signal amplifier, electrons arrive on a sensor placed at the end of the streak tube and form the so called streak image, resolved in two axes: on the horizontal the wavelength, on the vertical the time. Figure 1.3 presents a simplified schematic of a streak-camera setup.

For the study presented in this thesis, a femtosecond tunable Ti-Sapphire laser (Chameleon Ultra II, Coherent) emitting light pulses of approximately 140 fs over the spectral range of 680-1080 nm was employed as excitation source. The laser had a repetition rate of 80 MHz and a maximum pulse energy of about 50 nJ. The light pulses were focused on a b-barium borate crystal to generate second harmonic, generating an excitation wavelength of 430 nm. The excitation beam was focused on the sample, placed in an epi-fluorescence microscope. The emission from the sample was separated by the excitation pulses by passing through a dichroic mirror (T455lp, Chroma Technology Corp.) and a long pass filter with cut-off at 455 nm (Comar Optics Inc.). The emission was then focused on a monochromator (Acton SP2300 Princeton Instruments, 50 lines/mm grating, 1 nm spectral resolution) and sent to a C5680, Hamamatsu streak-camera system. The

temporal resolution was 2.5 ps when working at 80 MHz operation mode.

Fluorescence Lifetime Imaging Microscopy (FLIM) system

An imaging system which allowed to perform imaging of the fluorescence lifetime under the microscope was implemented. The necessity of developing this system came about during the investigation of historical lithopone pigments, which showed a composite luminescence characterized by several luminescent centres emitting at different wavelengths. It was hypothesized that the characterization of the dynamic behaviour of those emitters could yield new information about heterogeneous features, and the understanding of their origin.

A detailed schematic of the setup is showed in Figure 1.4.

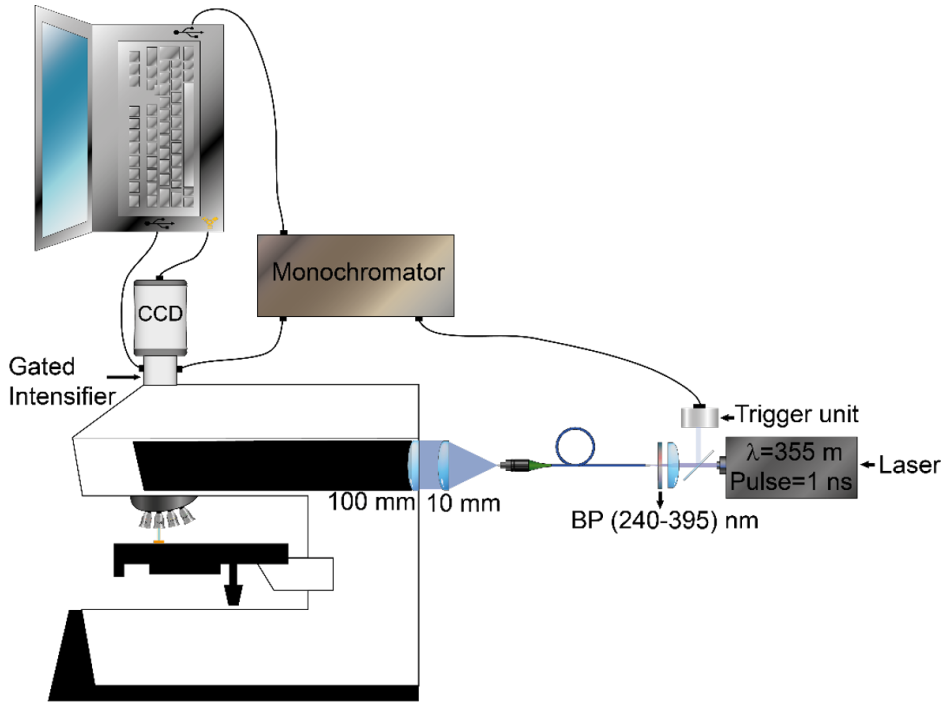

Figure 1.4: *Schematic of the FLIM imaging system.*

The system was composed of the same microscope for epifluorescence employed for multispectral micro-imaging 1.1.1. The laser light, injected into the 600 μm fiber optic, was focused on the objective plane of the microscope after passing through an optical system composed of three plano-convex lenses (focal length=10, 100, and 50 mm) which allowed to uni-

formly illuminate the field of view. The optical system was designed with MAPLESOFT under the thin-lens approximation, the quality of the illumination was required to be independent from the objective chosen; infinity-correction of the objectives was taken into account. After manual optimization of the optical system, uniform illumination just slightly smaller than the objective field of view was obtained. Emission from the pigment samples was detected in a time-resolved operation mode with the same gated-CCD camera system discussed in 1.1.2. The spatial resolution depended essentially on that of the intensifier (57 lp/mm), and resulted in a value of 1.5 μm when the 50x objective was employed. Data processing was operated by clustering similar kinetic emissions in the lifetimes map by image segmentation based on k-means clustering. The decay curves extracted were then fitted with the multiexponential decay model discussed in 1.1.2.

Spectrally- and Time- resolved system for the analysis of kinetics from ns to ms

A further TRPL spectroscopy system based on pulsed excitation, gated-CCD camera, and a monochromator was developed with the aim to provide similar information obtainable with the streak system (i.e. information on both the lifetime and the spectrum) for samples characterized by PL lifetimes from ns to ms. The system was employed for the measurement of the dynamics of the trap states of cadmium yellow pigments. The setup (Figure 1.5) comprised of the same Q-switching laser emitting 1 ns pulses at 355 nm discussed in 1.1.2. The laser was delivered through the 600 μm optical fiber and focused on the sample to a spot size of 1 mm diameter. An optical probe allowed the excitation of the PL signal from sample surface on a circular spot of 1 mm in diameter, with a maximum fluence per pulse of 102 $\mu J/cm^2$ (equivalent to an average power density of 0.1 W/cm^2). The resulting emission from the sample, after passing through some optics, was spectrally resolved in the 380-700 nm range using a monochromator (Acton Research 2300i, focal length = 300 mm, f/4 aperture) and detected by the gated-CCD mounted to the spectrometer. The diffraction grating with 150 lpmm allowed to achieve a spectral resolution of 10 nm. The measuring procedure consisted in the acquisition of a sequential stack of images by shifting the gate window with respect to the excitation. This resulted in a stack of images of the PL emission taken at different delays, and spectrally resolved on the horizontal axis. Following proper calibration of spectral data, and correction for the detector efficiency, spectrally-

and time- resolved data were obtained. Decay spectra were fitted with the multi-exponential model already presented in 1.1.2.

To study the dynamics of the trap states in cadmium yellow pigments, the monochromator was set to λ=650 nm as central wavelength, the luminescence was collect in a spectral window from 450 to 750 nm. A long-pass filter cutting at 420 nm was placed in between the sample and the monochromator to avoid residual excitation from entering the entrance slit of the detector system. A gate width of 1 μs was set, the long-lived decay kinetic was recorded in the first 30 μs.

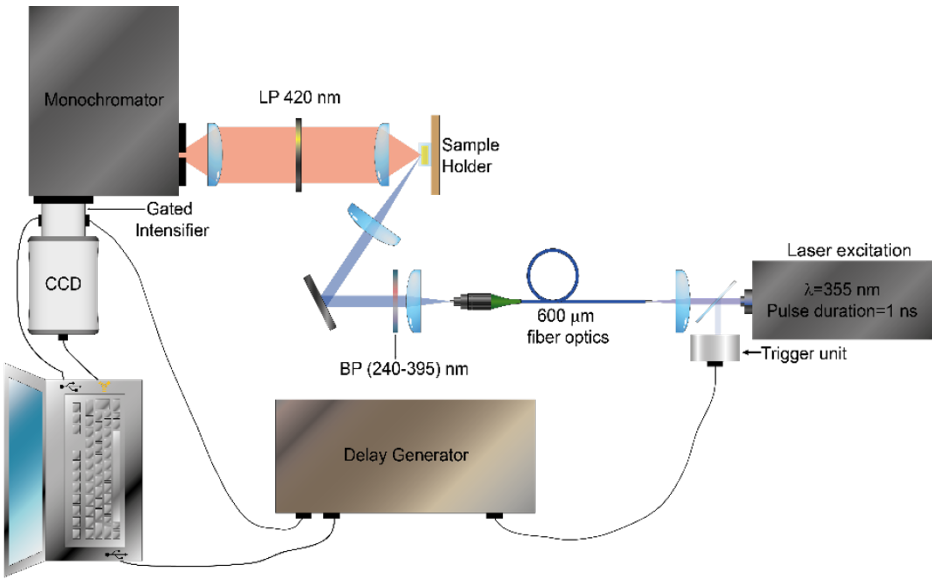

Figure 1.5: *TRPL system based on 1 ns pulsed excitation, gated-CCD camera, and a monochromator for the measure of the dynamic of the luminescence in samples characterized by emission lifetimes from ns to ms. A suitable sample-holder kept the sample vertical which respect to the optical table.*

1.2 Electron Paramagnetic Resonance (EPR) Spectroscopy

PL experiments were performed in conjunction with other techniques which could identify the nature of impurities and defects. EPR measurements were performed in collaboration with two different research groups. Lithopone samples were analyzed at the EPR facilities of the Laboratoire de Spectrochimie Infrarouge et Raman (LASIR), Universite de Lille 1 Sciences et Technologies (France). Historical cadmium yellows were ana-

lyzed at the Research center for advanced ESR techniques (cetRESav) of the National Institute of Material Physics in Bucharest, Romania, as part of the funded project by Central European Research Infrastructure (CERIC-ERIC) consortium. It is not intended to give a comprehensive discussion of the theory here, although the basic principle behind the technique and technical information about the two setups employed are provided.

The basic principle behind EPR spectroscopy is the Zeeman Effect. In 1896, Zeeman observed that when an atom is placed in an external magnetic field, and then excited, the spectral lines emitted following de-excitation process are split into several components. For weak fields, the splitting distance is proportional to the strength of the field, and is smaller than the fine-structure splitting. To explain this phenomenon, quantum mechanics theory and electron spin concepts are required. According to the quantum theory, the electron is a negatively charged particle which possesses an orbital angular momentum L (which make it moving around the nucleus), and a spin angular momentum S (which makes the electron spin around its own axis). The total magnetic dipole moment of an atom $\boldsymbol{\mu}$ is therefore composed of the orbital and spin magnetic moments $\boldsymbol{\mu_l}$ and $\boldsymbol{\mu_s}$ of its optically active electrons. When the atom is subjected to an external magnetic field B_0, the energy interaction between μ and B_0 is be given by:

$$\Delta E = -\mu B_0$$

In the presence of B_0, each of the atom's energy levels is split into several discrete components corresponding to the possible orientation that μ can assume. In a quantum mechanical description, the electron magnetic moments $\boldsymbol{\mu_l}$ can be written as:

$$\boldsymbol{\mu_l} = -g_l \mu_B \boldsymbol{l}$$

where g_l is the electron orbital g-factor (which value is exactly equal to one), μ_B is the Bohr magneton (the magnetic moment for one unit of quantum mechanical angular momentum, $\mu_B = e\hbar/2m_e$) and $\boldsymbol{l}$ is the angular momentum in units of $\hbar$: $\boldsymbol{l}=\frac{\boldsymbol{L}}{\hbar}$. Simmetrically, $\boldsymbol{\mu_s}$ is written as:

$$\boldsymbol{\mu_s} = -g_s \mu_B \boldsymbol{s}$$

where g_s is the electron spin g-factor (approximately equal to two), and $\boldsymbol{s}$ is the spin angular momentum in units of $\hbar$.

In a multi-electron atom, the contributions to $\boldsymbol{\mu}$ are obtained by summing the vector components in the Cartesian space from all the electrons.

If the electronic shells are full, $\sum_i \boldsymbol{l_i} = 0$ and $\sum_i \boldsymbol{s_i} = 0$, therefore the magnetic moment of the atom $\boldsymbol{\mu}$ is equal to zero. The atom is in a diamagnetic configuration. EPR spectroscopy can be employed only for the detection of paramagnetic centres. Many impurities or lattice defects introduce unpaired electrons in the material, and hence paramagnetic species. In the simplest case, the defect involves one electron in the s-orbital, therefore one unpaired spin with no orbital angular momentum is present, and only the spin magnetic moment interacts with the external field. In this configuration, the application of an external magnetic field introduces an interaction energy term described now with the quantistic Hamiltonian operator: $H = -\boldsymbol{\mu_s} \cdot \boldsymbol{B_0}$. By substitution of $\boldsymbol{\mu_s}$, the Electronic Zeeman Hamiltonian is obtained:

$$H_{Zeeman} = g_s \mu_B \boldsymbol{B_0} \cdot \boldsymbol{s}$$

The scalar product $\boldsymbol{B_0} \cdot \boldsymbol{s} = B_{0,x} s_x + B_{0,y} s_y + B_{0,z} s_z$ can be simplified if the field is defined along the z axis, giving $B_0 = B_z$. The quantization of the s_z operator allows only two eigenvalues $m_s = \pm\frac{1}{2}$ so that the Electronic Zeeman Energy can be written as:

$$E_{Zeeman} = g_s \mu_B B_0 m_s; m_s = \pm\frac{1}{2}$$

The originally double spin degenerate spin state $|s, m_s = \pm\frac{1}{2}\rangle$ is therefore splitted in two Zeeman levels with an energy separation $\Delta E = g_s \mu_B B_0$ which is proportional to B_0.

The equilibrium between population n_1 and n_2 of the two Zeeman levels $m = +\frac{1}{2}$, $m = -\frac{1}{2}$ follows the Maxwell/Boltzmann law:

$$\frac{n_1 - n_2}{n_1 + n_2} \simeq \frac{\Delta E}{2kT}$$

Since kT is much larger than ΔE even at low temperature ($kT = 3cm^{-1}$ for T=4K), $n_1 - n_2$ is very small; nevertheless, this small difference in population of the two states, with the population of the lower state n_2 ($m = -\frac{1}{2}$) being slightly exceeding, allows for the EPR signal. The separation of the levels can be matched to a quantum of radiation through the Bohr frequency condition:

$$\Delta E_{Zeeman} = h\nu = g_s \mu_B B_0$$

For a typical strength laboratory magnetic field B_0=0.35 T (3500 Gauss) the value of ΔE is about 0.3 cm^{-1} corresponding to a radiation λ=3 cm

(microwave, or X-band for EPR spectroscopy). When a crystal containing paramagnetic centres is subjected to an external magnetic field, if centres are present in low concentration so that they are non-interacting, the magnetic dipoles align to B_0 according to the presented theory. If the crystal is then subjected to incident electromagnetic radiation, resonance occurs when $\Delta E = h\nu$. At resonance, electrons in the lower level $m = -\frac{1}{2}$ are excited to the upper level $m = +\frac{1}{2}$, while electrons in the upper level transfer to the lower experiencing stimulated emission. As long as the population of the lower state exceeds the population of the upper one, net absorption takes place. The absorption intensity (or, more commonly, its first derivative) plotted as a function of the magnetic field strength results in the EPR signal, and gives information about the electronic configuration of the absorbing center. EPR experiment can be performed in two ways: in the first one, the magnetic field is kept at a fixed strength and the applied frequency is varied until the resonance condition is matched. In the second, the applied frequency is kept constant and the magnetic field is varied. The latter configuration is the most used due to the facility of varying the strength of the magnetic field. EPR spectrum of a real crystal is hence a plot of microwave absorption (at constant frequency) from many paramagnetic centres as a function of the applied magnetic field. Real resonance spectra can be complex, but if they can be properly interpreted, a wealth of microscopic detail is obtained about the defect under examination. More specifically, the symmetry is found, the value of the nuclear spin of a central atom, the nuclear spins of neighboring host lattice atoms, the extent of the localized wave function, the response of a system to the external constraints such as uniaxial stress, etc.

EPR measurement of historical lithopone pigments was performed at the LASIR laboratory, Universite de Lille 1 (France), with the aid of a Bruker E500 facility for CW EPR analysis, operating in the X-band at 9 GHz. All the experiment were performed at room temperature.

EPR measurement of historical cadmium yellow pigments was performed at the cetRESav laboratory, National Institute of Material Physics, Bucharest (Romania) by employing two different facilities for CW measurement: a Bruker EMX-plus instrument working in the X-band (8-10 GHz), at room temperature, and a Bruker ELEXSYS E500Q instrument equipped with E560 ENDOR accessory for measurement in the Q-band at 34 GHz, at T=100 K.

In both cases, samples were prepared by placing a small amount of pigment's powder into a thin quarz tube specific designed for EPR analysis.

1.3 Scanning Electron Microscopy with Energy Dispersive X-ray Analysis (SEM-EDX)

SEM is widely used in heritage science for preliminary observation of the surface of small samples, cross sections, and art's materials because of its capacity to provide morphological and compositional information with a micro-scale resolution, and for monitoring structural changes caused by treatments or deterioration agents.

A SEM unit is essentially composed of two sub-systems: (1) an electron gun, which is a column that produces a narrow, collimated beam of electrons with a precise kinetic energy. The collimated beam is scanned over the specimen surface, and (2) a detector unit which reveals the signal, processes and displays it. The signal consists in a form of energy emitted by the specimen after electron bombardment, which is converted into an electrical signal, amplified, and processed by the detector unit. The resolution of a SEM microscope it is not governed by diffraction as for light microscopes, but depends upon the physics of the electron beam and of the detector unit. In conventional SEM instruments, the electron gun is provided of a tungsten filament cathode which produces an electron beam following thermionic effect when heated at about 2800 °C. Electrons are then accelerated in a high electric field gradient and focused into a narrow beam. The electron beam produced varies in energy from 0.2 keV to 40 keV, and is focused with a condenser system to a spot of about 0.4 nm minimum diameter. The beam is then deflected in two axes to allow raster scanning over a rectangular area of the sample. In field emission (FESEM) setup, a sharp emitter is held at several kilovolts negative potential relative to a nearby electrode. Due to the high potential gradient at the emitter surface, electrons are produced via field electron emission. The electron beam produced is almost 1000 times smaller than in conventional SEM. Compared to SEM, higher resolution can be achieved, clearer, less electrostatically-distorted images are produced, and the spatial resolution, which goes down to 1.5 nm, is at least three times better. When the electron beam interacts with the specimen, a large variety of elastic and inelastic collisions between electrons and atoms within the sample is produced. Different signal are produced including secondary electrons (SE), back-scattered electrons (BSE), X-rays light, and transmitted electrons. Detectors for SE and BSE electrons are commonly present in every SEM setup. SE are generated as ionization products, pos-

sess low energy (below 50 eV) and provide information about the surface orientation (topographic contrast). BS electrons consist of those electrons from the beam which experience elastic collision within the atoms of the specimen, almost without any loss of their kinetic energy. Because larger atoms (with a greater atomic number Z) have higher probability of producing elastic collisions, the number of BS electron produced is proportional to Z. Hence, the brightness of the image formed is proportional to the intensity detected; brighter areas correlate with the presence of atomic species with higher Z, while darker areas with the presence of low Z species. BSE are therefore useful for obtaining high resolution compositional maps, and for distinguish different phases within the same sample.

For cadmium yellow pigments, Energy-dispersive X-Ray Spectroscopy (EDX) was also performed on selected areas of the sample identified during FESEM investigation. In EDX experiments, X-rays are created when the electron beam ejects electrons from the inner shells of the atom, leaving a hole behind which is promptly filled by an electron from an outer shell, emitting the exceeding energy as an X-ray. The energy of the X-ray emitted by the atom is characteristic of its atomic number. A scanning-detector converts X- rays energy into voltage signals, and an analyzer allow to obtain a map of the distribution and relative proportion of elements over the scanned area. Spatial resolution for EDX measurement depends on the size of the interaction volume –and therefore on the accelerating voltage selected– and from the atomic number of the atom specimen involved. The spatial resolution for a traditional EDX setup is on the order of a few microns. The detection limit, defined as the capacity to distinguish a peak from background fluctuation, depends on the specific element detected and on the instrument features over an average value of about 1000 ppm (0.1 wt%).

Table 1.3 provides specifics about the SEM-EDX microscopes used.

Laboratory	Instrument	Sample preparation	Case of study
Dipartimento di Chimica, Materiali ed Ingegneria Chimica G. Natta, Politecnico di Milano	Environmental SEM Zeiss EVO 50 EP equipped with a Oxford INCA 200-Pentafet LZ4 spectrometer	Powders were deposited on a carbon tape suitable for SEM analyses and sputter- coated with a 10 nm layer of gold	Historical lithopone pigments
Faculty of Mathematics and Physics, Charles University of Prague, Czech Republic	Mira TESCAN FESEM with high brightness Schottky emitter equipped with a Oxford EDX spectrometer	Few grains of sample as powder deposited onto carbon tape	Historical cadmium yellow pigments

Table 1.3: *SEM-EDX facilities employed for the experiments presented in this thesis.*

1.4 X-ray Fluorescence (XRF) Spectroscopy

XRF spectroscopy is based on the principle that an atom, excited by high-energy X-ray or gamma photons –called primary X-rays– experiences ejection of photoelectrons from the inner shell and subsequent fluorescent emission of characteristic X-ray radiation (secondary X-rays). The emitted X-ray possesses characteristic wavelength related to the difference in energy ΔE of the initial and final orbital involved in the relaxation process, according to Plank's Law: $\lambda = \frac{hc}{E}$. Similarly to EDX spectroscopy, the fluorescence radiation provides information about the atomic number of the interacting atom. By counting the X-rays of a certain energy emitted, and plotting them over their energy, identification and relative amount of elements from the sample is obtained.

Bulk-XRF measurement was performed on historical pigment samples with the ELIO PORTABLE ED-XRF SPECTROMETER by XGLab S.R.L. Elio belongs to the class of energy-dispersive XRF instruments: it mounts a semiconductor (in this case silicon) detector which receives the emitted fluorescence over the entire spectrum, and decodes it by plotting the number of counts versus the photon energy. It is provided with two lasers, axial and focal, for point easy-positioning and identification, a microscope

camera for monitoring the analysis point, and an external video camera for documentation. The whole setup is light and compact to guarantee transportability for easy in-situ analysis. XRF data were analyzed using free open source PyMca software, and with Elio software. Table 1.4 provides specifics of Elio instrument.

Laboratory	Instrument	Instrument features	Sample preparation	Case of study
Dipartimento di Fisica, Politecnico di Milano	XGLab Elio portable ed-xrf spectrometer	res<135 eV at Mn K-line -Exc. source: X-Ray generator, 5-200 μA, 10-40 kV -Microscope camera (magnified image 2cm x 2cm)	Deposition of few grains of powder into a Teflon cavity	Historical lithopone pigments

Table 1.4: *ELIO portable ED-XRF spectometer.*

1.5 Raman Spectroscopy

Raman spectroscopy is a non-invasive technique based on the interaction between electromagnetic radiation and the vibrational-rotational levels of molecules. When a laser light is incident upon a sample, different scattering processes occur. Beside Rayleigh scattering, which consists in elastic-diffused radiation, a small percentage of the scattered light might be shifted anelasticly (Raman scattering) and therefore be shifted in frequency. At the basis of Raman scattering is the interaction of the incident beam with the vibrational and rotational levels of the molecule, which provokes re-emission of light at different frequencies. The difference in energy between incident and Raman-scattered photons is therefore directly related to the structural properties of the material. As a result, the Raman spectrum consists in a series of peaks of Raman scattering intensity as a function of the Raman shift, which can be considered as a fingerprint that is unique to the material.

Raman analysis on historical samples was performed using a portable Raman spectrometer based on a 785 nm semiconductor laser (Lion, Sacher

Lasertechnik GmBH, Germany), a spectrometer equipped with a 1200 grooves/mm grating (SpectraPro2150, Princeton Instruments, USA), and a front-illuminated cooled CCD (PIXIS 100, Princeton Instruments, USA) working in the 150-1200 cm^{-1} range at a resolution of 15 cm^{-1}. The laser and the spectrometer were connected to the microprobe through optical fibres. Laser light was focused in a 100 μm diameter spot. The power density on the sample was always kept below 500 $\frac{W}{cm^2}$.

CHAPTER 2

Historical Lithopone White Pigments

HISTORICAL lithopone samples were studied through the combination of spectrally- and time-resolved PL imaging and EPR analysis for the characterization and assessment of the presence of specific impurities and defects, which are responsible for the luminous properties of the pigments.

2.1 Historical manufacture of lithopone white pigment

Historical synthesis of lithopone involved the mixing of a solution of barium sulfide (BaS) and zinc sulfate ($ZnSO_4$). The resulting coprecipitate of zinc sulfide (ZnS) and barium sulfate ($BaSO_4$) was then filtered, washed, and dried. This precipitate, generally referred to as crude lithopone, was then calcined at temperatures ranging from 600 °C to 900 °C and subsequently wet milled, filtered, and dried. The annealing process allowed the transformation of cubic ZnS to its hexagonal form. ZnS was present in higher percentages in finest quality lithopone, and could be as high as 32%, although the general proportions were around 30.5% zinc sulfide, 68% barium sulfate, and 1.5% zinc oxide that was also used as filler. The care

exercised in the preparation of the two soluble salts, BaS and $ZnSO_4$, which were prepared in the lithopone factory, influenced the quality of the pigment. $ZnSO_4$ was obtained by reprocessing zinc containing waste materials or directly from zinc ore. In order to obtain $ZnSO_4$, the zinc source material was leached in sulfuric acid, and other metallic impurities were precipitated as insoluble sulfides. The solution obtained was then filtered, washed, dried, and pulverized.

2.2 Optical properites of zinc sulfide

Optical properties of lithopone material depend essentially on the ones of its main constitutor ZnS. ZnS is an inorganic compound. Its primary ore, Sphalerite (historically named Zinc Blend) is the main form of zinc found in nature. Sphalerite crystallizes in the cubic structure and grows commonly as tetrahedral crystals. Pure Sphalerite (ZnS) is white, although it is commonly associated with variable amounts of iron substituting for zinc $(Zn, Fe)S$ which gives a dark grey color. The hexagonal analogue of Sphalerite is less frequently found in nature, and takes the name of Wurtzite. Thermal treatment at high temperature transforms ZnS from its cubic to hexagonal form. ZnS is a semiconductor of the II-VI group with a large, direct band gap of of 3.54 eV (cubic) or 3.91 eV (hexagonal) at room temperature [14]. Its optical properties have been widely studied since ZnS is used as phosphor in several applications, including X-ray screens, cathode tubes, and LEDS [14, 15]. In its pure form ZnS shows luminescence in the blue region, with an emission maximum ranging from 416 to 478 nm assigned to vacancies or interstitial defects in ZnS [16, 17]. When is doped with suitable activator, such as certain transition or rare-earth metals, ZnS extends its range of emission up to the infrared spectrum, with recombination occurring via shallow trap states or via deep trap states of different kinds which are created by the interaction of the doping element with the semiconductor matrix. ZnS with impurities has been widely used as luminescent material, and many references can be found. Blue luminescence can be achieved with aluminum [18, 19] or silver [20–22] doping. Copper is employed to design efficient phosphors emitting in the green band [21, 23, 24]. A strong orange emission is related to ZnS doped with manganese [21, 23, 25]. Eventually, co-dopant agents, such as chlorine [18, 26] can be used to further tune or enhance the emission properties.

2.3 Samples description

Six small jars of historical lithopone were provided by Joseph Barabe from the McCrone Associates in Westmont, Illinois (USA). Very little was known about these samples: they were synthesized in the United States of America, and were originally labelled with the name of different companies, as reported in Table 2.1. A careful research allowed the identification of the region of production, as well as make a rough estimation of the synthesis period. Commercial samples of ZnS and Lithopone were purchased from Kremer Pigmente GmbH&Co. (Germany) as reference standards. Powder from each sample was divided into three portions. The first part was used for bulk analysis; the second portion was adequately dispersed between two layers of UV-transparent silica glass of approximately 40 μm thickness to perform PL microscopy, and the third part was used for EPR analysis.

Sample name	Pigment name	Manufacturer	Geographical location	Manufacturing period
Commercial ZnS	–	Kremer Pigmente GmbH&Co	Germany	Commercially Available
Commercial Lithopone	–	Kremer Pigmente GmbH&Co	Germany	Commercially Available
S1	unknown	New Jersey Zinc Company (now HorseHead Corporation)	New Jersey, USA	1848-1966
S2	unknown	Acme	unknown	>1922
S3	unknown	DuPont	Delaware, USA	>1922
S4	unknown	The Chemical	Delaware, USA	unknown
S5	Ponolith	Krebs Pigment and Chemical Company	Delaware, USA	1902-1929
S6	Ponolith	Krebs Pigment and Chemical Company	Delaware, USA	1902-1929

Table 2.1: *List of samples analyzed with historical information regarding their manufacture, as found on the original bottles.*

2.4 Results

2.4.1 Elemental and morphological characterization

Preliminary bulk characterization of the samples was done with the aid of Raman and XRF spectroscopy. Elemental and molecular signals attributed to lithopone were found: Raman measurement revealed the presence of typical shifts of ZnS (348 cm^{-1}) and $BaSO_4$ (455 and 987 cm^{-1}). XRF measurement revealed the presence of Zn, S, and Ba as the main elements. Trace elements were not detected suggesting that, if metallic impurities are present, their concentration is below the detection limit of the portable XRF analyzer. Representative Raman and XRF spectra of sample S2 are shown in Figure 2.1

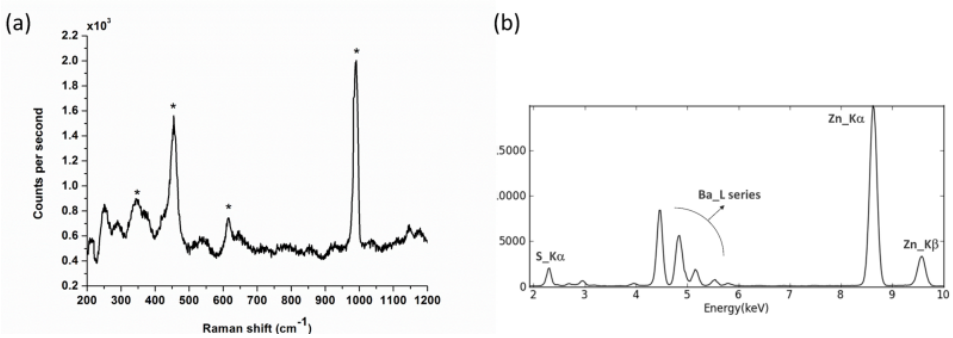

Figure 2.1: *(a) Raman and (b) XRF bulk analysis on a representative historical sample (S2).*

SEM images for all the samples are shown in Figure 2.2. Differences in particle size were observed and attributed to differences in synthesis conditions, which led to the formation of crystals of different sizes. The intimate mixture of white ($BaSO_4$) and light gray (ZnS) particles demonstrates that coprecipitates of different dimensions have been formed, with the largest particles, on the order of 1 μm in diameter, present in samples S1, S3, and S4.

2.4.2 PL characterization

Multispectral PL Microscopy

Preliminary PL bulk measurement on three representative samples are shown in Figure 2.3. PL bulk highlighted a noticeable emission from historical

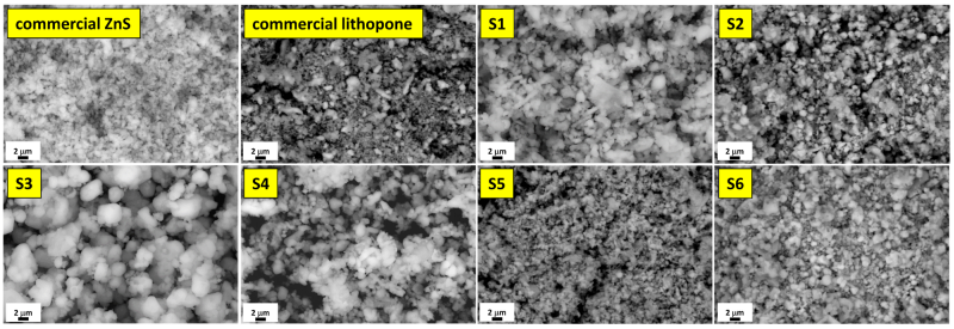

Figure 2.2: *Backscattered Electron images of all the samples analyzed as part of this study.*

samples with a high variability among them. As a general feature, a broad peak at about 520 nm was observed for most samples.

The luminescence properties were better investigated with the aid of PL microscopy. The RGB reconstructed maps of the emission are shown in Figure 2.4. Historical samples presented a very bright luminescence, a uniform emitting matrix, and several localized centres of variable diameter of a few micrometers, emitting at different wavelengths, and distributed over a more uniform and less-intensely emitting matrix. In general, blue (BL, λ= 500 nm), green-yellow (GL, λ= 550 nm), and orange (OL, $\lambda \geq$600 nm) luminescent centres could be clearly detected. In comparison, both commercial samples of lithopone and ZnS showed a less intense emission with only few emitting centres. Strong variations in historical samples are probably due to differences either in synthesis processes or in ores from which the pigments were produced. According to the color of the emission of the matrix and the distribution of impurities, three classes of lithopone were observed: samples S2 and S3 had strong-emitting luminescent centres mainly with maxima in the blue and inthe green-yellow region of the electromagnetic spectrum; samples S1, S4, and S5 were associated with a weakly red-emitting matrix and had small multicolored luminescent centres; sample S6 had a strong blue-emitting matrix and a variety of small emitting centres of different colors.

Time-Resolved PL Microscopy

Time-resolved PL measurements were performed on the same area analyzed with the multispectral PL imaging setup in order to correlate results and characterize the decay kinetics of the luminescence inclusions. The

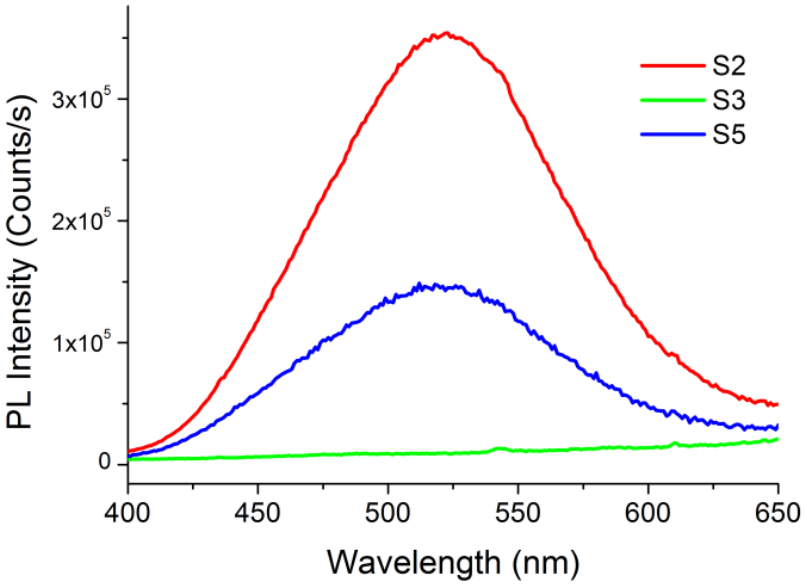

Figure 2.3: *BPL bulk spectra of three historical lithopone sample, with the distinctive broad emission peaked at about 520 nm.*

decay emission parameters of luminescent centres detectable in four samples (S2, S5, and S6, representing the three classes described above, and S4, characterized by a lower emission intensity) have been summarized in Table 2.2.

PL decay curves from two representative samples, S5 and S6, are shown in Figures 2.5 and 2.6, together with reconstructed RGB maps of the color of the emission, the emission lifetime map, PL spectra, and mean decay profiles of clustered emitting centres.

The PL decay curves measured were strongly multiexponential, which indicates the trap nature of the emission mechanism and the existence of a distribution of nonradiative transition paths. All the samples were characterized by the presence of long-lived luminescent centres with an effective emission on the order of microseconds; the longest effective lifetime is always associated with the blue centres. The same trend was observed for all the samples. In sample S5, blue centres showed effective lifetime τ_{mean}=4.14 μs, green centres have τ_{mean}=1.09 μs, and orange centres have τ_{mean}=1.98 μs. The same analysis for sample S6 highlighted a blue luminescent matrix (τ_{mean}=4.57 μs), blue emitting localized cen-

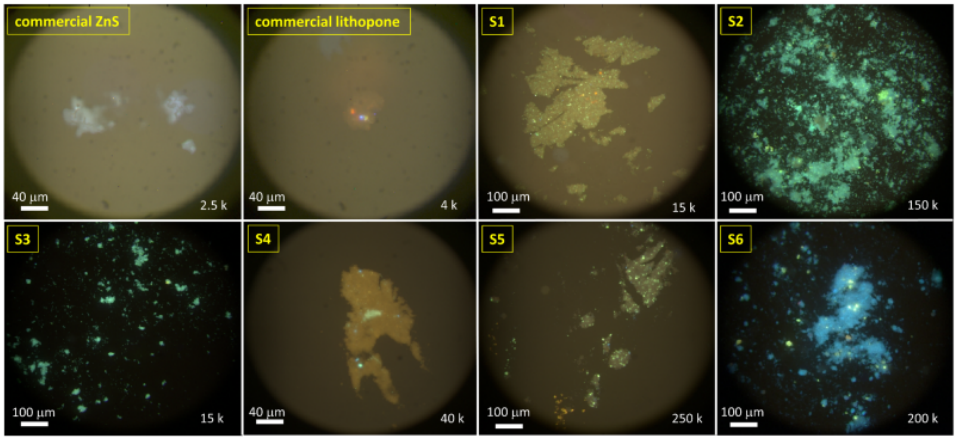

Figure 2.4: *Reconstructed RGB images of the UV-induced PL emission for commercial samples of ZnS and lithopone, and for the six historical lithopone samples (S1-6). At the bottom right of each image, the maximum PL intensity recorded is reported in counts.*

tres (τ_{mean}=5.00 μs), green-yellow emitting centres (τ_{mean}=3.93 μs), and a small cluster of orange luminescent inclusions (τ_{mean}=3.89 μs). In sample S2, BL with the longest measured lifetime (τ_{mean}=5.34 μs) and OL (τ_{mean}=4.29 μs) emitting centres were detected, while in sample S4 BL (τ_{mean}=3.16 μs) and OL (τ_{mean}=2.43 μs) are identified. For these two samples, the analysis of the decay kinetics of the few green-yellow emitting centres gave inconsistent results, suggesting that more centres emitting at different wavelengths are superimposed. The presence of multiple superimposed centres was also found for sample S1.

2.4.3 EPR Spectroscopy

EPR was performed in the attempt of identify external impurities or other paramagnetic centres which might be responsible for the features observed during PL experiments. EPR spectra registered from all historical samples exhibited a small peak at g=4.3, a broad signal around g=2.2, and a resolved hyper-fine pattern centered at g=2 (shown in Figure 2.7(a) for sample S3). Figure 2.7(b) displays a highlight for the g=2 region of the EPR spectrum for two representative samples (S1 and S3).

	$\tau_1(\mu s)$	$\tau_2(\mu s)$	$\tau_3(\mu s)$	$A_1\tau_1(\%)$	$A_2\tau_2(\%)$	$A_3\tau_3(\%)$	$\tau_{mean}(\mu s)$
S2(BL)	0.10	0.93	7.51	7.0	25.1	67.9	5.34
S2(OL)	0.07	0.78	6.92	14.5	26.7	58.8	4.29
S4(BL)	0.02	0.48	5.44	14.7	29.9	55.4	3.16
S4(OL)	0.01	0.45	5.47	28.7	29.3	42.0	2.43
S5(BL)	0.09	0.85	6.56	14.7	25.7	59.6	4.14
S5(GL)	0.03	0.33	5.03	56.8	23.4	19.8	1.09
S5(OL)	0.01	0.42	4.27	27.9	28.8	43.4	1.98
S6(BL)	0.11	0.77	6.90	7.0	23.3	69.7	5.00
S6(GL)	0.05	0.40	5.89	11.8	23.0	65.1	3.93
S6(OL)	0.06	0.43	5.97	12.2	24.4	63.4	3.89

Table 2.2: *Results of analysis of TRPL decay curves fitted with a three- exponential model.*

2.5 Discussion of results

Results obtained during PL and EPR experiments can be explained by considering that Sphalerite is nearly always found with aluminum (Al) resulting from acidic weathering of rock and sulfide minerals, including salts of Mn, Cu, Ag, Cd, and Pb, resulting from mine drainage activity [27]. In order to obtain $ZnSO_4$, the zinc source material was leached in sulfuric acid, and other metallic impurities were precipitated as insoluble sulfides. The solution obtained was then filtered, washed, dried, and pulverized. Due to the impurity of the Zn sources and variability in the preparation of solutions, different metal impurities may have been introduced during various steps of lithopone synthesis. Blue luminescence (BL) centers observed in lithopone samples can be attributed to interstitial Ag and Cu or to intrinsic ZnS defects. Ag substitutes Zn in the matrix and acts as an electron acceptor centre, giving rise to an emission ranging from 420 to 440 nm depending on the presence of coactivators like Al, which usually causes a red-shift of the luminescence [18]. Cu forms two types of acceptor centres in ZnS matrix, and the emission wavelength closely depends on the Cu-doped concentration [26]: the blue-Cu luminescence (BL) peaked at 472 nm is formed by positively charged interstitial Cu^+ ions [Cu_i^+]; Cu_i^+ centres trap electrons from the conduction band, which immediately recombine with free holes nonradiatively. Since the diffusion of Cu into the ZnS matrix is difficult, formation of interstitial Cu_i^+ centres can occur only with an excess of Cu doping. The so-called self-activated emission from crystals of ZnS, ascribed to the presence of intrinsic defects, also gives rise to blue luminescence [16, 17]. A green-Cu luminescence (GL) peaked at 520 nm is formed by Cu substitutionally sitting at the Zn^{2+} site [Cu_{Zn}^{2+}] acting as a

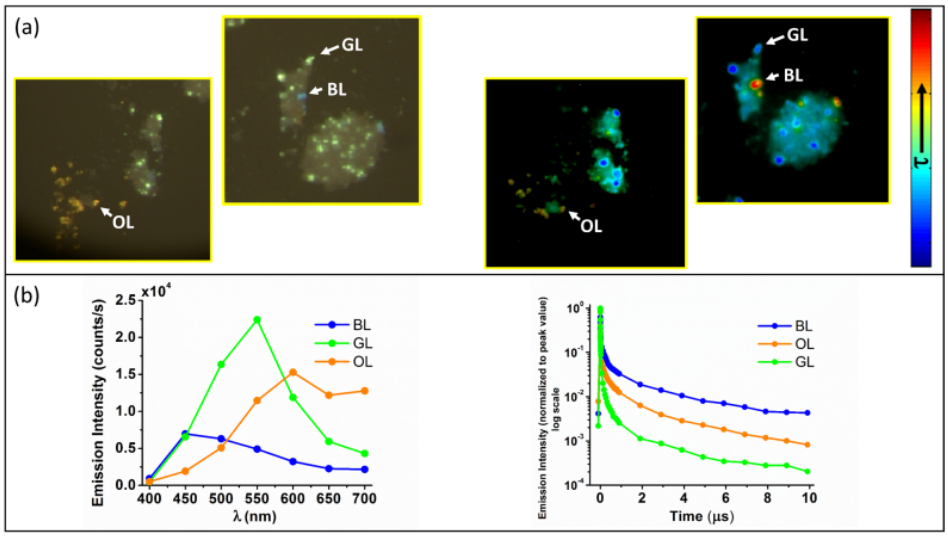

Figure 2.5: *For selected areas of sample S5 are shown: (a) reconstructed RGB maps of the color of the emission, (b) emission lifetime map, (c) PL spectra, (d) mean decay profiles of clustered emitting centres.*

recombination centre for electrons from either conduction band or shallow donor sites (e.g., S vacancies). Green Cu emission can be quenched when the concentration of Cu impurities increases beyond a certain limit, indicated as 3.510^{-4} mol [23], which promotes the blue Cu_i^+ luminescence. Therefore, the ratio between these two peaks may be a good indicator of the concentration of Cu doping. Orange luminescence (OL) arises from the incorporation of traces of Mn^{2+} in the crystal lattice and is peaked at around 580 nm [23]. The mechanism for the orange luminescence from Mn^{2+} doped ZnS is similar to that of Cu_{Zn}^{2+}, but in this case, Mn^{2+} acts as an isoelectronic dopant that substitutes at the Zn valence sites and acts as an attracting site for holes $[Mn_{Zn}^{2+}]$ which therefore recombine with conduction band electrons or electrons in shallow donor sites. PL properties showed a complex behavior that reflected the great heterogeneity (different impurities and concentrations), confirmed by the multiexponential behavior of the luminescence decays. Few studies address the analysis of the dynamics of doped ZnS materials, and most highlight how differences in lattice structure are responsible for marked differences in kinetic properties: Lisensky et al. [28] modeled the dynamics of Cu-doped phosphors as a second-order equation, consistent with the recombination of equal populations of holes and electrons. Jayanthi et al. [24] measured the time-resolved

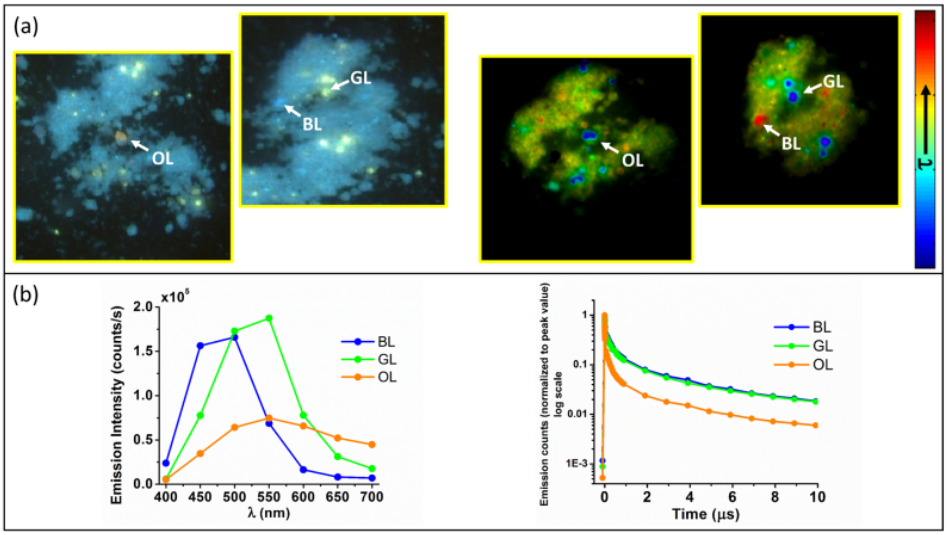

Figure 2.6: *For selected areas of sample S6 are shown: (a) reconstructed RGB maps of the color of the emission, (b) emission lifetime map, (c) PL spectra, (d) mean decay profiles of clustered emitting centres.*

decay of PL for undoped ZnS and ZnS/Cu nanoparticles, suggesting that, beneath the band gap excitation, carrier dynamics involves band to band excitation, trapping at sulfur vacancies, recombination at valence band or Cu level, and conduction band to Zn valence acceptor centres. Chen et al. [18] studied the role of codoping in the variation of the decay constant in Cu-doped ZnS phosphors. Due to the large range of applications of doped ZnS, its kinetic properties can be tuned from a microsecond up to several minutes; therefore, a comparison of time constants reported in this work with literature is not straightforward. As a general feature, the type and concentration of dopants, as well as the local environment of an activator centre, play a key role in determining the optical properties of the luminescence of lithopone, such as the intensity of the transitions and the energy at which the transitions occur. In addition, the environment of the activator may strongly affect the radiative decay time and the nature of the de-excitation mechanism. EPR spectroscopy provided information on some of the structural and dynamic phenomena of lithopone samples and gave insights into impurities that influence their PL properties. The narrow peak at g=4.3 arised from high spin S=5/2 Fe^{3+} species; this peak was found in all samples, therefore the concentration of Fe^{3+} can be considered similar for all samples. Fe is a common contaminant associated with spharelite

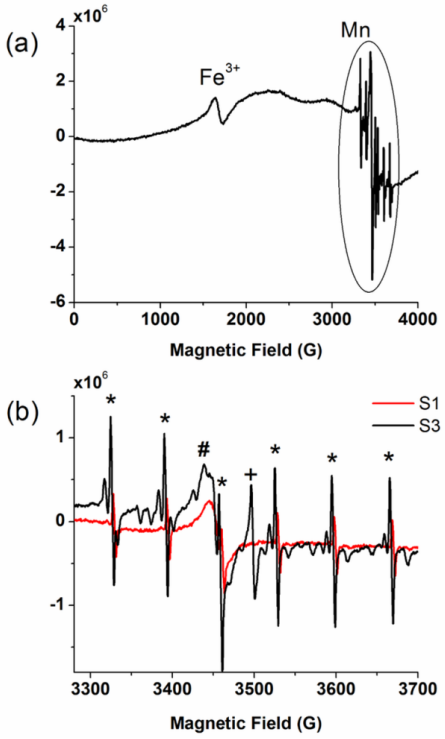

Figure 2.7: *a) EPR spectrum for sample S3; (b) highlight of the g=2 region for samples S1 and S2, which shows the hyperfine pattern centered at g=2.*

with Fe^{2+} substitution for cation lattice Zn sites [29]. The presence of the Fe^{3+} state rather than Fe^{2+} might therefore be due to oxidation of sphalerite [$Zn(S,Fe) + 2O_2 \rightarrow Zn(S,Fe)O_4$] during the grinding process of the mineral [30]. The broad line around g=2.2, observed for all samples, could be ascribed to the presence of trace Cu^{2+}_{Zn}, which was predicted by PL analysis as a justification for the GL. At around g=2, a broad signal superposed over hyperfine structure is consistent with the presence of Mn as a cluster and Mn^{2+} substituting Zn^{2+} sites, which is a reasonable explanation for the OL [31]. This signal, consisting of a complex of six sharp lines, identified as hyperfine structure Mn^{2+}, is due to the interaction of electron spin of Mn^{2+}_{Zn} with its nuclear spin I=5/2. The spectrum further contained a system of lines between each component of the sextet, identified as the so-called forbidden transitions coming from the zero field splitting interactions, when the nuclear spin changes simultaneously with the orientation of the electron spin, due to high spin state of Mn^{2+} species [32]. The other two components, respectively centered at g=2.009 and g=2.002, were at-

tributed to the presence of organic radicals and ZnS defects [33], which might be partially responsible for the blue luminescence detected in historical samples, ascribed to the self-activated emission from ZnS crystals.

CHAPTER 3

Historical Cadmium Yellow Pigments

OPTICAL properties of a set of historical CdS pigments as powder were observed through a combination of photoluminescence (PL) techniques such as spectrally-resolved PL, UV μ-photography, Time Resolved PL, morphological and elemental analysis FESEM-EDX, and EPR. This study has been carried out within the framework of the CERIC-ERIC (Central European Research Infrastructure Consortium) which allowed for access to facilities such as FESEM-EDX (Faculty of Mathematics and Physics, Charles University of Prague, Czech Republic) and EPR (Research center for advanced ESR techniques (cetRESav) of the National Institute of Material Physics in Bucharest, Romania).

3.1 Historical manufacture of cadmium yellow pigments

The natural form of cadmium yellow, Greenockite, is a rare mineral which belongs to the wurtzite group [34]. It is constitutes of cadmium sulfide crystallized in the hexagonal system at high temperatures, and as tetrahedral system at low temperatures. Greenockite is often found associated with other sulfide minerals such as Spharelite $(Zn, Fe)S$. Due to the rarity

of pure Greenockite occurrence, most cadmium is obtained as a byproduct of zinc ores, especially spharelite [35]. Several patents and historical sources document the historical process for the industrial manufacturing of cadmium sulfide as a pigment [36–38]. The standard procedure involved the production of cadmium sulfate by attacking metallic cadmium with acids (such as sulfuric acid) to obtain cadmium salts. Cadmium salts were subsequently precipitated in aqueous solutions together with soluble sulfides until cadmium sulfide (CdS) formed. To achieve lighter and more greenish shades of yellow, cadmium salts were reacted with zinc sulfate ($ZnSO_4$) that was simultaneously added to the water solution, to co-precipitate zinc and cadmium sulfide ($Cd_{1-x}Zn_xS$). The addition of barium sulfide ($BaSO_4$) resulted instead in the formation of a coprecipitate of cadmium sulfide and barium sulfate ($CdS + BaSO_4$) which was called cadmiophone in analogy with zinc lithopone ($ZnS + BaSO_4$). The precipitate obtained consisted of cubic CdS which was not used in the pigment industry due to a lack of qualities such as tinting strength, oil absorption, and brilliance of color. It was only after pH adjustment to about 8.6, filtering, drying and calcinating that a composite pigment with suitable properties as color was produced. CdS properties as a pigment depend on the whole described manufacturing procedure; careful filtering-washing of the aggregate, and subsequent thermal treatment are described by historical sources were the most crucial steps to ensure to the material high quality and reproducibility. Filtering and washing of precipitate made it possible to remove harmful impurities or to extract valuable components that were contained in the pore liquid. Calcination at high temperatures allowed to convert the crystal system of CdS compound from the cubic, to the more stable hexagonal form. Calcination was usually performed in an inert (i.e. non-oxidizing) atmosphere, at about 600 °C. This process is described as complicated and cost intensive, but still essential for the complete transformation of cubic CdS to hexagonal CdS without some of the CdS being oxidized.

3.2 Optical properties of cadmium sulfide

Cadmium sulfide is a semiconductor belonging to the IIb-VIa group. In its cubic form is characterized by a direct, large band gap of 2.42 eV corresponding to 512 nm at room temperature, and Bohr exciton radius of $\sim$3 nm [39]. In hexagonal CdS the band gap width strongly depends on the lattice temperature, with the energy gap $E_g(t)$ monotonically decreasing when increasing the teperature. A value of 2.3, corresponding to 539 nm, is

reported for exhagonal CdS at room temperature [40]. The band gap shifts toward higher wavelengths when zinc is incorporated to CdS, the shift is proportional to the relative Zn amount [11]. Optical properties of CdS have been studied in the past few decades due to CdS reliability for applications in various fields like X-ray detectors, light emitting diodes, window layer for heterojunction systems used as solar cells, photocatalysis, and biological sensors [41–43]. Like others wide band-gap semiconductors, CdS attractively derives principally from the possibility of tuning its emission in the visible-light range. Therefore, CdS as material for optoelectronics is normally used under the form of nanoparticles or nanocrystals due to the possibility of changing their size and shape, which allow to tune their emission properties. Limited literature deals with optical properties of bulk CdS. In CdS and in its alloy $Cd_{1-x}Zn_xS$, the blue-green emission is due to recombination of donor-acceptor pair states lying below the exciton states [44, 45]. While the exciton state photoluminescence has been largely characterized in the past decades, the origin of the luminescence in the red and near-infrared is not well understood. At least two near-infrared emission bands, with values of wavelengths in the ranges 640-710 nm and 680-900 nm, seem to be associated with deep traps states in the band gap arising from vacancies of Cd- and S- [46]. A further band peaked at λ=520 nm related to interstitial sulfur was sporadically observed [47]. In addition to that, optical properties of CdS can be modified by the incorporation of minor amounts of metallic activator, such as silver or copper into cadmium sulfide or zinc-cadmium sulfide host material. When heated at elevate temperatures, these activators enter the crystal lattice of the host material and are responsible for imparting the luminescent properties to the material. Unfortunately, the range of emission bands related to impurities often overlaps with the emission arising from native defects, making the characterization of doped CdS and $(Cd, Zn)S$ extremely difficult. Silver-related defects in CdS crystal have been analyzed with a combination of photoluminescence, photocurrent, and thermally-stimulated current for the study of the diffusion of Ag centres [48]. Ag incorporation introduces an orange photoluminescence band at λ=610 nm that has been ascribed to the creation of acceptors centres following diffusion of interstitial Ag (Ag_i^+) into the CdS matrix and subsequent substitution of Ag to Cd vacancies. A similar diffusion mechanism was observed for CdS doped with copper [49] which substitutes to Cd vacancies as Cu^{2+} and produces a photoluminescence band at around 820 nm in CdS particles. Photoluminescence properties of manganese-doped CdS nanocrystals revealed the appearing of a broad emission in the yellow band (λ=574 eV) characteristic of the Mn^{2+}

internal ${}^4T_1 \rightarrow^6 A_1$ transition in cubic CdS [50]. As a general feature, trap states in CdS, both arising from native defects or impurities, are related to the recombination of free electrons on complex donor-acceptors centres which may involve more than one defect. $Cd_xZn_{1-x}S$ ternary compounds have a wider band gap which can be varied from the one of CdS to the one of ZnS by adjusting the relative amount of zinc. An excess of zinc doping is reported to lead to the formation of zinc aggregates and an increase of the irregularity of the morphology of the precipitate. The zinc excess coalescence is reflected optically by an increase of the absorbance [51]. Rosi et al. presented a non-destructive protocol of investigation for the study of the chemical composition of $(Cd, Zn)S$ pigments from early 20^{th} C through a combination of micro-Raman and UV-VIS-NIR spectroscopy [11]. Quenching of the near band edge emission with increasing content of zinc was observed, which might be due to increased defect density and structural disorder introduced by substitution of zinc in the CdS matrix. Differences in the red to near-infrared spectral properties that could be related to the molar fraction of zinc were also observed. In 2014, the kinetic emission properties of commercially available cadmium-based pigments were investigated for the first time [12]. In this work, a non-linear behavior of luminescence was demonstrated by PL experiments at different irradiance, showing that the capacity of exciting band edge or trap emission depends on the excitation intensity, with high excitation irradiance promoting the trap state saturation and allowing for observation of the band edge emission, while the emission from the traps is observed at low irradiance. All the studies mentioned remarked how a consistent description of luminescence behavior of CdS is not of easy description, depending upon several factors: (1) the number and types of traps present; (2) the competition between the radiative and non-radiative pathways; (3) the contributions to deep trap states from dangling bonds at the crystal surface, which are known to reduce trap emission; (4) the ionization energy of the trap. Fluorescence proved to be very sensitive to small changes and cannot therefore be used alone to establish the complex nature of the emission observed.

3.3 Sample description

Seven historical cadmium-based yellow pigments as powder, dated between 1851 and 1949 conserved at the Courtauld Institute of Art, archival collection, and one cadmium yellow pigment as powder purchased from Kremer Pigmente GmbH, named "Cadmium Yellow n.01, lemon" were analyzed

3.1. Previous finding for the commercial sample [12] allowed to know in detail its elemental composition and kinetic properties. Historical pigments from the same bottles were previously analyzed by Leone et al. at the Courtauld Institue [7] with the aim to the study the deterioration processes after artificial aging. Table 3.1 describes the information found on the bottles containing the historical pigments, as well as the correspondence between the samples number here assigned and the identification number in Leone et al. manuscript.

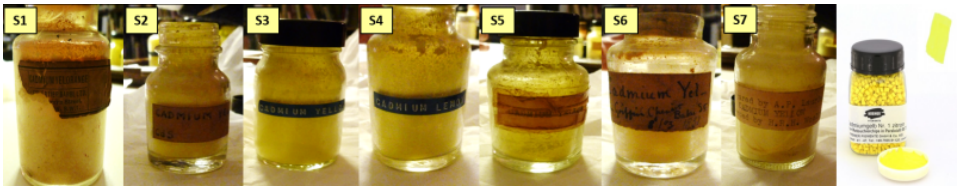

Figure 3.1: *Historical Cd yellow pigments analyzed as part of this study, as conserved at the Courtauld Institute archival collection, and commercial sample commercialized as "Cadmium Yellow n.01, lemon" purchased from Kremer Pigmente GmbH.*

Sample name	Sample name in ref Leone et al. (2005)	Label
S1	9	leomertier barre ltd, London
S2	15	CdS yellow
S3		Cd yellow (blue label)
S4	13	Cd Lemon (blue label)
S5		cadmium yellow
S6	16	"Griffin" 8^{th}/03 1851
S7	14	AP Laurie, 1949

Table 3.1: *List of samples analyzed with historical information regarding their manufacture, as found on the original bottles.*

3.4 Results

3.4.1 XRD analysis

X-Ray Diffraction (XRD) analysis, as reported in Leone et al. manuscript, revealed that all the samples under investigation contained solid solutions of cadmium zinc sulfide in a hexagonal crystal lattice, although a mixed phase can possibly present without being revealed from the instrument. A complete transformation from cubic to hexagonal phase is indicative of a

synthesis process that was performed carefully by control of the calcination temperature and atmosphere.

3.4.2 Elemental and morphological characterization

EDX bulk analysis

EDX spectroscopy was performed with the main purpose to distinguish between samples containing detectable amount of zinc, barium, and for the detection of impurities. Figure 3.2 shows spectra of two representative samples, S2 and S3. Table 3.2 summarizes the elements found for each historical sample.

Sample	Elements Found by EDX Investigation
S1	O, Al, Si, S, Cd, Ca
S2	O, Al, S, Cd, Ba, Cu, Zn
S3	O, Al, Si, S, Cd, Ti, Zn
S5	O, Al, S, Cd, Ba, Cu, Zn
S6	O, Al, S, Cd
S7	O, Al, S, Cd, Cu, Zn
Kremer Cd	O, Al, S, Cd, Zn

Table 3.2: *List of the elements found with EDX bulk analysis performed on historical cadmium pigments.*

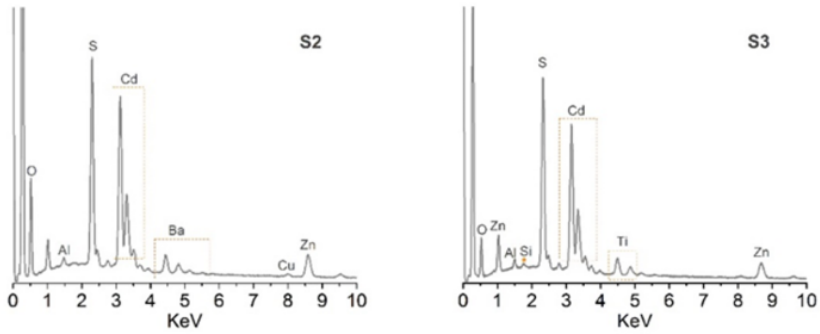

Figure 3.2: *EDX bulk measurement performed on samples S2 and S3*

EDX measurement did not detect zinc in samples S1 and S6. The commercial sample purchased from Kremer Pigmente resulted a mixture of cadmium sulfide with a zinc compound. Considering the light, acid shade of this pigment, $Cd_xZn_{1-x}S$ can be assumed as main constitutor. Samples

S2 and S5 consisted of a mixture of cadmium sulfide, zinc and barium compounds, while sample S3 consisted of a mixture of cadmium sulfide, zinc, and titanium. Rather unexpected results related to the presence of aluminum, silicon, and copper in every sample, and the presence of calcium in sample S1.

FESEM-EDX imaging

FESEM microscope working in at 30 kV allowed to achieve a spatial resolution of 1.0 nm which enabled to visualize samples morphology at a microscale. Figures 3.3 and 3.4 show images of the samples, taken at two different magnifications.

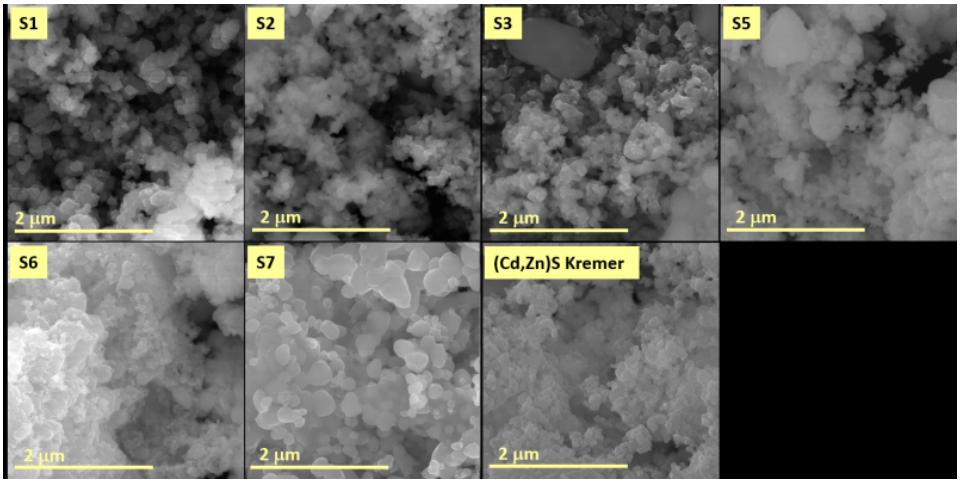

Figure 3.3: *Backscattered Electron (BSE) images of cadmium sulfide pigments at low magnification.*

At a first observation, significant variations in size, texture and morphology between the samples were revealed under SEM microscope. All the samples were characterized by aggregates of irregularly shaped grains of various size. These features might suggest that crystals formed after a fast precipitation, and attest the difficulties in controlling the syntheses process which are often reported in historical handbooks and patents describing the manufacturing of Cd-based pigments. Samples S1, S2, S3, and S5 showed similar morphology and dimension, and were characterized by the most regular grains in size. Sample S6 consisted of aggregates of coarse grains and smaller indistinguishable entities. The largest grains were observed for sample S7. The commercial sample was composed of

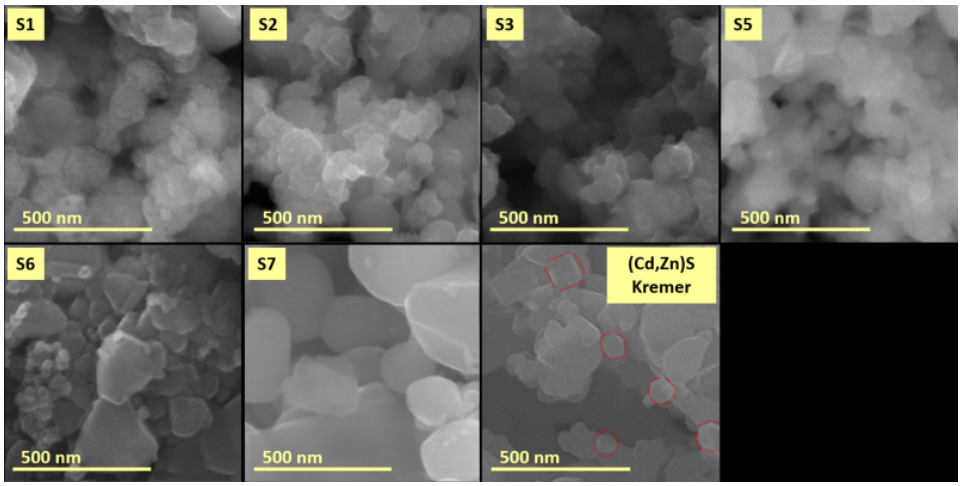

Figure 3.4: *Backscattered Electron images (BSE) of the same samples taken at the maximum magnification achievable*

very small and sharp particles. Figure 3.4 shows the same samples under a bigger magnification. Under this condition, more information about the morphology of single grains were obtained. Observation of the crystal geometry of single particles was possible for the commercial sample. Both squared and hexagonal geometries were observed (the edges of the particles have been enhanced with red contour) suggesting that the annealing treatment did not completely converted between the cubic and hexagonal crystal phases. Samples S1, S2, S3, and S5 still appeared very similar, all composed by roundish particles that seem to share hexagonal geometry. Nevertheless particles in S1 have less defined edges and are characterized by a more granular surface. Sample S6, containing a greater variety of entities, appeared at this magnification composed of few rod-shaped entities and irregular tetrahedrons surrounded by additional aggregates of fine particles fused on the surface of the bigger grains. Sample S7 was confirmed to be composed of more distinguishable grains with a spherulitic morphology, smooth surface, and defined edges. EDX elemental mapping for all the samples helped visualization of the distribution of different elements. In this regards, the most interesting samples were S2 and S5, both containing barium, and S3, which contained titanium. Figures 3.5 and 3.6 show elemental maps of chosen elements for samples S2 and S3.

Elemental maps for sample S2 showed a uniform distribution for sulfur, zinc, and cadmium, suggesting that coprecipitation of zinc and cadmium sulfide occurred, leading to the formation of $Cd_{1-x}Zn_xS$ compound. Bar-

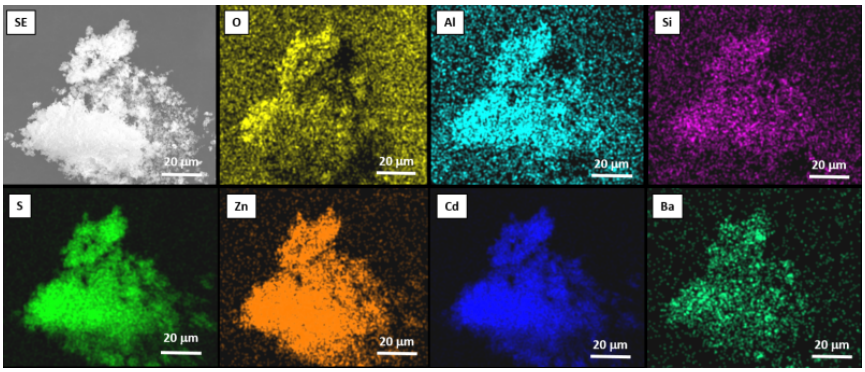

Figure 3.5: *EDX mapping of selected elements for sample S2*

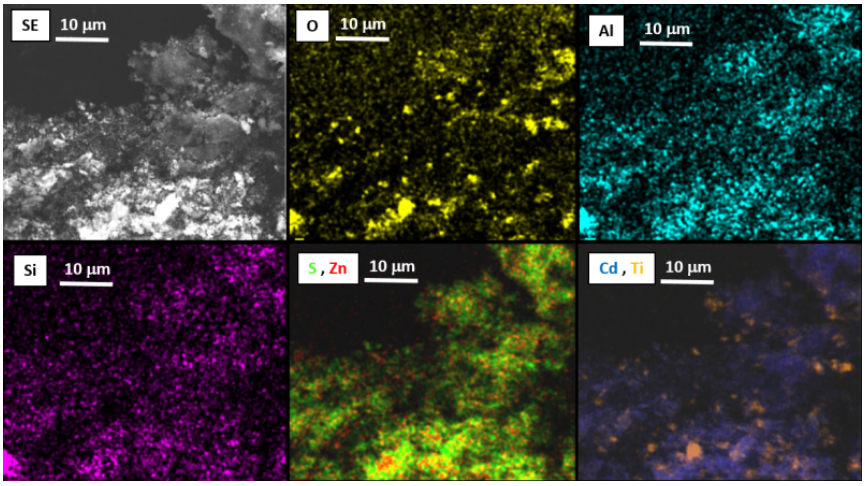

Figure 3.6: *EDX mapping of selected elements for sample S3*

ium map showed instead a nonuniform, leopard-spot like distribution of this element, which leaded to the hypothesis that barium sulfate was added separately as a pigment extender, rather than being coprecipitated as cadmophone. The same features were found for sample S5. The elemental map of oxygen displayed a thickening of this element concentration on the left border of the grain, suggesting that oxidation of the cadmium-zinc sulfide matrix occurred. Aluminum and silicon seemed uniformly distributed all over the $Cd_{1-x}Zn_xS$ matrix. Nevertheless, as these two elements are present in a very low amount even for bulk EDX analyses, no suppositions about their origin and effective distribution could be made. Sample S3 showed similar results, with sulfur, zinc, and cadmium being intimately mixed, and titanium being present as concentrated agglomerates that correlate very well

with the oxygen map, suggesting the presence of titanium dioxide TiO_2 as pigment extender, probably used with the purpose of achieving a lighter shade of yellow. A more careful observation suggested the strong correlation between oxygen, aluminum, and silicon, which might indicate the presence of aluminosilicate (Al_2SiO_5) compound coprecipitated together with the Cd compound. Amorphous aluminum silicate is employed by pigment makers as a white filler in emulsion paint, to increase opacity of the final product. It is often found as a replacement or together with titanium dioxide, which might explain the evidence of the presence of both compounds in the investigated sample. As a matter of fact, no evidence of a strong correlation between silicates compound and the raw geological materials used as reactants for the synthesis of Cd-based pigments could be find in the literature.

3.4.3 PL characterization

Reflectance and LIF spectroscopy

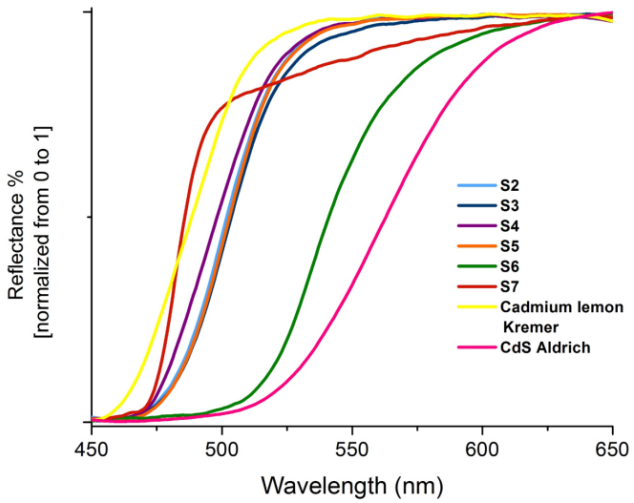

Figure 3.7: *Reflectrance spectra of historical pigments and two commercial references (Cd yellow from Kremer, and chemical grade CdS from Aldrich).*

Figure 3.7 shows the diffuse reflectance spectra, measured at room temperature, of fluorescent samples (all the samples except S1). A further commercial sample of chemical grade CdS (named CdS Aldrich) was measured

as reference spectrum from pure CdS signal. XRD, performed on this sample, revealed its amorphous nature.

The diffuse reflectance spectra in the visible region showed the typical semiconductor sigmoidal shape. The absorption edges of all the samples shifted towards longer wavelengths with compared to the pure grade CdS. This result might confirm that sample S6 contains solid cadmium-zinc sulfide in traces. After performing first derivative calculation of the reflectance spectra (Figure 3.8) two distinct absorption edges appeared for the commercial sample from Kremer (curve in yellow), while the spectrum of sample S6 resulted to be slightly non-symmetrical. Coexistence of two distinct emitters was hypothesized for this two samples.

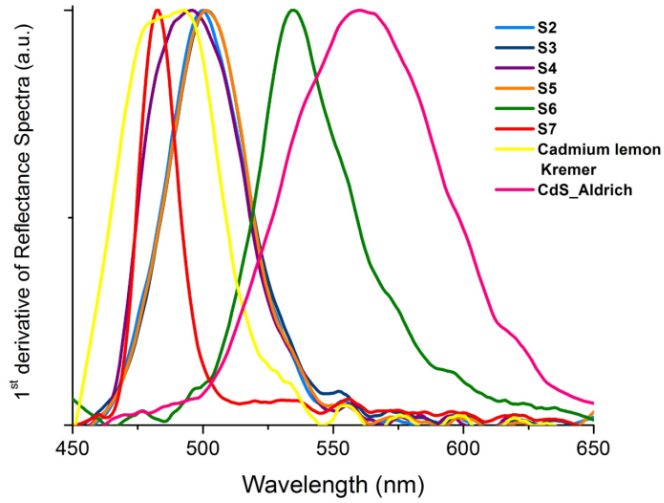

Figure 3.8: *First derivative of reflectrance spectra of historical pigments and two commercial references (Cd yellow from Kremer, and chemical grade CdS from Aldrich).*

LIF spectroscopy was performed by exciting the luminescence with two different laser sources: a pulsed-laser working at 355 nm (Figure 3.9) and a CW-laser operating at 375 nm (Figure 3.10). Commercial sample of pure CdS purchased from Aldrich did not show luminescence signal, which might reflect the amorphous nature of this sample.

The two set of spectra measured under different laser excitation appeared very different from each other. Figure 3.9 shows luminescence emission at energies comparables with the emission from the energy gap.

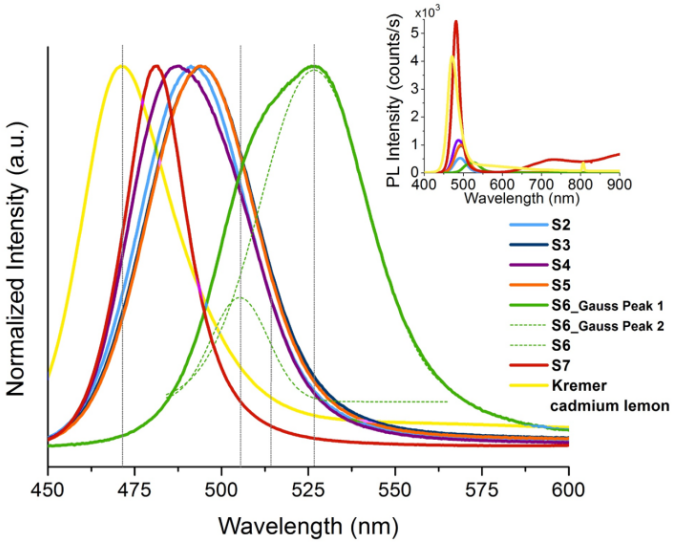

Figure 3.9: *Normalized PL spectra of Cd pigments (pulsed laser at 355 nm). Non-normalized spectra are shown in the small inset.*

As reported by Cesaratto et al. [12], when the sample is illuminated with a highly energetic beam saturation of the trap states is induced, allowing for the observation of the band edge. The separation between the maximum peaks probably reflects the differences in the amount of zinc, with the light-yellow commercial pigment from Kremer owning the larger optical band gap, and emission from sample S6, a yellow/orange with zinc present only in traces, shifted to lower energies compared to the others. The asymmetric spectrum of the band edge emission for sample S6 was fitted with a multi-peak Gaussian which revealed two distinct peaks at 505 nm and 527 nm, supporting the hypothesis of co-existence of two different crystalline phases which gives rise to distinct band edge emissions. Non-normalized spectra (Figure 3.9 inset) revealed a great difference also in term of intensity of the near band edge emission. In particular, the commercial cadmium yellow from Kremer and historical sample S7 (Laurie Cadmium Yellow, 1949) showed a distinct, bright luminescence signal. Emission from sample S7 consisted of a narrow, symmetric band edge peak, and two broad signals in the red and near-infrared region which are ascribable to the emission from the trap state. As reported in Leone manuscript [7], the manufacturer Arthur Pillans Laurie in his handbook "The pigments and mediums of the old masters" (1914) recommends to precipitate cadmium sulfide from sulfate and

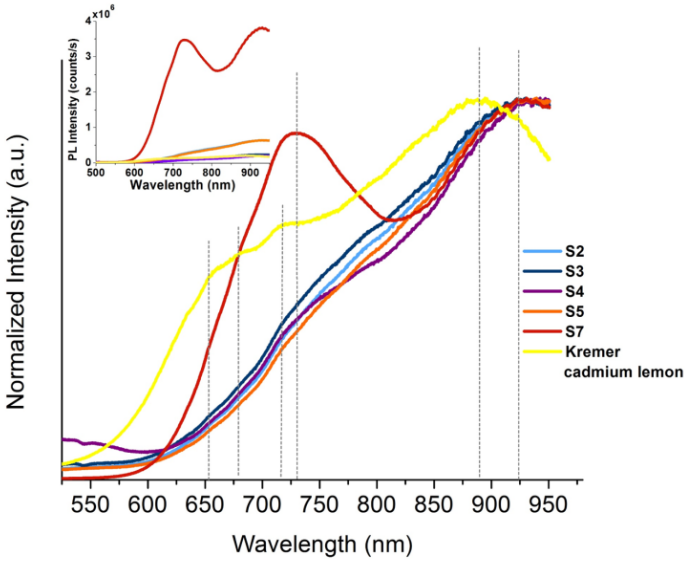

Figure 3.10: *Normalized PL spectra of Cd pigments (CW laser excitation at 375 nm). Not-normalized spectra are shown in the small inset.*

sodium thiosulfate. Leone et al. argued that an improper washing during the manufacturing process of this sample might have left residual impurities which are responsible of the bright fluorescence observed. No evidence of the presence of sodium was found in our studies; nevertheless, noticeable differences in sample S7 morphology compared to the other samples were observed, with sample S7 constituted of well-formed grains of a bigger, homogeneous size. A better crystallization might therefore be responsible for the enhanced optical properties of sample S7. The emission from the trap states was observed at low power density exciting the luminescence with a CW laser at 375 nm operating at average power of 495 mW (Figure 3.10). All the spectra are characterized by red to near infrared emission bands. As already discussed, it is not possible to exploit luminescence spectra for the univocal determination of the emitting state associate with a particular luminescence profile due to the overlap of the emissions arising from trap states of different nature. The signal observed can be assigned to crystal defects, surface defects or external impurities. Looking at the non-normalized spectra (Figure 3.10 inset) a great difference in term of intensity of the signal could be observed for sample S7, which showed a brighter emission also in this regime of excitation. The same sample was characterized by two distinct peaks, one at 729 nm and the other at 922 nm, with almost the

same relative intensity. Cadmium pigment Kremer presented five distinct peaks at 655 nm, 681 nm, 717 nm, 729 nm, and 889 nm, with this last peak blue-shifted of around 36 nm compared to historical samples. Samples S2, S3, and S5 presented instead very common features, with several small peaks between 600 nm and 800 nm, and the same, distinct dominating emission at 924 nm. Finally, sample S4 showed a more pronounced emission below 600 nm. Sample S6 did not show any detectable signal in low-power regime.

UV photography at a microscale

UV photography was performed in the attempt to visualize inhomogeneity in the luminescence emission, and therefore to draw more information about their optical properties. Following the same protocol developed for the investigation of Zn-lithopone pigments, Cd-based samples were prepared for being analyzed under the microscope by inserting few grains of pigment powder in-between two discs of micrometric silica glass. UV photography was then performed by exciting the luminescence with a pulsed laser working at 355 nm first and then, by careful repositioning of the sample in a way to illuminate again the same area, with a CW mercury lamp working at its 365 nm line. Images were taken with a 20x objective, which resulted a good compromise between a good magnification capable of revealing new optical features, and an acceptable focus depth. UV μ-photography for the two different excitation regimes are shown in Figure 3.11.

The upper row of Figure 3.11 displays luminescence excited with pulsed UV laser. Compared to bulk analysis, interesting features could be noticed at microscale. Samples S2, S3, S5, S7, and the commercial pigment from Kremer displayed a fluorescent blue matrix arising from the band edge emission. While the fluorescent matrix seemed to be reasonably homogeneous for the commercial pigment and for samples S5 and S7, small luminescent centres emitting in the blue and green region, could be clearly distinguished for samples S2, S3, and S4. A different situation characterized sample S6. In this case, the emission from the matrix could be described as being composed of two distinct contributors ranging in the scale of green emission. This result agreed with the observation of two different peaks, one at 505 nm and one at 527 nm in the spectrum of fluorescence from the bulk material. The bottom row of Figure 3.11 displays the luminescence from the same area of the samples following CW excitation. As expected, under this regime no emission was recorded for sample

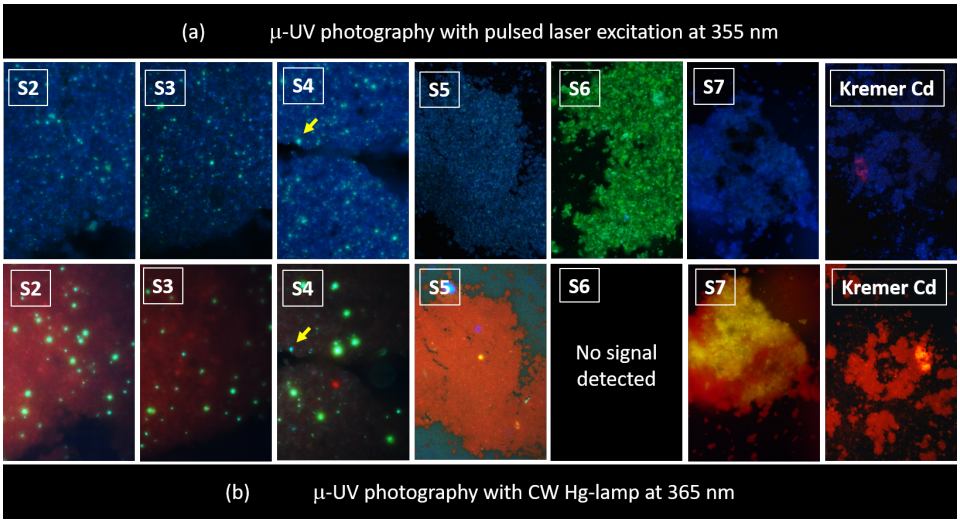

Figure 3.11: *micro-UV photography of all the emitting samples taken at different excitation regimes.*

S6. For the remaining samples, the blue-emitting matrices converted to red-emitting matrices at different intensities. Similarly to what observed in the upper row, samples S2, S3, and S4 were characterized by the presence of several, uniformly distributed luminescent centres emitting in the blue and green, particularly bright in the case of sample S4. Unlike lithopone samples, which showed the same microscopic features when excited with the mercury lamp and with the pulsed laser employed for time-resolved analysis, in the case of the historical cadmium-yellow samples the same consistency did not interested the most part of the emitting centres, with the exception of few features which could be observed in both pulsed and CW regime (for example, the blue emission pointed by a yellow arrow in sample S4). Finally, very few luminescent centres characterized by a peculiar shade of yellow could be observed for samples S5 and S7, while almost no inhomogeneity was noticed for the commercial sample.

TRPL

TRPL analysis was performed with the aid of two different setups. The first one, composed of a streak camera-based detection system and a Ti-Sapphire femtosecond laser as excitation source was employed for the study of the short kinetic of the near band edge emission (1.1.2). The second setup, based on the gated-intensified CCD camera, allowed for the investi-

gation of the long-lived kinetics of the trap states (1.1.2). The decay properties of the near band edge emission are summarized in Table 3.3. For the commercial sample, data have been extracted from the study by Cesaratto et al. [12].

Sample name	λ_{peak} (nm)	τ_{mean} (ps)
S2	490	35
S3	490	32
S4	λ_1=477	τ_1=30
	λ_2=498	τ_2=32
S5	490	34
S6	λ_1=506	τ_1=17
	λ_2=526	τ_2=20
S7	482	21
Kremer Cd	476	3.8

Table 3.3: *Results of analysis of the fast (ps) TRPL decay curves for Cd yellow samples.*

The band edge emission was characterized for all the samples by a short average lifetime of the order of ps, as expected for exciton transitions. Results obtained for the historical pigments showed a significant increase of the average lifetime compared to the commercial sample. Therefore, the dynamics of the band edge might be related to the presence of oxidation states responsible for the increasing of the average lifetime. Two distinct peaks, which can be ascribed to two different cadmium compounds present in the crystal, were measured for sample S4 and S6. This result was expected for sample S6, but did not find any correspondence with previous optical analysis for sample S4. The dynamics of the broad-band emission in the red and near-infrared region was investigated at a longer acquisition mode. Figure 3.12 shows the PL spectra (left) and decay curves (right) recorded with a 1 μs gate width in a large temporal window of 0-30 μs. The time-resolved PL curves were then fitted with a three-exponential model. Lifetime (τ_i) and relative weights ($A_i\tau_i$) of the three components, and average lifetime (τ_{mean}) values extracted for all the samples are displayed in Table 3.4.

Under this regime of excitation, all the samples exhibited a long-living luminescence of the order of microsecond characteristic of a distribution of trap states. Samples S2 and S3, which were found to share similar morphology and PL spectra, showed almost coincident kinetic components. Historical samples S5 and S7, characterized by a more uniform emission with very few inhomogeneity observed under the microscope, showed a longer lifetime and a predominance of the longest component. The commercial

	$\tau_1(\mu s)$	$\tau_2(\mu s)$	$\tau_3(\mu s)$	$A_1\tau_1(\%)$	$A_2\tau_2(\%)$	$A_3\tau_3(\%)$	$\tau_{mean}(\mu s)$
S2	<0.01	1.87	14.6	6.71	46.9	46.4	7.73
S3	<0.01	1.93	12.9	6.71	45.5	47.8	6.96
S4	<0.01	2.03	15.7	3.99	37.2	49.4	9.98
S5	<0.01	2.16	17.3	3.65	30.2	68.1	12.5
S7	<0.01	2.29	17.2	2.50	30.0	67.2	12.2
Kremer Cd	<0.01	4.15	28.8	29.9	52.4	52.4	16.5

Table 3.4: *Results of analysis of the long (μs) TRPL decay curves fitted with a 3-exponential model*

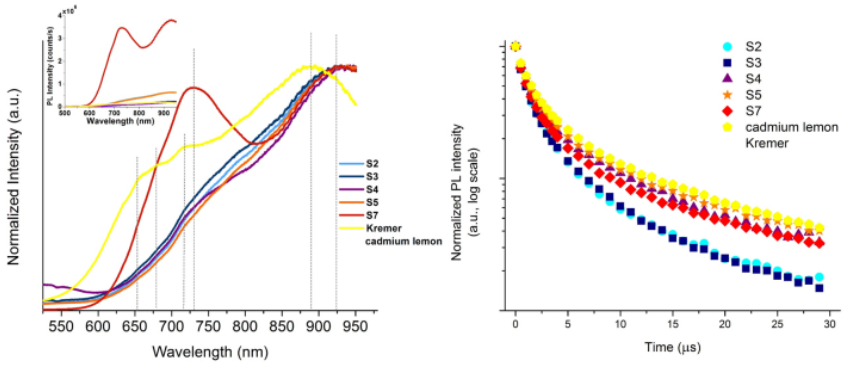

Figure 3.12: *PL spectra (left) and decay curves (right) recorded with a 1 μs gate width in a large temporal window of 0-30 μs.*

pigment exhibited the longest average lifetime.

3.4.4 EPR

EPR was performed in the attempt of identify the presence of external impurities or other paramagnetic centres which might be responsible for the features observed with fluorescence techniques. Due to the limited amount of time dedicated to the experiment, only three representative historical samples (S3, S6, and S7) were chosen. Sample S3 consisted of a co-precipitate of $(Cd, Zn)S$ with small amount of titanium dioxide. Sample S6 is nominally composed of CdS only, although presence of zinc in traces was found through XRD analysis. Sample S7 showed a distinct, bright luminescence, and no significant heterogeneity was reported by micro-UV photography. The commercial sample from Kremer was also analyzed as reference. Luminescent analysis was conducted at 8-10 GHZ (X-Band), and 35 Ghz (Q-band). Figure 3.13 shows the results for historical samples. A very weak Mn^{2+} signal with $A = 9.4$ mT was observed in all the spec-

tra. The signal was simulated at $g = 2.0011 \pm 0.0002$, and does not matches signal of Mn ions in CdS matrix.

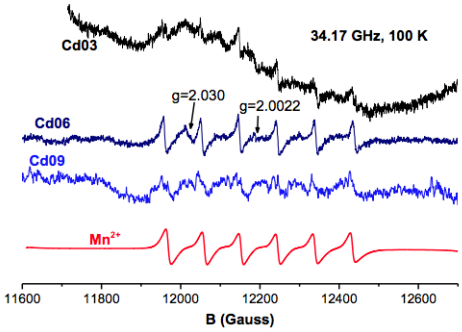

Figure 3.13: *comparative Q-band EPR spectra for samples S3, S6, and S9, measured at 100 K, together with a simulation of the Mn^{2+}spectrum.*

For sample S3 further signals were detected by operating in the Q-band at 100 K: a very weak signals at g=4.3, g=3.4 (probably isolated Fe^{3+}), an intense and broad signals at g=2.486, and a broad signal in the g=[2.17-2.09] range (Figure 3.14).

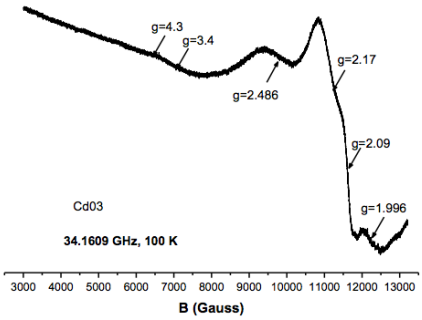

Figure 3.14: *Q-band EPR spectrum of the S3 sample measured at 100 K.*

Reliable reference data to match the strong signals could not be found. The closest g-values found were for Cu or Fe clusters in organic compounds. Sample S7 resulted very difficult to measure, probably due to a higher electrical conductivity. The commercial pigment from Kremer showed a further Mn^{2+} signal at A=6.9 mT in addition to the Mn^{2+} signal at A=9.4 mT observed for all the samples (Figure 3.15). The additional signal, simulated with $g = (2.0019 \pm 0.0002)$ and ΔB_{pp}=0.9 mT as parameters, was ascribed to Mn^{2+} in CdS matrix [52]. This signal was the

only one which could be univocally attributed to external impurities in CdS matrix.

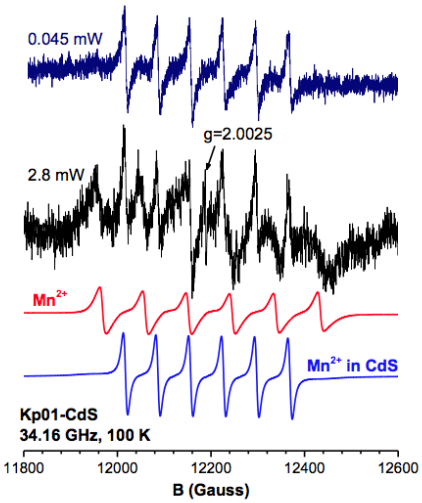

Figure 3.15: *Q-band EPR spectra of the commercial sample (Kremer Cd yellow n. 01) measured at 100 K at two different microwave powers, together with the simulations of the two Mn^{2+}spectra measured.*

For more clarity, all the results obtained with EPR investigation were summarized in Table 3.5.

3.5 Discussion of results

A set of seven historical cadmium yellow pigments, and a commercial cadmium yellow purchased from Kremer Pigmente were analyzed with the aid of a multi-analytical protocol which included morphological investigation, PL techniques, UV photography at a microscale, and EPR. The methodology of investigation was chosen following two research studies which were used as reference: the first one by Cesaratto et al. [12], highlighted the high dependence of spectral and lifetime emission properties of cadmium yellow pigments on the excitation irradiance, with the emission from the trap states promoted at low-energy, while saturation of the trap state emission, and subsequent opening of the band edge recombination, allowed at high irradiance values. Similar results were obtained for the investigation of historical samples showed in this thesis, for which both the emission from the band edge and from the trap states could be observed. Investi-

Sample name	X-band, 9.45 GHz (RT)	Q-band, 34.0 GHz (T=100 K)
S3	asymmetric, broad signal at g=2.48	weak signals at g=4.3, g=3.4 → isolated Fe^{3+} clusters; strong, broad signal at g=2.486 → not assigned; weak Mn^{2+} signal with A=94 → not in CdS matrix
S6	no signal detected	weak Mn^{2+} signal with A=94 → not in CdS matrix; weak, broad signal at g=2.30 → not assigned; sharp signal at 2.0022 → oxygen radicals in CdS
S7	broad signals at g=4.27, g=2.05 very strong signal at g=2.29 weak signals at g=3.30, g=1.92 → very probably Fe and Cu clusters	weak Mn^{2+} signal with A=94 → not in CdS matrix
Kremer Cd	no signal detected	weak Mn^{2+} signal at A=68 G → Mn^{2+} in CdS

Table 3.5: *Summary of all signals revealed by EPR measurement.*

gation of optical properties of historical lithopone pigments was used as further reference [53]. The cited study underlines the importance of investigation of historical samples at a microscale. A similar protocol of investigation was applied to the study of historical Cd pigments. In this case, UV photography at a microscale revealed interesting features in the luminescence of historical Cd yellows, and allowed to observe for the first time the presence of several emitting centres for both excitation regimes. Extensive morphological investigation of the surface of the selected samples was also considered. High-resolution FESEM-EDX allowed to extract important information that were correlated with the PL results. While PL of the near band edge emission did not give significant results, samples characterized by analogous morphology, rather than similar chemical composition, shared similar PL emission from the trap states. More in detail, samples S2 and S3, which consist of very small roundish particles, showed almost equal PL spectra, kinetic properties, and similar features under the microscope. Samples S5, S7, and the commercial sample exhibited a higher luminescence yield and trap states characterized by a longer average lifetime. The same samples showed a more homogeneous emission under UV-microphotography investigation, and a morphological structure composed of larger grains. Similarly to what described for historical lithopone samples, EPR spectroscopy was employed in the attempt to investigate the nature of luminescent centres observed under the microscope in histori-

cal cadmium pigments. A photosensitive centre was attributed to Fe^{3+} in sample S3. Fe is usually present in Sphalerite (ZnS) as main impurity, under the form of Fe^{2+} ions which substitute for Zn sites [30]. Hence, the presence of iron clusters might be related to the coprecipitation of zinc in cadmium-zinc sulfide. The presence of Fe^{3+} state rather than Fe^{2+} might be due to oxidation of the pigment surface, or to trapping mechanism of free holes produced by irradiation, after which Fe^{2+} becomes Fe^{3+} and can therefore be observed with EPR, and parallel trapping of electrons by other trap states [54].A very weak Mn^{2+} signal was observed for all the analyzed samples, but it could be univocally attributed to Mn ions in CdS matrix only for the commercial sample. Counio et al. observed that in bulk Mn^{2+}-doped CdS, strong luminescence requires the presence of so-called sensitizers such as Cl, In, Ga, Ag, and Cu. If sensitizer are present, a resonant energy transfer mechanism from defect centres associated with these impurities and manganese ions allows for the emission from Mn ions at 580 nm [50]. If only manganese impurities are present in the commercial sample, this might explain why no luminescent inclusion were observed. It remains difficult to explain the lack of EPR results for the historical samples. Metal impurities which diffuse into the CdS matrix during annealing have been observed to promote the conversion of the CdSmatrix from cubic to hexagonal, due to re-arrangement of the crystal lattice. This rearrangement also promotes the formation of Cd- and S- vacancies [55]. Emission from impurities in CdS lattice is therefore very difficult to probe due to the strong overlap of this emission with emission arising from native defects. Furthermore, the luminescence of CdS and $(Cd, Zn)S$ is known to be strongly dependent on the surface conditions, with the most part of luminescent processes taking place in the surface region of crystals [56]. Cd-based materials are known for being extremely susceptible to alteration as a result of their reactions with light, oxygen, and other agents of degradation present in the environment. The degradation mechanisms behind these alterations are often complex, involving traces of synthesis starting reagents or other impurities in the paint, requiring the presence of multiple degradation agents. External impurities might be hosted in the pigment matrix even in trace amounts. CdS was produced as a by-product of zinc ores such as Sphalerite; therefore, it is not improper to hypothesize that the same impurities found in lithopone samples could be present in cadmium pigments. The presence of impurities, together with chemical and physical alterations, might reflect in alteration of the concentrations and occupations of recombination centres and traps leading to the formation of complex surface defect states which involve native and external defects. This complex

defects could be still responsible for the PL emission although they cannot be revealed by EPR spectroscopy.

An attempt to performe μ-FLIM was done on the most luminescent sample (S7). Unfortunately, a residual fluorescence from the objectives of intensity comparable with the PL signal from the pigment did not allow to perform the measurement under the same experimental conditions employed for the study of lithopone samples. A further, quick attempt was performed with the aid of a 15x magnification catadioptric objective. This objective did not showed any intrinsic fluorescence but it is not designed for the optical setup, and therefore allowed the emission to be observed on a quite limited field of view (Figure 3.16).

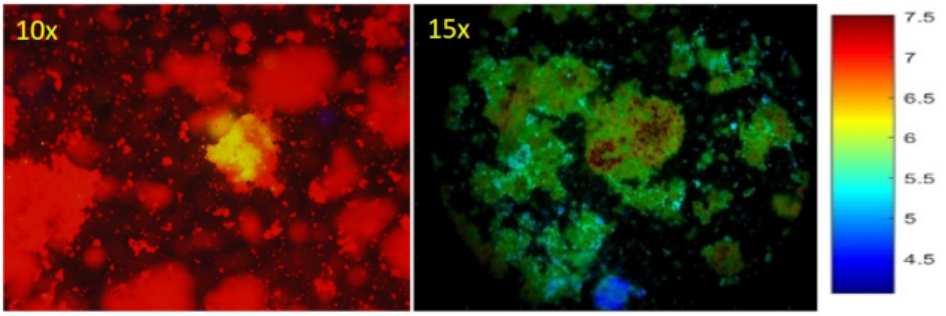

Figure 3.16: *(left) UV photography of the PL emission for a selected area of sample S7 taken under 10x magnification, and (right) lifetime map of a similar (but not coincident) area taken under 15x magnification, following monoexponential decay data fitting, shown in false color.*

Despite the less than optimal measurement conditions, a heterogeneous distribution of the lifetimes could be still observed for the selected area. This result highlighted for the necessity of developing a setup equipped with proper optics, capable of performing fluorescence lifetime imaging even on low-emitting samples which in future will be employed for the study of the kinetic properties of historical cadmium pigments at a microscale. If significant results will be obtained, these will need to be complemented with analytical techniques which, similarly to EPR, can determine the nature of the luminescent centres observed. In past, synchrotron radiation facilities was employed for the micro-analysis of the degradation of cadmium yellow pigments in paintings [9, 57], while impurities in Zn-based pigments were successfully analyzed with the aid of synchrotron-based micro-mapping [58]. A similar protocol of investigation, based on techniques such as micro X-ray fluorescence, micro X-ray absorption, and

synchrotron UV luminescence imaging could help in the identification and distinction between native defects and external impurities in historical cadmium samples, as well as their role in pigment's degradation.

CHAPTER 4

Application of Fluorescence Lifetime Imaging to the study of zinc white paint layer in Picasso's painting "Harlequin" (1927)

THIS chapter is intended to show an example where Fluorescence Lifetime Imaging was used on the Picasso's paintings "Harlequin" (1927) during in-situ investigation at the Metropolitan Museum of Art, New York (USA). The painting contained zinc-based layer paint. A comment on experimental results will be given on the basis of the knowledge acquired during the study of modern semiconductor pigments.

4.1 Pablo Picasso, Harlequin

Harlequin oil on canvas (Figure 4.1)was painted by Pablo Picasso in 1927. It belongs to the series of Picasso's paintings which have Harlequin as main subject. Picasso, who considered Harlequin as his alter ego, represented here an enigmatic character, and painted himself as a white silhouette ob-

h 

Figure 4.1: *Pablo Picasso, Harlequin (1927). Metropolitan Museum of Art, New York (USA).*

serving from the left margin the disoriented figure.
The paint was donated to the Metropolitan Museum of Art by Mr. and Mrs. Klaus G. Perls. Signature and date were painted by the artist in black and two shades of gray paint, at the upper right corner. The painting is in good state of conservation, with no visible fading of the paint layer. Dimensions are (81.3 x 65.1 cm).

4.1.1 Results

Laser Induced Fluorescence (LIF) measurement was performed on four selected areas of the painting (white and pale brown from the painted frame, brown paint from Harlequin's collar, and gray from the table behind the figure). The PL emission was excited with a CW laser (λ_{exc}=375nm) and recorded in the visible spectrum. The PL was collected from a point of surface 1 mm in diameter. Recorded spectra are shown following background substraction (mainly arising from sensor read and dark noise) and correction for the spectral efficiency of the system. Results are shown in Figure 4.2.

Normalized PL emission spectra are shown. For all the investigated areas, a peaked emission at around 380 nm (partially covered by the excita-

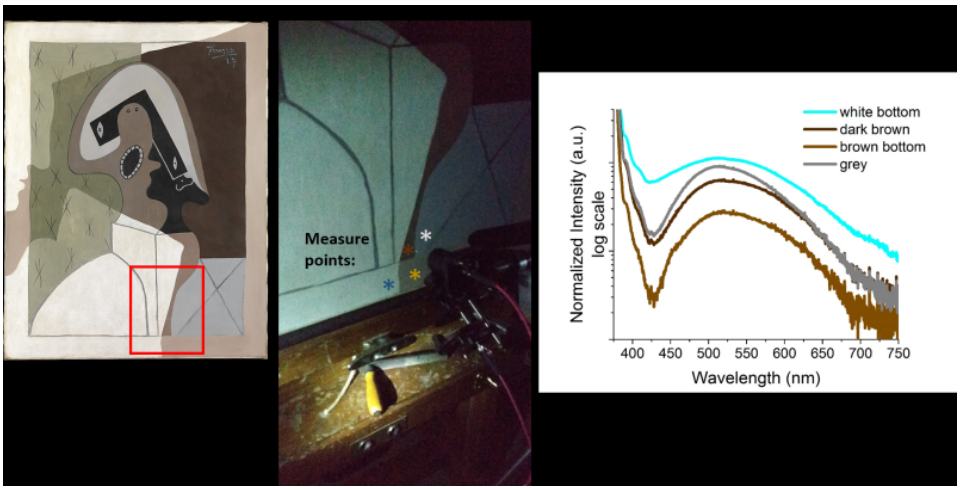

Figure 4.2: *LIF measurement on four selected areas of the painting: white (blue star) and pale brown (yellow star) from the painted frame, brown paint from Harlequin's collar (brown star), and gray from the table behind the figure (grey star).*

tion) and a broad peak centered at 520 nm were observed. These peaks are indicative of the presence of ZnO as white pigment (E_g for ZnO is around 380 nm [1]). The broad emission in the visible range is typical trap states in Zn compounds. In ZnO, trap states are usually ascribed to Zn- or O-vacancies rather then to metallic impurities [59]. The presence of ZnO was subsequently confirmed by XRF measurement.

Fluorescence Lifetime Imaging was performed on the whole painting. The gate width was set to 100 nm in order to measure the dynamic of the PL from ns (organic materials) to μs (semiconductor pigments). Figures 4.3, 4.4 , and 4.5 show results for three selected areas.

Three different kinetics trends were observed. The first one was characteristic of areas where the shortest component of the multiexponential fit (τ_1) is the most significant. Areas C and D from Figure 4.3 can be taken as example. For those areas, the average lifetime is below 100 ns. The second trend is representative of areas where the shortest (τ_1) and the longest (τ_3) components had both a significant weight $A\tau$. For those areas, the average lifetime falls between 100-1000 ns. Area C from Figure 4.4 can be taken as example. The last trend concerned areas where the longest component of the multiexponential decay was the most significant contribution. Those areas are characterized by an effective emission of the order of microseconds. Areas A from Figures 4.3 and 4.4, and area D from Figure 4.5 belong

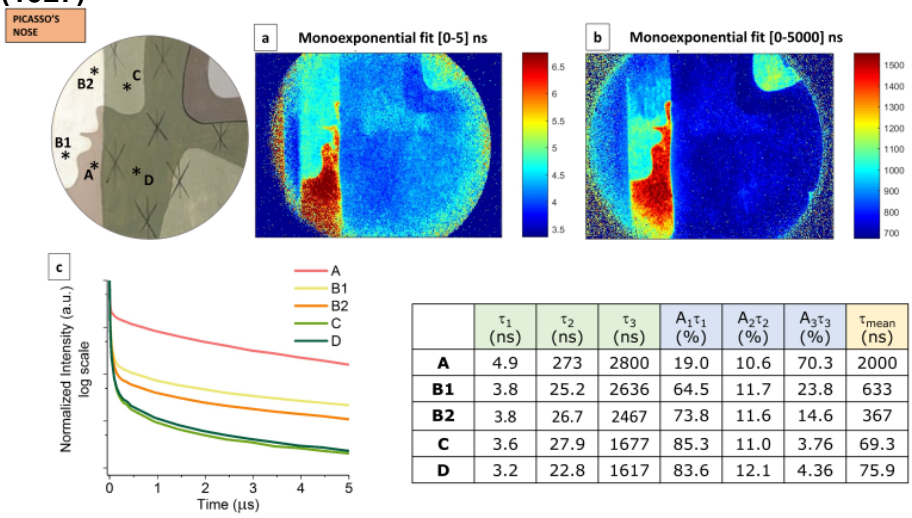

	τ_1 (ns)	τ_2 (ns)	τ_3 (ns)	$A_1\tau_1$ (%)	$A_2\tau_2$ (%)	$A_3\tau_3$ (%)	τ_{mean} (ns)
A	4.9	273	2800	19.0	10.6	70.3	2000
B1	3.8	25.2	2636	64.5	11.7	23.8	633
B2	3.8	26.7	2467	73.8	11.6	14.6	367
C	3.6	27.9	1677	85.3	11.0	3.76	69.3
D	3.2	22.8	1617	83.6	12.1	4.36	75.9

Figure 4.3: *(a) Map of the lifetimes following monoexponential fit from 0 to 5 nm, (b) from 0 to 5000 ns, (c) decay curves of selected points (abeled in capital letters) together with kinetics parameters following 3-exponential fit of the decay curves.*

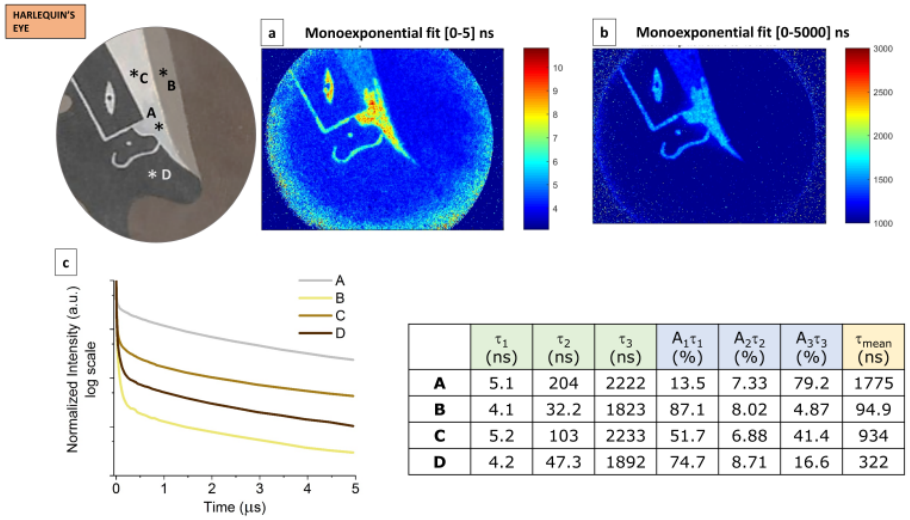

	τ_1 (ns)	τ_2 (ns)	τ_3 (ns)	$A_1\tau_1$ (%)	$A_2\tau_2$ (%)	$A_3\tau_3$ (%)	τ_{mean} (ns)
A	5.1	204	2222	13.5	7.33	79.2	1775
B	4.1	32.2	1823	87.1	8.02	4.87	94.9
C	5.2	103	2233	51.7	6.88	41.4	934
D	4.2	47.3	1892	74.7	8.71	16.6	322

Figure 4.4: *(a) Map of the lifetimes following monoexponential fit from 0 to 5 nm, (b) from 0 to 5000 ns, (c) decay curves of selected points (abeled in capital letters) together with kinetics parameters following 3-exponential fit of the decay curves.*

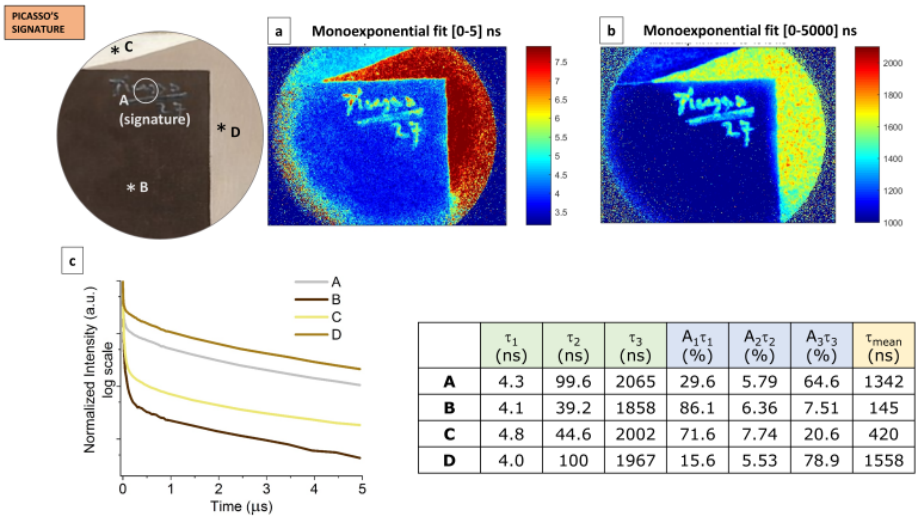

	τ_1 (ns)	τ_2 (ns)	τ_3 (ns)	$A_1\tau_1$ (%)	$A_2\tau_2$ (%)	$A_3\tau_3$ (%)	τ_{mean} (ns)
A	4.3	99.6	2065	29.6	5.79	64.6	1342
B	4.1	39.2	1858	86.1	6.36	7.51	145
C	4.8	44.6	2002	71.6	7.74	20.6	420
D	4.0	100	1967	15.6	5.53	78.9	1558

Figure 4.5: *(a) Map of the lifetimes following monoexponential fit from 0 to 5 nm, (b) from 0 to 5000 ns, (c) decay curves of selected points (abeled in capital letters) together with kinetics parameters following 3-exponential fit of the decay curves.*

to this group. The distribution of this long-living PL emission can be observed in the map of the lifetimes obtained by monoexponential fit from 0 to 5 μs (Figures4.3b; 4.4b; 4.5b).

The complex behaviour of the luminescence might arise from different factors. The kinetic parameters measured have to be considered as average values which include the emission from different materials such as binders, pigments, substrate materials, and the way each emitter interacts with its neighbours. Nevertheless, the diversity in the average lifetime of the ms decay kinetics (Figure 4.6) which was ascribed to the emission from trap states in ZnO, suggested that the artist used zinc whites from different sources.

Summarizing, the following conclusion can be pointed out:

- The presence of ZnO, already detected with XRF investigation, was confirmed by LIF results.

- A long-living luminescence signal has been detected in all the measured area (probably responsible for a flat, uniform, greenish fluorescence under UV light inspection of the artwork). This signal can be attributed either to pure ZnO or to a mixture of ZnO and other semi-

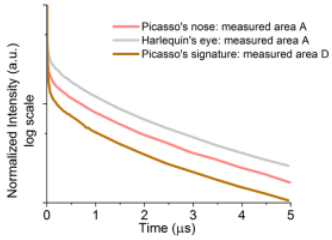

	τ_1 (ns)	τ_2 (ns)	τ_3 (ns)	$A_1\tau_1$ (%)	$A_2\tau_2$ (%)	$A_3\tau_3$ (%)	τ_{mean} (ns)
Picasso nose (area A)	4.9	273	2800	19.0	10.6	70.3	2000
Harlequin eye (area A)	5.1	204	2222	13.5	7.33	79.2	1775
Picasso signature (area D)	4.3	99.6	2065	29.6	5.79	64.61	1342

Figure 4.6: *decay curves of selected points, kinetics parameters following 3-exponential fit of the decay curves for the areas which showed the longest emission.*

conductor pigments with characteristic microsecond decay behavior (most likely ZnS and lithopone). These pigments might be present in trace concentrations that are below the detection limit of the XRF device. Their presence cannot be excluded by LIF analysis because the excitation wavelength is higher than ZnS bandgap (350 nm for the cubic form). Nevertheless, ZnS or lithopone even in small amounts can significantly affect the lifetime results.

- Differences in the average μs average lifetimes suggest that semiconductor white pigments from different sources have been used (as fillers, preparatory layer, etc.).

CHAPTER 5

Conclusions

UV, VIS, or IR light is commonly employed by conservator for the inspection of works of art to reveal important features such as the presence of imperfections and evidence of restoration, and to select sampling locations for further analysis. Instead, advanced photoluminescence techniques can provide a deep chemical and physical description of cultural heritage materials with a non- or micro-invasive approach. The research reported in this thesis described a method for the characterization of the optical properties of luminescent historical semiconductor pigments based on the employment of advanced photoluminescence experimental techniques. Two types of pigment have been considered. Lithopone white pigment ($ZnS + BaSO_4$) is non-toxic, easy and cheap to manufacture, and can be used together with other pigments and binders without provoking mixing reactions. Despite the fact that Lithopone possesses good qualities as pigment, it gained poor reputation as an artist's pigment, making difficult to trace its usage from factory production, to colourmakers and to artists from the 19^{th} Century to the 20^{th} Century. Little attention has been paid to the understanding of its aging characteristics and the extension of its usage. The lack of data regarding Lithopone pigment's physical and chem-

ical properties, as well as difficulties related to its identification in works of art, made the characterization of Lithopone an underinvestigated problem worthy of attention. The optical properties of six historical Lithopone pigments from the beginning of the 20^{th} Century were analyzed through a combination of microscopy-based PL and time-resolved PL techniques which were implemented specifically for performing this experiment. At a microscale, the PL of historical luminescent lithopone resulted to be composited of luminescent inclusions emitting at different colours from blue to red. The emitting centers were characterized by PL decay times of the order of μs. In order to understand the nature of this inclusions, a careful overview of historical sources documenting the manufacturing process of lithopone pigment was done. Information gathered allowed to hypothesize that metal impurities normally present in zinc mineral sources, if not properly removed during the synthesis of the pigment, could be responsible of the observed features. This hypothesis was validated by EPR spectroscopy measurement which allowed for identification of Mn^{2+}_{Zn} and Cu^{2+}_{Zn} metal ions in ZnS matrix, and further indicate the presence of Fe as a constituent of the ZnS mineral ore.

The successful result obtained motivated to explore the potentiality of the same protocol of investigation on the study of the optical properties of historical Cd-based yellow pigments from the 19^{th} and early 20^{th} Century. Unlike Lithopone, in recent years Cd yellows (CdS and $Cd_{1-x}Zn_xS$) underwent a consistent due to the evidence of discolouration and fading of Cd-yellow containing paint in modern artworks. UV photography of historical Cd-yellows were taken under the microscope, under two excitation regimes. A non- linear behavior of the luminescence was observed by exciting the luminescence at different irradiance, making possible to selectively excite the luminescence from the band edge or from the trap state. At great heterogeneity of the luminescence was observed for both excitation regimes at a microscale, demonstrating the potential of μ-PL for evidencing complex luminescence behaviour which cannot be revealed with bulk analysis. Historical manufacturing process of Cd-yellows and scientific literature on PL emission of CdS were studied in order to understand the nature of the luminescence observed. Compared to ZnS, the synthesis of CdS seem to be much more sensitive to reaction conditions such as the pH of the solution or the temperature of calcination. Mixed phases of amorphous, cubic, and hexagonal CdS are often observed in historical Cd pigments. The necessity to obtain consistent tonality between different synthesis batches might have induced colourmakers to adulterate the final product by modifying the Cd/Zn ration, and adding other compounds as extenders. Therefore,

a greater variety of historical Cd yellows exist, which make the study of their physical and chemical properties more difficult. In scientific literature, structural defects in CdS such us Cd- or S- vacancies, and external impurities, have been characterized with the aid of PL techniques. All the studies remark how point defects in CdS are often complex in nature and arise from the interaction between shallow donors and acceptors levels and trap states which act as recombination centres. Furthermore, the emission from defect states is strongly dependent on the surface conditions. EPR spectroscopy did not allow to univocally identify the nature of the luminescent centres although paramagnetic species such as Cu^{+}, Cu^{2+}, Al^{2+}, and Mn^{2+} are common dopant agents for CdS. If present, these impurities might be therefore be part of defect-impurity complexes which do not exhibit EPR signal. The role of native defects and external impurities in the fading of Cd yellows observed at the surface of paintings is still little studied. In future, the complex composition of historical Cd pigments should be taken into account for the understanding of their degradation paths.

The research presented in this thesis explored the potential of spatially and temporally resolved PL microscopic imaging as a technique for the identification and qualitative characterization of luminescence features in modern pigments. To a general extent, the PL microscopic imaging protocol established in this thesis can provide useful information about a range of inorganic and organic materials. Running a PL experiment is cheap, fast, does not require sample preparation, and is non-destructive. Nevertheless, the data acquired are often difficult to interpret and ascribe. This fact highlighted the need for integration with high-resolution analytical techniques which allow a more complete investigation of the chemical composition of the material. EPR spectroscopy revealed to be a valuable tool in some cases, but failed in the description of non-paramagnetic species and complex defects. Synchrotron spectroscopy and imaging encompasses techniques from the infrared (FT-IR) to the hard X-ray region (X-ray absorption, fluorescence, diffraction and microtomography), and are still the most valuable tool for the study of heritage materials at a micrometric and nanometric scale. Nevertheless, synchrotron facilities are not of easy access, and limited amount of time can be dedicated to each experiment. A synchrotron experiment should be therefore anticipated by laboratory-based investigation which allows to collect a statistically meaningful set of experimental data preserving the integrity of the samples. Although not exhaustive, the protocol of study discussed in this thesis, and the effort in correlating experimental results with information gathered from historical sources, revealed

to be a useful baseline for supporting further investigation for the study of the intrinsic heterogeneity of other painting materials.

List of Publications

Peer-reviewed articles

- Jacopin, G., Rigutti, L., Bellei, S., Lavenus, P., Julien, F.H., Davydov, A.V., Tsvetkov D., Bertness K.A., Sanford N.A., Schlager J.B., Tchernycheva M., Photoluminescence Polarization in strained GaN/AlGaN core/shell nanowires, Nanotechnology (2012) 17;23(32)
- Nevin, A.B.; Cesaratto, A.; Bellei, S.; D'Andrea, C.; Toniolo, L.; Valentini, G.; Comelli, D., Time-Resolved Photoluminescence Spectroscopy and Imaging: new approaches to the analysis of cultural heritage and its degradation, Sensors (2014) 14(4):6338–55
- Capogrosso, V.; Bellei, S.; Cesaratto, A.; Valentini, G.; Comelli, D.; Nevin, A. B., An integrated approach based on micro-mapping analytical techniques for the detection of impurities in historical Zn-based white pigments, Journal of Analytical Atomic Spectrometry (2015) 30, 828–838
- Bellei, S.; Nevin, A.B.; Cesaratto, A.; Capogrosso, V.; Valentini, G.; Comelli, D., Multianalytical Study of Historical Luminescent Lithopone for the Detection of Impurities and Trace Metal Ions, Analytical Chemistry (2015) 87 (12), pp 6049–6056
- A. Artesani, S. Bellei, V. Capogrosso, A. Cesaratto, S. Mosca, A. B. Nevin, G. Valentini, D. Comelli, Photoluminescence properties of zinc white: an insight into its emission mechanisms through the study of historical artist materials, Applied Physics A (2016) 122(12):1053

Conferences

- Integration of micro-luminescence imaging and time-resolved luminescence spectroscopy for the study of modern semiconductor pigments, Technart 2013, Rijksmuseum, Amsterdam (Netherlands) (oral)
- Multi-Analytical Study of Historical Semiconductor Pigments for the Detection of Impurities and Trace Metal Ions, Gordon Research Seminar 2014: Scientific Methods in Cultural Heritage Research (GRS), Sunday River Newry, ME (USA) (oral and poster)
- Exploring the kinetics of the luminescence emission from red lake pigments, Technart 2015, University of Catania (Italy) (poster)
- Multianalytical study of the metal ion-anthraquinone complex in red lake pigments, InArt 2016, 2nd International Conference on Innovation in Art, Research and Technology, Ghent (Belgium) (poster)

List of Figures

List of Tables

Bibliography

[1] Gunter Buxbaum. *Industrial inorganic pigments*. John Wiley and Sons, 2008.

[2] Catia Clementi, Francesca Rosi, Aldo Romani, Riccardo Vivani, Brunetto G Brunetti, and Costanza Miliani. Photoluminescence properties of zinc oxide in paints: a study of the effect of self-absorption and passivation. *Applied spectroscopy*, 66(10):1233–1241, 2012.

[3] Rebecca Capua. The obscure history of a ubiquitous pigment: Phosphorescent lithopone and its appearance on drawings by john la farge. *Journal of the American Institute for Conservation*, 53(2):75–88, 2014.

[4] Gustav Jantsch and Paul Wolski. Process for producing lithopone fast to light, 1928. US Patent 1,693,902.

[5] Lara Boselli, Samuele Ciattini, Monica Galeotti, M Lanfranchi, Cristiana Lofrumento, Marcello Picollo, and Angela Zoppi. An unusual white pigment in la verna sanctuary frescoes: An analysis with micro-raman, ftir, xrd and uv-vis-nir fors. *Preservation Science*, 6:38–42, 2009.

[6] D Comelli, A Nevin, A Brambilla, I Osticioli, G Valentini, L Toniolo, M Fratelli, and R Cubeddu. On the discovery of an unusual luminescent pigment in van gogh's painting les bretonnes et le pardon de pont aven. *Applied Physics A*, 106(1):25–34, 2012.

[7] Bronwyn Leone, Aviva Burnstock, Chris Jones, Peter Hallebeek, Jaap Boon, and Katrien Keune. The deterioration of cadmium sulphide yellow artists' pigments. In *Triennial meeting (14th), The Hague, 12-16 September 2005: preprints*, pages 803–813. James & James, 2005.

[8] Laura Giacopetti. *Degradation of Cd-yellow pigment: an ab initio study of defects and adsorption of oxygen and water on CdS*. PhD thesis, Universita degli Studi di Cagliari, 2016.

[9] E Pouyet, M Cotte, B Fayard, M Salomé, F Meirer, A Mehta, ES Uffelman, A Hull, F Vanmeert, J Kieffer, et al. 2d x-ray and ftir micro-analysis of the degradation of cadmium yellow pigment in paintings of henri matisse. *Applied Physics A*, 121(3):967–980, 2015.

[10] Mathieu Thoury, John K Delaney, E René de la Rie, Michael Palmer, Kathryn Morales, and Jay Krueger. Near-infrared luminescence of cadmium pigments: in situ identification and mapping in paintings. *Applied spectroscopy*, 65(8):939–951, 2011.

[11] Francesca Rosi, Chiara Grazia, Francesca Gabrieli, Aldo Romani, Marco Paolantoni, Riccardo Vivani, Brunetto G Brunetti, Philippe Colomban, and Costanza Miliani. Uv vis-nir and micro raman spectroscopies for the non destructive identification of cd1-xznxs solid solutions in cadmium yellow pigments. *Microchemical Journal*, 124:856–867, 2016.

[12] Anna Cesaratto, Cosimo D'Andrea, Austin Nevin, Gianluca Valentini, Francesco Tassone, Roberto Alberti, Tommaso Frizzi, and Daniela Comelli. Analysis of cadmium-based pigments with time-resolved photoluminescence. *Analytical Methods*, 6(1):130–138, 2014.

[13] Daniela Comelli, Cosimo D'Andrea, Gianluca Valentini, Rinaldo Cubeddu, Chiara Colombo, and Lucia Toniolo. Fluorescence lifetime imaging and spectroscopy as tools for nondestructive analysis of works of art. *Applied optics*, 43(10):2175–2183, 2004.

[14] Xiaosheng Fang, Tianyou Zhai, Ujjal K Gautam, Liang Li, Limin Wu, Yoshio Bando, and Dmitri Golberg. Zns nanostructures: from synthesis to applications. *Progress in Materials Science*, 56(2):175–287, 2011.

[15] J Manam, V Chatterjee, S Das, A Choubey, and SK Sharma. Preparation, characterization and study of optical properties of zns nanophosphor. *Journal of Luminescence*, 130(2):292–297, 2010.

[16] D Denzler, M Olschewski, and K Sattler. Luminescence studies of localized gap states in colloidal zns nanocrystals. *Journal of applied physics*, 84(5):2841–2845, 1998.

[17] D Kurbatov, A Opanasyuk, S Kshnyakina, V Melnik, and V Nesprava. Luminescent and optical characteristics of zinc sulfide thin films produced by close-spased vacuum sublimation. In *Paper presented at the 4th National Conference on Applied Physics*, 2008.

[18] YY Chen, JG Duh, BS Chiou, and CG Peng. Luminescent mechanisms of zns: Cu: Cl and zns: Cu: Al phosphors. *Thin Solid Films*, 392(1):50–55, 2001.

[19] Hiroji Kawai, Shigeo Kuboniwa, and Teruhiko Hoshina. Concentration dependence of green-cu luminescence in zns: Cu, al. *Japanese Journal of Applied Physics*, 13(10):1593, 1974.

[20] A Murugadoss and Arun Chattopadhyay. Tuning photoluminescence of zns nanoparticles by silver. *Bulletin of Materials Science*, 31(3):533–539, 2008.

[21] HV Chung, PT Huy, TT An, NTM Thuy, and ND Chien. Synthesis and optical properties of zns nanostructures. 2008.

[22] Encai Hao, Yipeng Sun, Bai Yang, Xi Zhang, Jiming Liu, and Jiacong Shen. Synthesis and photophysical properties of zns colloidal particles doped with silver. *Journal of colloid and interface science*, 204(2):369–373, 1998.

[23] PV Ben and PT Tue. The role of color luminescence centers mn, cu, co in the semicondutors with wide band gap zns, zno and their applications. *VNU Journal of Science*, 24:181–187, 2008.

[24] K Jayanthi, S Chawla, H Chander, and D Haranath. Structural, optical and photoluminescence properties of zns:cu nanoparticle thin films as a function of dopant concentration and quantum confinement effect. *Crystal Research and Technology*, 42(10):976–982, 2007.

[25] Jian Cao, Jinghai Yang, Yongjun Zhang, Lili Yang, Yaxin Wang, Maobin Wei, Yang Liu, Ming Gao, Xiaoyan Liu, and Zhi Xie. Optimized doping concentration of manganese in zinc sulfide nanoparticles for yellow-orange light emission. *Journal of Alloys and Compounds*, 486(1):890–894, 2009.

[26] K Manzoor, SR Vadera, N Kumar, and TRN Kutty. Synthesis and photoluminescent properties of zns nanocrystals doped with copper and halogen. *Materials Chemistry and physics*, 82(3):718–725, 2003.

[27] Nigel J Cook, Cristiana L Ciobanu, Allan Pring, William Skinner, Masaaki Shimizu, Leonid Danyushevsky, Bernhardt Saini-Eidukat, and Frank Melcher. Trace and minor elements in sphalerite: A la-icpms study. *Geochimica et Cosmochimica Acta*, 73(16):4761–4791, 2009.

[28] George C Lisensky, Manish N Patel, and Megan L Reich. Experiments with glow-in-the-dark toys: kinetics of doped zns phosphorescence. *J. Chem. Educ*, 73(11):1048, 1996.

[29] A Hoffmann, I Broser, P Thurian, and R Heitz. Fine structure of the cu2+ centre in cds. *Journal of crystal growth*, 101(1-4):532–535, 1990.

[30] HF Steger and LE Desjardins. Oxidation of sulfide minerals; v, galena, sphalerite and chalcocite. *The Canadian Mineralogist*, 18(3):365–372, 1980.

[31] Junye Liu, Chunxu Liu, Yingguang Zheng, Dan Li, Wu Xu, and Jiaqi Yu. Three types of site of mn2+ in zns: Mn2+ nanocrystal/pyrex glass composites. *Journal of Physics: Condensed Matter*, 11(27):5377, 1999.

[32] M Stefan, SV Nistor, D Ghica, CD Mateescu, M Nikl, and R Kucerkova. Substitutional and surface mn 2+ centers in cubic zns: Mn nanocrystals. a correlated epr and photoluminescence study. *Physical review B*, 83(4):045301, 2011.

[33] N Murase, R Jagannathan, Y Kanematsu, M Watanabe, A Kurita, K Hirata, T Yazawa, and T Kushida. Fluorescence and epr characteristics of mn2+ doped zns nanocrystals prepared by aqueous colloidal method. *The Journal of Physical Chemistry B*, 103(5):754–760, 1999.

[34] Liu Tiegeng, Zhang Qian, Ye Lin, and Shao Shuxun. Discovery of primary greenockite in nature, as exemplified by the niujiaotang cadmiumzincdeposit, guizhou. *Acta Mineralogica Sinica*, 2:191–196, 2004.

[35] Jozef Plachy. *Cadmium recycling in the United States in 2000*. US Department of the Interior, US Geological Survey, 2003.

[36] Guy W Lussiez, Eddie C Chou, and Leo W Beckstead. Production of hexagonal cadmium sulfide pigment, 1989. US Patent 4,810,303.

[37] J O'brien James. Process for making yellow pigments, 1936. US Patent 2,061,368.

[38] Nerlinger. Production of cadmium red pigments, 1949. US Patent 2,479,636.

[39] Charles Kittel. *Introduction to solid state*, volume 162. John Wiley & Sons, 1966.

[40] R Pässler. Alternative analytical descriptions of the temperature dependence of the energy gap in cadmium sulfide. *physica status solidi (b)*, 193(1):135–144, 1996.

[41] RM Ma, XL Wei, L Dai, HB Huo, and GG Qin. Synthesis of cds nanowire networks and their optical and electrical properties. *Nanotechnology*, 18(20):205605, 2007.

[42] G Giribabu, G Murali, D Amaranatha Reddy, RP Vijayalakshmi, and N Madhusudhana Rao. Effect of mg doping on the structural and optical properties of cds nanoparticles synthesized by co-precipitation method. *Journal of Nano-and Electronic Physics*, 4(4):4028–1, 2012.

[43] Hongyu Sun, Xiaohong Li, Yan Chen, Wei Li, Feng Li, Baoting Liu, and Xiangyi Zhang. The control of the growth orientations of electrodeposited single-crystal nanowire arrays: a case study for hexagonal cds. *Nanotechnology*, 19(22):225601, 2008.

[44] N Chestnoy, TD Harris, R Hull, and LE Brus. Luminescence and photophysics of cds semiconductor clusters: the nature of the emitting electronic state. *SPIE MILESTONE SERIES MS*, 150:574–580, 1998.

[45] LS Pedrotti and DC Reynolds. Change in structure of blue and green fluorescence in cadmium sulfide at low temperatures. *Physical Review*, 119(6):1897, 1960.

[46] Arthur Varghese, Prasenjit Ghosh, and Shouvik Datta. Cadmium vacancy minority defects as luminescence centers in size and strain dependent photoluminescence shifts in cds nanotubes. *The Journal of Physical Chemistry C*, 118(37):21604–21613, 2014.

[47] Jeremy J Ramsden and Michael Grätzel. Photoluminescence of small cadmium sulphide particles. *Journal of the Chemical Society, Faraday Transactions 1: Physical Chemistry in Condensed Phases*, 80(4):919–933, 1984.

[48] LV Borkovskaya, BM Bulakh, L Yu Khomenkova, and IV Markevich. Silver-related local centres in cadmium sulfide. *SEMICONDUCTOR PHYSICS QUANTUM ELECTRONICS AND OPTOELECTRONICS*, 4(3):163–167, 2001.

[49] George A Sullivan. Diffusion and solubility of cu in cds single crystals. *Physical Review*, 184(3):796, 1969.

[50] G Counio, S Esnouf, T Gacoin, and J-P Boilot. Cds: Mn nanocrystals in transparent xerogel matrices: synthesis and luminescence properties. *The Journal of Physical Chemistry*, 100(51):20021–20026, 1996.

[51] A Mukherjee, M Fu, and P Mitra. Influence of zn incorporation in cds: Structural and morphological studies. *Journal of Physics and Chemistry of Solids*, 82:50–55, 2015.

[52] Paul B Dorain. Electron paramagnetic resonance of manganese (ii) in hexagonal zinc oxide and cadmium sulfide single crystals. *Physical Review*, 112(4):1058, 1958.

[53] Sara Bellei, Austin Nevin, Anna Cesaratto, Valentina Capogrosso, Herve Vezin, Caroline Tokarski, Gianluca Valentini, and Daniela Comelli. Multianalytical study of historical luminescent lithopone for the detection of impurities and trace metal ions. *Analytical chemistry*, 87(12):6049–6056, 2015.

[54] J Lambe, J Baker, and C Kikuchi. Photosensitive spin resonance in cds. *Physical Review Letters*, 3(6):270, 1959.

[55] R Mariappan, V Ponnuswamy, M Ragavendar, D Krishnamoorthi, and C Sankar. The effect of annealing temperature on structural and optical properties of undoped and cu doped cds thin films. *Optik-International Journal for Light and Electron Optics*, 123(12):1098–1102, 2012.

[56] IB Ermolovich, GP Peka, and MK Sheinkman. Effect of surface states on luminescent properties of cds single crystals. *Surface Science*, 24(1):229–238, 1971.

[57] Geert Van der Snickt, Joris Dik, Marine Cotte, Koen Janssens, Jakub Jaroszewicz, Wout De Nolf, Jasper Groenewegen, and Luuk Van der Loeff. Characterization of a degraded cadmium yellow (cds) pigment in an oil painting by means of synchrotron radiation based x-ray techniques. *Analytical Chemistry*, 81(7):2600–2610, 2009.

[58] V Capogrosso, F Gabrieli, S Bellei, L Cartechini, A Cesaratto, N Trcera, F Rosi, G Valentini, D Comelli, and A Nevin. An integrated approach based on micro-mapping analytical techniques for the detection of impurities in historical zn-based white pigments. *Journal of Analytical Atomic Spectrometry*, 30(3):828–838, 2015.

[59] A Artesani, S Bellei, V Capogrosso, A Cesaratto, S Mosca, A Nevin, G Valentini, and D Comelli. Photoluminescence properties of zinc white: an insight into its emission mechanisms through the study of historical artist materials. *Applied Physics A*, 122(12):1053, 2016.

Nanotechnology **23** (2012) 325701 (6pp) doi:10.1088/0957-4484/23/32/325701

Photoluminescence polarization in strained GaN/AlGaN core/shell nanowires

G Jacopin[1], L Rigutti[1,2], S Bellei[1], P Lavenus[1], F H Julien[1], A V Davydov[3], D Tsvetkov[3], K A Bertness[4], N A Sanford[4], J B Schlager[4] and M Tchernycheva[1]

[1] Institut d'Electronique Fondamentale UMR CNRS 8622, University Paris Sud, 91405 Orsay, France
[2] Groupe de Physique des Matériaux UMR CNRS 6634, University of Rouen, 76801 St Etienne du Rouvray, France
[3] MML, NIST, Gaithersburg, MD 20899, USA
[4] PML, NIST, Boulder, CO 80305, USA

E-mail: gwenole.jacopin@u-psud.fr

Received 12 April 2012, in final form 26 June 2012
Published 17 July 2012
Online at stacks.iop.org/Nano/23/325701

Abstract
The optical polarization properties of GaN/AlGaN core/shell nanowire (NW) heterostructures have been investigated using polarization resolved micro-photoluminescence (μ-PL) and interpreted in terms of a strain-dependent 6×6 $\mathbf{k} \cdot \mathbf{p}$ theoretical model. The NW heterostructures were fabricated in two steps: the Si-doped n-type c-axis GaN NW cores were grown by molecular beam epitaxy (MBE) and then epitaxially overgrown using halide vapor phase epitaxy (HVPE) to form Mg-doped AlGaN shells. The emission of the uncoated strain-free GaN NW core is found to be polarized perpendicular to the c-axis, while the GaN core compressively strained by the AlGaN shell exhibits a polarization parallel to the NW c-axis. The luminescence of the AlGaN shell is weakly polarized perpendicular to the c-axis due to the tensile axial strain in the shell.

(Some figures may appear in colour only in the online journal)

1. Introduction

Ultraviolet (UV) nitride-based light emitting diodes (LEDs) are attracting considerable attention due to their numerous potential applications, including water purification [1], document authentication, medical diagnostics and phototherapy [2]. However, planar UV LEDs have a lower efficiency than standard blue LEDs [3] due to material and technological issues such as a high density of structural defects [4], difficulties with efficient p-doping of AlGaN alloys with high Al content [5], issues related to the internal electric field in the quantum wells [6] and problems of light extraction efficiency [7], partly related to the unfavorable light polarization parallel to the c-axis in AlGaN layers with Al content above 12% [8]. Nitride core/shell NWs have been intensively studied as building blocks for novel optoelectronic devices such as solar cells [9], LEDs [10–12] or optically pumped nanowire lasers [13]. In the context of LEDs, a quasi-1D geometry is advantageous since NWs are essentially defect-free [14, 15]. This geometry also provides more flexibility in the design of the active region, by making use of non-polar NW facets. Finally, it allows the possibility of emission polarization engineering by tuning the thicknesses and chemical composition of the GaN/AlGaN heterostructure.

The optical polarization of nitride nanowire photoluminescence has been studied by different authors [16–18]. It has been shown that the polarization properties can be affected by the nanowire elongated shape [17, 19]. However, to our knowledge, the influence of the strain state on the polarization properties of a core–shell nanowire has not been investigated yet.

In this work, we report on the optical properties of n-GaN/p-AlGaN core/shell nanowires. These NWs represent a first building block for a complete UV LED structure based on n-GaN/n-AlGaN/p-AlGaN core–multishell NWs. The NW heterostructures are grown in two steps using MBE for the Si-doped n-GaN core and HVPE for the Mg-doped AlGaN shell. The emission properties of the

individual core/shell structures are investigated by position- and polarization-resolved μ-PL at low temperature. The emission of the uncoated strain-free GaN NW core is polarized perpendicular to the *c*-axis, while the GaN core compressively strained by the AlGaN shell exhibits a polarization parallel to the NW *c*-axis. The luminescence of the AlGaN shell is weakly polarized perpendicular to the *c*-axis due to the tensile axial strain in the shell. These polarization properties can be straightforwardly interpreted by considering the effects of uniaxial strain along the *c*-axis on the electronic band structure of GaN and AlGaN in the framework of a 6×6 $\mathbf{k} \cdot \mathbf{p}$ model [20].

2. Sample fabrication and microstructure

Si-doped n-type GaN NWs were grown along the wurtzite *c*-axis on Si(111) substrate by plasma-assisted MBE. Details on the growth procedure are described in [21]. The NWs lengths were uniform at 15 ± 0.1 μm, while their diameters ranged from 50 to 500 nm. In a second step, HVPE growth was employed to form Mg-doped AlGaN shells over the MBE-grown GaN[5] NWs. The HVPE growth conditions were similar to those described in [22] for fabricating p-GaN shells over MBE-grown n-GaN cores. The choice of the HVPE technique for shell overgrowth is motivated by the limited capacity of MBE to achieve core/shell growth in the same process, more efficient p-doping in HVPE process [22], and better compositional uniformity of $Al_xGa_{1-x}N$ alloys in the whole range of x from 0 to 1. The thickness of the conformally deposited epitaxial shells on the GaN NW sidewalls was in the range from 50 to 700 nm. Figure 1 shows an array of vertically-aligned core/shell NWs. During the shell growth for some closely spaced GaN NWs, shadowing effects resulted in only partial AlGaN shell formation. The inset in figure 1 shows an example of such a non-uniform coating, where an AlGaN shell has only been formed over the top 5 μm of the NW.

The Al content in AlGaN shells was determined by x-ray diffraction (XRD) measurements and energy dispersive x-ray spectroscopy (EDX). XRD was performed on the core/shell NW arrays using a Scintag D-500 powder diffractometer[6] with Cu Kα_1 radiation, while elemental analysis was done on individual core/shell NWs using an Oxford Instruments EDX detector attached to a Hitachi S4700 field emission scanning electron microscope (FE-SEM).

The XRD pattern shown in figure 2 reveals the presence of 000*l* reflections from the core/shell structures, confirming that AlGaN forms conformal epitaxial shells over the vertically-aligned GaN NWs. The XRD pattern was used to estimate the Al content in the AlGaN shell although the XRD analysis does not allow separation of the effect of strain from that of composition. As a first approximation for the Al content estimation the strain in the AlGaN shell was neglected. Deconvolution of the broad $Al_xGa_{1-x}N$ component from the main 0004 GaN peak in the inset of figure 2 (at $2\theta = 73.4°$) allows measurement of the *c*-lattice parameter and gives an estimation of the $Al_xGa_{1-x}N$ composition centered around $x = 0.23 \pm 0.07$. The shoulder at $2\theta = 74.8°$ with the two-orders of magnitude lower intensity is assigned to $Al_xGa_{1-x}N$ with $x = 0.62 \pm 0.07$. The uncertainty of 7 at.% is derived from the x versus *c*-parameter calibration, produced in our previous study of AlGaN films (calibration curves not shown) [23].

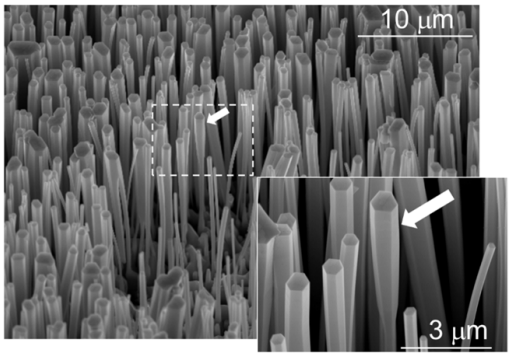

Figure 1. (a) Tilted SEM view of the GaN-core/AlGaN-shell nanowire heterostructures on Si substrate. The inset shows a magnified view of the cone-shaped nanowire due to AlGaN shell thickening towards the NW top.

To correlate these two distinct $Al_xGa_{1-x}N$ compositions with the core/shell microstructure, EDX analysis was performed on individual NWs detached from the substrate. The EDX analysis revealed that the $Al_xGa_{1-x}N$ shell atop the GaN NW is considerably richer in Al than on the NW sidewalls. Typical EDX spectra together with the corresponding SEM image of the analyzed core/shell NW are shown in figure 3. The composition x measured at the top of the shell is 0.54 whereas on the sidewalls of the shell it is only 0.27. The statistical error of measuring Al content by EDX did not exceed $\Delta x = \pm 0.05$.

For the NW base the absence of an Al signal confirms the absence of the AlGaN coating in this region. It should be noted that the EDX analysis was conducted under a low acceleration voltage of 5 keV to ensure that the probe penetration depth did not exceed the actual AlGaN shell thickness; applying Casino 2.42 simulation [24], the calculated excitation depth did not exceed 100 ± 20 nm for the $Al_{0.2}Ga_{0.8}N$ composition, while the actual shell thickness in spots '2' and '3' in figure 3 was estimated from SEM to be 150 to 200 nm. Nevertheless, in view of the possible contribution of a Ga signal from the GaN core to the overall Ga EDX peak, the evaluated EDX compositions should be considered as low-end estimates of the Al content for this particular NW. Taking into account wire-to-wire composition fluctuations, the EDX results are in reasonable agreement with the composition values deduced from the XRD in figure 2.

From the XRD scans on the randomly oriented GaN NWs before and after AlGaN shell coating (not shown), we

[5] For comparison with the previously published data [21], the growth runs were 'C023' for the GaN core and 'N173' for the AlGaN shell.

[6] Any mention of commercial products in this article is for information only; it does not imply recommendation or endorsement by the NIST.

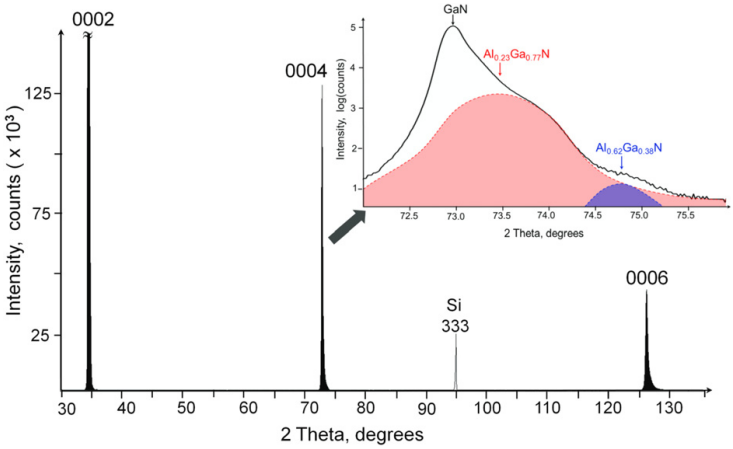

Figure 2. XRD pattern of the core/shell heterostructure NW ensemble shown in figure 1. The 000*l* reflections from the GaN/AlGaN NW arrays dominate the pattern. The inset shows a deconvolution of the 0004 reflection into the GaN main peak (peak profile is not shown) and two $Al_xGa_{1-x}N$ peaks corresponding to Al-poor (red indicated peak with x near 0.23) and Al-rich (blue indicated peak with x near 0.62) compositions.

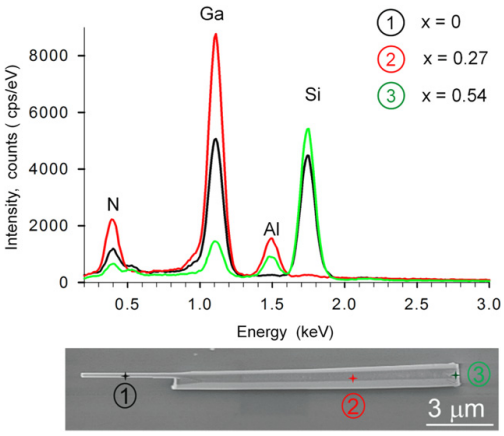

Figure 3. EDX spectra (top figure) measured in three spots of a typical core/shell NW (SEM image shown in the bottom figure) used for PL study. The $Al_xGa_{1-x}N$ composition for each spot is $x = 0$, 0.27 and 0.54, respectively. Note the absence of AlGaN coating at the NW base (left). The strong Si signal in the EDX spectra 1 and 3 arises from the underlying Si substrate.

have estimated the compressive strain induced by the AlGaN shell in the GaN NW cores. For these measurements, NWs that were still attached to the substrate were mechanically disturbed to disrupt their vertical alignment. The induced random orientation of NWs allowed one to observe all GaN diffraction peaks, including the asymmetric reflections. The 2Θ Cu Kα_1 range from 32° to 127° was used to refine the GaN lattice parameters by the least-squares method in Jade 5.0 (Materials Data Inc., Livermore, CA). The corresponding GaN lattice parameters were calculated as follows: $a_0 = 3.1908 \pm 0.0012$ Å, $c_0 = 5.1842 \pm 0.0001$ Å for uncoated NWs, and $a_1 = 3.1890 \pm 0.0015$ Å, $c_1 = 5.1813 \pm 0.0002$ Å for the GaN peak of the AlGaN shell coated NWs. From this analysis, while the shell-induced compression in the a-direction was found to be statistically insignificant due to the large experimental uncertainty, the c-compression value was evident, with $(c_1 - c_0)/c_0 = -5.6 \times 10^{-4}$. It should be noted that this value averages the strain in the whole nanowire ensemble, while the strain of individual nanowires can deviate from this value, as was found from the optical measurements in section 3. Notably, it was not possible to use XRD to extract strain values in the AlGaN shells due to the absence of the 'lattice parameters versus Al content' calibration curve for strain-free AlGaN alloys. An uncertainty in the peak position for unstrained material made it impossible to deconvolute the effect of strain from that of alloy composition on the absolute location of AlGaN peaks.

3. Optical spectroscopy

For the μ-PL studies, wires were detached from their growth substrate by means of ultrasonic agitation in ethanol and then dispersed on a patterned Si substrate with alignment marks. Position and polarization resolved μ-PL spectra were recorded at low temperature around 5 K by exciting the wire with a cw frequency doubled Ar^{++} ion laser operating at 244 nm. The laser was focused onto a spot diameter of 2 μm by a UV objective microscope with 0.4 numerical aperture. The position resolved μ-PL spectral image was obtained by scanning the laser spot along the axial direction of the wire by means of an automated X–Y piezoelectric stage. In order to analyze the polarization of the emission, a linear polarizer was placed at the entrance of the spectrometer. For different positions along the wire, series of spectra were collected at different angles of the polarizer, which was varied over the

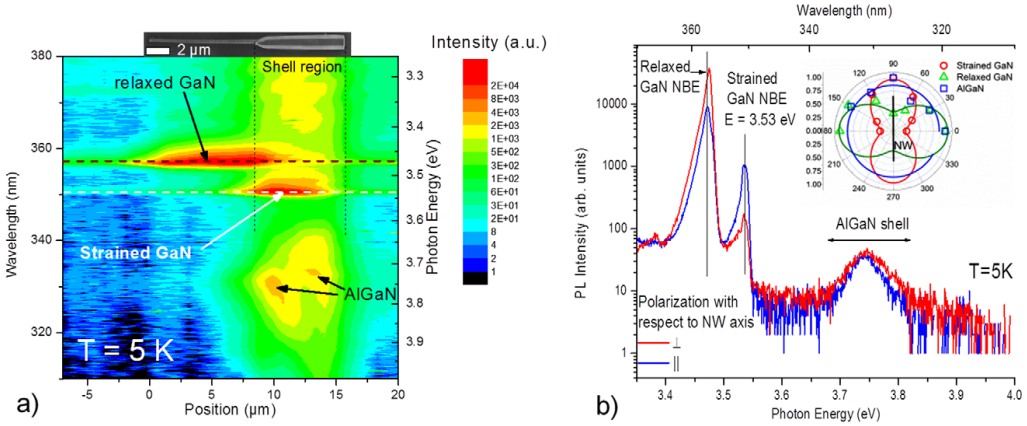

Figure 4. (a) μ-PL line scan of a single core/shell wire (the wire SEM image is shown at the top). (b) μ-PL spectra at different polarization at $T = 5$ K. Inset—normalized polarization diagram for the three different peaks: relaxed GaN at 3.47 eV (green), strained GaN at 3.53 eV (red) and AlGaN peak around 3.75 eV (blue).

interval 0° to 180° with a 15° step size. The response of the system to horizontally or vertically directed light was calibrated using UV light from different unpolarized sources with energies in the range 3.3–3.8 eV. The orientation and the position of the studied wires with respect to the alignment crosses were determined by means of a visualization system consisting of LED illumination and a CCD camera. The morphology of the wires was analyzed using an SEM. The alignment marks were used to locate the wires under study and to assess their orientation for the polarization analysis.

We now discuss the emission properties on a typical single wire. A μ-PL line scan along the wire axis is reported in figure 4(a) together with the corresponding SEM image. At the base of the wire, we observe the emission related to the donor-bound X_A exciton of relaxed GaN ($D^\circ X_A$) at 3.47 eV [25]. On the top of the wire, where the core/shell structure is located, two main contributions appear in the spectrum. The first peak centered around 3.53 eV is attributed to the strained GaN [16, 17] and a band at higher energy 3.7–3.8 eV is ascribed to the AlGaN shell. These attributions will be confirmed in section 4 by the polarization analysis and comparison with theoretical predictions. In addition, we observed a weak sub-bandgap emission below 3.4 eV related to donor–acceptor pair (DAP) transitions in AlGaN [26] or to interface defects [27].

The μ-PL spectra of figure 4(b) were recorded for $\parallel$ (electric field $\parallel$ to c-axis) and $\perp$ (electric field $\perp$ to c-axis) polarizations at 5 K in the intermediate region of the wire, where both core and core/shell contributions are present near the 13 μm position in figure 4(a). By rotating the polarization from $\parallel$ to $\perp$, we observed that the relative intensity of the peaks changes. The polarization ratio is defined as:

$$P = \frac{I_\perp - I_\parallel}{I_\perp + I_\parallel}$$

where $I_\parallel$ and $I_\perp$ are the integrated PL intensities for $\parallel$ and $\perp$ polarization, respectively. The peak related to the near band edge of relaxed GaN emission is maximal when the electric field is perpendicular to the c-axis with a polarization ratio of 0.62. The peak related to strained GaN is polarized parallel to the c-axis with a polarization ratio of -0.73. The PL arising from the AlGaN shell is slightly polarized perpendicular to the c-axis with a small polarization ratio of 0.09. The polarization diagrams of these three components are shown in the inset of figure 4(b). The polarization angular dependence can be well fitted by a cosine-squared law.

4. Theoretical considerations and discussion

The polarization properties are related to the valence band ordering and the selection rules of the related excitonic transitions. Thus, to predict the polarization behavior of the PL of a core/shell wire, we have calculated the valence band electronic states at the center of the Brillouin zone using a 6×6 $\mathbf{k} \cdot \mathbf{p}$ model including spin–orbit interaction under the quasi-cubic approximation [20]. To take into account the stress effects, we have used the Bir–Pikus approach as in [28]. The band structure parameters have been taken in agreement with Ghosh *et al* [28] for GaN and with Vurgaftman and Meyer [29] for AlN. All parameters for AlGaN are deduced by a linear interpolation between those of GaN and AlN, except for the bandgap, where a bowing parameter of 1 eV has been used [30]. The diagonalization method to determine the three excitonic transition energies is explained in detail in Ghosh *et al* [28]. The polarization ratio is then derived from the eigenstates of the Hamiltonian, assuming Boltzmann's statistics for the population of exciton states.

In the case of nanowires, the polarization properties of the emission are determined not only by the excitonic selection rules, but also by the dielectric index contrast between the nanowire and the surrounding medium [31]. However, possible influence of the nanowire shape on the polarization properties, which is very strong in GaN nanowires with a

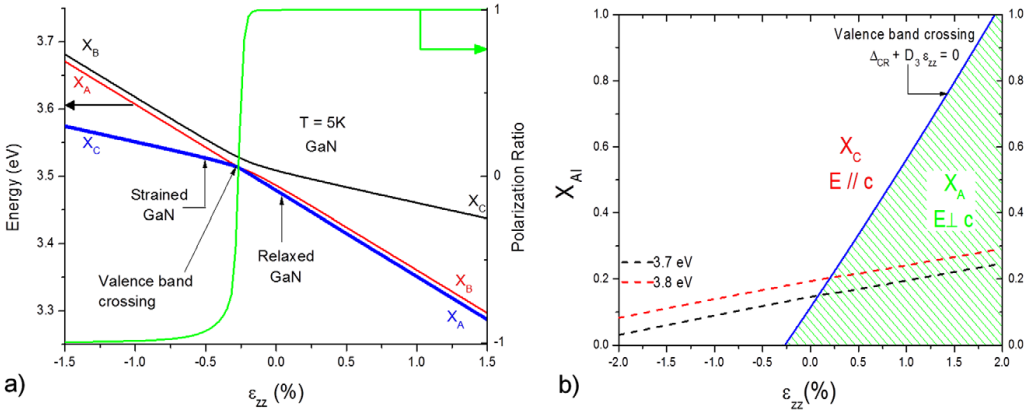

Figure 5. (a) Calculated excitonic transition energies as a function of uniaxial strain in GaN and polarization ratio of GaN near-band-edge emission (green line) depending on uniaxial strain along the *c*-axis for $T = 5$ K. (b) PL polarization diagram as a function of Al concentration and uniaxial strain. The dashed lines correspond to the experimentally observed emission energy of 3.7 eV and 3.8 eV, respectively. A schematic diagram of a AlGaN/GaN core/shell nanowire showing *z*-axis orientation is depicted in the inset.

small diameter [32], is expected to be negligible in the present case because the wires have a diameter above 100 nm [31]. Therefore, the polarization properties of AlGaN/GaN NWs can be completely understood in terms of valence band ordering.

As has been shown both theoretically and experimentally [17, 33, 34], in the case of AlGaN/GaN core/shell wires, the in-plane strain is typically about ten times smaller than the axial strain and the optical properties are governed by the axial strain. This is also confirmed by the XRD measurements on randomly oriented NWs with statistically significant *c*-axial compressive strain in the GaN core as determined in section 1. As for the AlGaN shell, the outer shell thickness in our case exceeds the critical value for a coherently strained nanowire [35] and we expect a partial strain relaxation in the shell via dislocations. The residual strain is assumed to remain uniaxial. The exact strain value in the AlGaN shell is very difficult to extract from microstructural analysis due to absence of the 'lattice parameters versus Al content' calibration curve for strain-free AlGaN alloys, which is further complicated by the compositional variation in the shells, both from wire to wire and within the same wire. In the following, we neglect the in-plane strain in the polarization analysis, i.e. $\varepsilon_{yy} + \varepsilon_{xx} \approx 0$ [33], taking z as the *c*-axis (the axis orientation is illustrated in the inset to figure 5(b) showing a schematic of a nanowire). The theoretical dependence of the three exciton energies in GaN on the uniaxial strain along z is shown in figure 5(a).

As observed in figure 5(a), at zero strain, the lowest excitonic transition is the X_A exciton, i.e. the topmost valence band is the A band. For increasing uniaxial compressive strain, A and C bands are getting closer and the crossing occurs at $\varepsilon_{zz} \approx -0.27\%$. The band crossing corresponds to the change of symmetry of the uppermost valence band from Γ_9 to Γ_7 [36]. A further increase of ε_{zz} values leads to a stronger C and A band separation.

As shown by Chuang *et al* [20], the excitonic transition implies each valence band and is characterized by a specific polarization: the X_A excitonic transition is polarized perpendicular to the *c*-axis whereas the X_C excitonic transition is polarized parallel to the *c*-axis. Hence, at low temperature, the polarization ratio changes rapidly around band crossing. As shown in figure 5(a), the polarization ratio for GaN near-band-edge emission changes its sign for axial strain around $\varepsilon_{zz} \approx -0.27\%$ due to the valence band re-ordering. As seen in figure 5(a), the PL arises from X_C excitons for $\varepsilon_{zz} < -0.27\%$ (strained GaN) and X_A excitons for $\varepsilon_{zz} > -0.27\%$ (relaxed GaN).

In the case of ternary AlGaN alloy, the band crossing between the A and C valence bands occurs for a value of strain that depends on the Al content. Following the 6×6 $\mathbf{k} \cdot \mathbf{p}$ theory, we can derive the condition of band crossing when $\varepsilon_{xy} = \varepsilon_{yz} = \varepsilon_{zx} = 0$:

$$\Delta_{\mathrm{cr}} + D_3 \varepsilon_{zz} + D_4(\varepsilon_{xx} + \varepsilon_{yy}) = 0$$

where Δ_{cr} is the crystal field splitting, D_3 and D_4 are deformation potentials.

In the approximation of negligible in-plane strain, this gives the following simplified condition:

$$\Delta_{\mathrm{cr}}(X_{\mathrm{Al}}) = -D_3(X_{\mathrm{Al}})\varepsilon_{zz}$$

where $\Delta_{\mathrm{cr}}(X_{\mathrm{Al}})$ and $D_3(X_{\mathrm{Al}})$ are functions of the Al content which change linearly from Δ_{cr}(GaN) (resp. D_3(GaN)) for $x = 0$ to Δ_{cr}(AlN) (resp. D_3(AlN)) for $x = 1$.

Figure 5(b) shows the dominant exciton [37] for wurtzite $Al_xGa_{1-x}N$ under uniaxial strain ε_{zz} as a function of Al content. The solid line shows the valence band crossing. From this diagram it is clear that the perpendicular polarization of $Al_xGa_{1-x}N$ ($x > 0.12$) X_A emission anticipates a tensile strain in the AlGaN shell.

The emission of relaxed GaN originating from the excitonic ($D^{\circ}X_A$) transition is predicted to be polarized

perpendicular to the *c*-axis in agreement with measurements. For strained GaN, our calculations predict that the observed PL energy at 3.53 eV corresponds to a strain state of GaN core around $\varepsilon_{zz} = -0.55\%$. For this value, we expect a negative polarization ratio in agreement with the PL measurements. Since the observed AlGaN emission is almost unpolarized, the diagram of figure 5(b) shows that the AlGaN strain is close to the valence band crossing line. Taking into account the observed AlGaN peak PL energy of 3.7–3.8 eV, we estimate the Al content and the relative strain of the $Al_xGa_{1-x}N$ shell as $x_{Al} \approx 15$–22% and $\varepsilon_{zz} \approx 0.20\%$, respectively. The estimated Al composition is compatible with the value deduced from the XRD and EDX measurements. Notably, the average strain value along the *c* axis in the GaN core found from XRD ($\varepsilon_{zz} \sim 0.056\%$) does not coincide with the $\varepsilon_{zz} \sim 0.55\%$ value found from μPL on a single wire. This discrepancy is most likely related to the fact that XRD has been performed on the whole ensemble of wires. In this case, the 5 μm thick GaN wetting layer on Si substrate as well as the uncovered wire bases and wires with thinner AlGaN shells also contribute to the position and broadening of the XRD peak for the strained GaN core. The shown μPL results, on the other hand, refer to a single wire with a thick AlGaN shell.

5. Conclusions

The polarization properties of wurtzite AlGaN/GaN core–shell nanowires have been investigated by means of spatially resolved polarization-dependent micro-photoluminescence. The experimental results are interpreted in terms of the strain-induced valence band crossing determined from the 6×6 $\mathbf{k}\cdot\mathbf{p}$ theory. In particular, we observe that the polarization of GaN photoluminescence changes from perpendicular to the *c*-axis for strain-free nanowire base part to parallel to the *c*-axis for compressively strained GaN core. The emission of AlGaN shell is weakly polarized perpendicular to the *c*-axis. This result shows that strain engineering in nanowire-based core/multishell n-GaN/n-AlGaN/p-AlGaN structures can be used to modify the emission polarization, which is of interest for optimizing the extraction efficiency in NW UV LEDs.

Acknowledgments

This work was supported by the French ANR agency under the programs ANR-08-BLAN-0179 NanoPhotoNit. GJ acknowledges financial support from the Ministère de l'Enseignement Supérieur et de la Recherche.

References

[1] Vilhunen S, Särkkä H and Sillanpää M 2009 *Environ. Sci. Pollut. Res.* **16** 439–42
[2] Morison W L 2005 *Phototherapy and Photochemotherapy of Skin Disease* (Boca Raton, FL: Taylor and Francis)
[3] Hirayama H, Tsukada Y, Maeda T and Kamata N 2010 *Appl. Phys. Express* **3** 031002
[4] Kneissl M *et al* 2011 *Semicond. Sci. Technol.* **26** 014036
[5] Nakarmi M L, Kim K H, Khizar M, Fan Z Y, Lin J Y and Jiang H X 2005 *Appl. Phys. Lett.* **86** 092108
[6] Nishida T, Saito H and Kobayashi N 2001 *Appl. Phys. Lett.* **78** 399
[7] Khizar M, Fan Z Y, Kim K H, Lin J Y and Jiang H X 2005 *Appl. Phys. Lett.* **86** 173504
[8] Atsushi Yamaguchi A 2010 *Appl. Phys. Lett.* **96** 151911
[9] Smith G A 2004 *J. Appl. Phys.* **95** 8247
[10] Dong Y, Tian B, Kempa T J and Lieber C M 2009 *Nano Lett.* **9** 2183–7
[11] Qian F, Gradecak S, Li Y, Wen C Y and Lieber C M 2005 *Nano Lett.* **5** 2287–91
[12] Jacopin G *et al* 2012 *Appl. Phys. Express* **5** 014101
[13] Fang Qian Y L, Li Y, Gradecak S, Park H-G, Dong Y, Ding Y, Wang Z L and Lieber C M 2008 *Nature Mater.* **7** 701–6
[14] Hersee S D, Rishinaramangalam A K, Fairchild M N, Zhang L and Varangis P 2011 *J. Mater. Res.* **26** 2293–8
[15] Bertness K A, Sanford N A and Davydov A V 2011 *IEEE J. Sel. Top. Quantum* **17** 847
[16] Schlager J B, Bertness K A, Blanchard P T, Robins L H, Roshko A and Sanford N A 2008 *J. Appl. Phys.* **103** 124309
[17] Rigutti L, Jacopin G, Largeau L, Galopin E, De Luna Bugallo A, Julien F H, Harmand J-C, Glas F and Tchernycheva M 2011 *Phys. Rev.* B **83** 155320
[18] Chen H Y, Yang Y C, Lin H W, Chang S C and Gwo S 2008 *Opt. Express* **16** 13465–75
[19] Ruda H E and Shik A 2006 *J. Appl. Phys.* **100** 024314
[20] Chuang S and Chang C 1996 *Phys. Rev.* B **54** 2491–504
[21] Bertness K, Roshko A, Mansfield L, Harvey T and Sanford N 2007 *J. Cryst. Growth* **300** 94–9
[22] Sanders A *et al* 2011 *Nanotechnology* **22** 465703
[23] Sanford A, Robins L H, Davydov A V, Shapiro A, Tsvetkov D V, Dmitriev A V, Keller S, Mishra U K and DenBaars S P 2003 *J. Appl. Phys.* **94** 2980
[24] Drouin D, Couture A R, Joly D, Tastet X, Aimez V and Gauvin R 2007 *Scanning* **29** 92–101
[25] Reshchikov M A and Morkoç H 2005 *J. Appl. Phys.* **97** 061301
[26] Li R *et al* 2009 *Appl. Phys. Lett.* **94** 211103
[27] Calleja E, Sánchez-García M, Sánchez F, Calle F, Naranjo F, Muñoz E, Jahn U and Ploog K 2000 *Phys. Rev.* B **62** 16826–34
[28] Ghosh S, Waltereit P, Brandt O, Grahn H and Ploog K 2002 *Phys. Rev.* B **65** 075202
[29] Vurgaftman I and Meyer J R 2003 *J. Appl. Phys.* **94** 3675
[30] Yun F, Reshchikov M A, He L, King T, Morkoç H, Novak S W and Wei L 2002 *J. Appl. Phys.* **92** 4837
[31] Ruda H E and Shik A 2006 *J. Appl. Phys.* **100** 024314
[32] Rigutti L *et al* 2010 *Phys. Rev.* B **81** 045411
[33] Hestroffer K *et al* 2010 *Nanotechnology* **21** 415702
[34] Laneuville V *et al* 2011 *Phys. Rev.* B **83** 115417
[35] Raychaudhuri S and Yu E T 2006 *J. Appl. Phys.* **99** 114308
[36] Gil B, Briot O and Aulombard R-L 1995 *Phys. Rev.* B **52** R17028
[37] Atsushi Yamaguchi A 2008 *Phys. Status Solidi* c **5** 2364–6

Sensors **2014**, *14*, 6338-6355; doi:10.3390/s140406338

OPEN ACCESS

sensors

ISSN 1424-8220

www.mdpi.com/journal/sensors

Article

Time-Resolved Photoluminescence Spectroscopy and Imaging: New Approaches to the Analysis of Cultural Heritage and Its Degradation

Austin Nevin [1,*], Anna Cesaratto [2], Sara Bellei [1], Cosimo D'Andrea [2,3], Lucia Toniolo [4], Gianluca Valentini [2] and Daniela Comelli [2]

[1] Istituto di Fotonica e Nanotecnologie—Consiglio Nazionale delle Ricerche (IFN-CNR), Dipartimento di Fisica, Politecnico di Milano, Piazza Leonardo da Vinci 32, 20133 Milano, Italy; E-Mail: sara.bellei@polimi.it

[2] Dipartimento di Fisica, Politecnico di Milano, Piazza Leonardo da Vinci 32, 20133 Milano, Italy; E-Mails: anna.cesaratto@polimi.it (A.C.); cosimo.dandrea@polimi.it (C.A.); gianluca.valentini@polimi.it (G.V.); daniela.comelli@polimi.it (D.C.)

[3] Center for Nano Science and Technology@PoliMi, Istituto Italiano di Tecnologia, Via Giovanni Pascoli 70/3, I-20133 Milano, Italy

[4] Dipartimento di Chimica, Materiali ed Ingegneria Chimica "G. Natta", Politecnico di Milano, via Mancinelli 7, 20131 Milano, Italy; E-Mail: lucia.toniolo@polimi.it

***** Author to whom correspondence should be addressed; E-Mail: austin.nevin@ifn.cnr.it; Tel.: +39-022-3996-187; Fax: +39-022-3996-126.

Received: 11 March 2014; in revised form: 31 March 2014 / Accepted: 31 March 2014 / Published: 2 April 2014

Abstract: Applications of time-resolved photoluminescence spectroscopy (TRPL) and fluorescence lifetime imaging (FLIM) to the analysis of cultural heritage are presented. Examples range from historic wall paintings and stone sculptures to 20th century iconic design objects. A detailed description of the instrumentation developed and employed for analysis in the laboratory or *in situ* is given. Both instruments rely on a pulsed laser source coupled to a gated detection system, but differ in the type of information they provide. Applications of FLIM to the analysis of model samples and for the in-situ monitoring of works of art range from the analysis of organic materials and pigments in wall paintings, the detection of trace organic substances on stone sculptures, to the mapping of luminescence in late 19th century paintings. TRPL and FLIM are employed as sensors for

the detection of the degradation of design objects made in plastic. Applications and avenues for future research are suggested.

Keywords: fluorescence lifetime imaging (FLIM); time-resolved fluorescence spectroscopy; cultural heritage; degradation; monitoring; semi-conductor pigments

1. Introduction

This work presents a review of the analysis of cultural heritage using time-resolved photoluminescence spectroscopy (TRPL) and fluorescence lifetime imaging (FLIM) which we illustrate through applied case studies. Both techniques are non-destructive and based on the use of ps or ns pulsed lasers and gated detection for the analysis of range of organic and inorganic materials.

1.1. Background of Photoluminescence Analysis of Works of Art

The analysis of works of art often begins with the visual examination of the surface of an object under UV light. This is because the spectrum of the optical emission from the surface as well as its spatial distribution in a field of view can provide conservators, art historians, and scientists key information regarding the presence of heterogeneities on a painting or a sculpture, signed papers or modern design objects. While the interpretation of fluorescence and the attribution of emissions to specific materials is far from trivial, both the spectrum of the emission, perceived as colour, and the spatial distribution of fluorescence are valuable starting points for further investigations. For example, conservators are experienced at relating differences in the fluorescence of surfaces to damage, to traces of materials (for example organic binders) which may provide insights regarding degradation or to past interventions, to the local applications of varnish (which tends to develop fluorescence with age) or to the presence of retouching (which is often dark when examined under UV light). Many materials found in cultural heritage fluoresce: indeed, stone substrates, organic pigments, binding media and waxes, conservation materials and semiconductors pigments have all been studied using fluorescence spectroscopy [1–10].

The luminescence from cultural heritage has long been utilized during routine inspection of paintings because it can be excited easily, with simple and low cost devices (lamps or LEDs); it is non-invasive, and can allow a reliable assessment of condition and the selection of suitable sampling locations for point-like analyses or sampling. The visual examination of works of art relies on the careful choice of both filtered UV-illumination and high-sensitivity color camera, providing a method for conservators to detect materials which may not be visible under normal lighting conditions. Typically, proper UV excitation is obtained with low-pressure UV lamps shielded with UV filters for suppressing the visible emission from the lighting devices; in these conditions, digital and analogue photography can provide spectacular images, as has recently been demonstrated during the analysis of wall paintings by Giotto in the Peruzzi Chapel (in the Basilica of Santa Croce, Florence, Italy) [11], where traces of original organic materials employed for paint and for gilding were revealed for the first time.

Many applications in the examination of works of art require the analysis of more quantitative parameters of the emission, including the emission spectrum of a material which reflects its chemical composition. The modification of the fluorescence of organic materials has been reported and related to general and more specific molecular changes, including those related to oxidation phenomena: for example, the photooxidation of protein-based binders [12], oils and varnishes [2], or the oxidation of modern polymers and plastics [13]. It is recognized, however, that the discrimination of materials on the basis of fluorescence spectra is often impossible—subtle spectral differences, which may arise from chemical modifications of materials or differences in molecular properties, may be masked by competing effects, auto-absorption phenomena [14], or scattering [15], for example. Fluorescence emissions may also be weak and thus spectra may be difficult to detect.

1.2. Time-Resolved Photoluminescence

In addition to the emission spectrum recorded from the surface of an object, the dynamics of the fluorescence, or luminescence, emission can be useful in the analysis and monitoring of cultural heritage and cultural heritage materials, which is the focus of the analysis presented in this article.

In simple terms, the emission process consists of the radiative decay from excited states of the chromophore. The emission lifetime can be interpreted as the average time the fluorophore stays in the excited state and hence provides information on the emission dynamics [16]. According to the nature of the excited state (singlet or triplet state) the lifetime can be extremely different varying from ps to ms. In the first case we generally refer to the emission process as fluorescence, while in the second case as phosphorescence. Both phenomena are generally summarized under the term luminescence.

Decay channels, from excited to ground state, can be classified as radiative and non-radiative. The emission decay depends on both radiative and non-radiative processes, because both of them influence the excited state population, leading to a strong dependence of the lifetime on the microenvironment of the fluorophore. In other terms, any interaction of fluorochromes with the microenvironment provides a specific emission quenching that is reflected by the emission lifetime. Therefore, this parameter carries clues about chemical changes (e.g., bond breaking) affecting the emitters due to oxidation, aging and other modifications of organic molecules. This represents one of the main advantages provided by the measurement of the fluorescence lifetime. Moreover, some emitters (e.g., fluorescent pigments) show specific fluorescence lifetimes, which can be considered characteristic.

Intensity measurements, especially those which are spectrally resolved, are affected by several drawbacks: first the presence of absorbers can severely extinguish the fluorescence signal and distort recorded spectral features. This is mainly true when dealing with paintings, because colors in the painted layer can strongly modify the emission from organic binders, which are often the main subject of the scientific investigation. Further, intensity measurements are affected by the spatial distribution of the excitation light, which is typically uneven, and by ambient light, which can seldom be avoided, unless measurements are done in complete darkness in the laboratory. For these reasons, fluorescence images may often be misinterpreted because areas with comparable chemical features appear different because of artifacts. In contrast the relaxation dynamics of the fluorescence or phosphoresce emission, like the tone of a sound, are almost insensitive to the intensity of the signal, provided that they can be reliably measured. Finally, time-resolved measurements are, at least on the first order, insensitive to

ambient light since any continuous wave light, being uncorrelated with excitation pulses, gives a negligible contribution to the signal in the very low duty cycle measurement gates, provided that the repetition rate used is below few kilohertz.

1.3. Overview of the Lifetime of Luminescent Materials in Cultural Heritage

Different organic materials can be found on cultural heritage objects, which include protein and oil-based binders, varnishes, restoration treatments, adhesives and glues. These materials are often luminescent due to the presence of delocalized electrons in molecules containing multiple aromatic rings or long-chains of conjugated double bonds. The related decay kinetics associated with these molecules is on the order of picoseconds or nanoseconds [1] and is highly affected by a number of factors, which include pH, temperature, solvent polarity and molecular flexibility. Similar lifetimes characterize the emission from natural organic pigments, such as lakes or diazo pigments, and synthetic organic dyes (including phtalocyanines and anthraquinones) [17,18].

A different decay behavior is detected in luminescent inorganic materials typically present on cultural heritage objects. For example, semiconductor pigments, such as cadmium- and zinc-based pigments, are typically characterized by a fast picosecond band gap emission, due to the recombination of an electron with a hole from the conduction to the valence bands. Moreover, trap state levels, present in these emitting molecules as a consequence of intrinsic and extrinsic defects, give rise to further radiative relaxation decay paths with a much longer temporal scale (typically on the order of microseconds) [19].

An example of luminescent materials employed in contemporary art is provided by "glow-in-the-dark" paints. These pigments are based on long-living phosphors, such as copper- or silver-activated zinc sulfide and, more recently, doped strontium aluminate, and typically glow a pale green to greenish blue color which can last for up to hours after exposure to UV excitation. A further interesting example of luminescent material is cuprorivaite, which forms the basis of the synthetic blue pigment first produced in the 4th Dynasty in Ancient Egypt, known as Egyptian blue. The pigment is strongly luminescent, with the emission ascribable to Cu^{2+} ions in the crystal matrix and characterized by a peak in the infrared (at 910 nm) and a reported luminescence decay time of 107 μs [20]. Similar emitting properties has been reported for other luminescent inorganic pigments, as those based on $BaCuSi_4O_{10}$ (Han blue) and $BaCuSi_2O_6$ (Han purple) [21].

The optical emission from stone sculptures and monuments is usually due to intrinsic defects in the mineral structure or to trapped impurities. For example in calcite, trace concentrations of ions from transition metals (Mn^{2+}) and rare-earth elements (including Tm^{3+} and Eu^{3+}) gives rise to phosphorescence emissions characterized by different decay kinetics (of the order of ms and μs for the former and the latter, respectively), which can be easily discriminated by time-resolved luminescence spectroscopy [10,22]. It has to be reported that, as marbles and stones are rather porous materials, the optical emission from stone artworks is also ascribed to adsorbed organic contaminants (including humic acids). Nevertheless, the different decay kinetics which characterize the intrinsic emission from stone and from exogenous organic contaminants, allow the easily discriminate between these two contributions, as will be better outlined in a case study discussed in a following section.

The values of typical emission lifetimes of luminescent materials are given in Table 1.

Table 1. Emission lifetimes of typical luminescent materials found in cultural heritage.

Material	Emitting Molecule or Process	Emission Lifetimes
Protein and oil-based binders, varnishes, adhesives and glues	Organic molecules	ps to tens of ns
Organic natural and synthetic pigments	Organic molecules	ps to tens of ns
Semiconductor pigments	Band gap recombination	ps to ns
	Trap levels	µs
Doped semiconductor pigments	Impurities	µs to hours
Minerals	Intrinsic or extrinsic defects in the crystal lattice	µs to ms

2. Methods

2.1. Fluorescence Spectroscopy and Fluorescence Imaging

Time-resolved fluorescence analysis requires pulsed excitation and gated detection. In this work femtosecond and nanosecond pulsed laser radiation at different wavelengths is employed for excitation. Detection for fluorescence lifetime imaging (FLIM) is provided by a time-gated imaging intensifier, while time-resolved photoluminescence spectroscopy (TRPL) relies on a picoseconds streak camera system.

Laser-induced fluorescence (LIF) has received significant attention for the analysis of pigments [3,6,23] and binding media [24,25]; indeed it has been employed for the measurement of the emission decay kinetics of samples only in few cases [8]. Laser excitation has distinct advantages over lamp illumination, such as brightness and monochromaticity, which allow fluorescence measurements without the need for filters to remove stray or parasitic blue radiation, as required when using mercury-based UV lamps. The choice of suitable excitation wavelength requires knowledge of the absorption properties of materials—for example, organic materials often absorb in the ultraviolet and emit in the visible range—while semiconductor pigments and trapped ions may be more efficiently excited with visible radiation and may emit in the visible and infrared region [15,26].

2.2. Description of Fluorescence Lifetime Imaging (FLIM)

The fluorescence lifetime imaging (FLIM) apparatus is comprised of a ns laser excitation source combined with a time-gated intensified camera (C9546-03, Hamamatsu Photonics, Hamamatsu City, Japan), capable of high speed gating to capture images of transient phenomena. A custom-built trigger unit and a precision delay generator (DG535 Stanford Research System, Sunnyvale, CA, USA) complete the system, giving rise to a net temporal jitter close to 0.5 ns.

The choice of the laser depends on the absorption properties of the investigated sample. Usually, a Q-switching frequency-tripled diode-pumped Nd:YAG laser (FTSS 355-50 Crylas GmbH, Berlin, Germany, λ = 355 nm, Pulse energy = 70 µJ, Pulse duration = 1.0 ns) is used in order to excite luminescence from materials absorbing in the UV range; different excitation wavelengths can be achieved by using a compact dye laser optically pumped by the UV laser radiation (FTSS Dye Lasers, Crylas GmbH, Berlin, Germany).

The laser beam is coupled to a silica optical fiber; the fiber tip is magnified with suitable optics in order to uniformly illuminate a circular area of about 25 cm in diameter, leading to a typical fluence per pulse kept below 140 nJ/cm^{-2} (well below any damage threshold).

The fluorescence decay is temporally sampled by the image intensifier, whose gate width is adjustable from 3 ns to continuous mode, depending on the kinetic properties of the sample or surface under investigation. Usually, a 10 ns gate width is applied to detect the nanosecond kinetic of the emission from organic materials, but long-lived decay kinetics, on the order of the microsecond and millisecond, can be more effectively sampled by increasing the width of the gate window. The fluorescence signal within the gate window is then intensified by the MCP intensifier and accumulated by a CCD camera (QImaging Retiga 2000R fast, Cooled Mono 12-bit, Surrey, BC, Canada). This procedure is repeated at different delays between the excitation pulses and the leading edge of the gate, thus leading to a sequence of fluorescence images taken at different times (Figure 1).

Figure 1. A timing diagram showing pulsed laser excitation, luminescent emission, and operation of the intensifier gate. The acquisition of luminescent images at different delays with respect to the laser pulse (purple). The intensity of the luminescence (red) decreases in time. The images recorded highlight the presence of a long-lived emission (>1,000 ns). Intensity in insets has been rescaled to fill the dynamic range of each image.

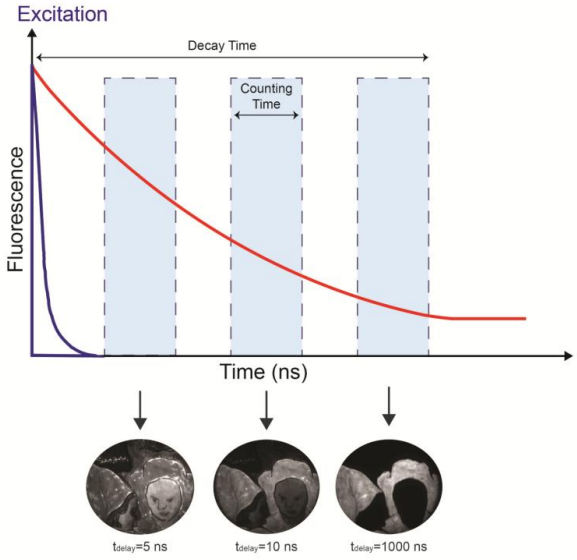

The FLIM device is not spectrally resolved: in fact the image detector, based on an input multialkali photocathode, allows the detection of all photons emitted in the 400–900 nm spectral range. In order to select emission from specific spectral regions, a suitable band pass optical filter can be mounted in front of the image intensifier. The whole system has been assembled in a portable rack of about 60 × 60 × 70 cm, except for the gated camera that is connected to the control unit through a 10 m cable and a 40 m fiber optic, for remote access during in situ investigations. The long optical fiber allows an easy synchronization of the electronic gate with laser pulses in an almost jitter free configuration.

The lifetimes are subsequently calculated pixel-by-pixel, and then their spatial variations are displayed in a false colour representation. As a general feature, the more time samples are taken, the better is the estimate of the lifetime. Luminescence can seldom be modeled as a mono-exponential decay due to the simultaneous presence of several fluorescent species and different non-radiative relaxation paths. Nevertheless, the reconstruction of the effective lifetime map based on a simple mono-exponential decay model is typically the optimal choice for our investigations [27]. In fact, it leads to a single map that yields strong spatial contrast for the discrimination of different compounds and benefits from intensity independence. Moreover, the mono-exponential fitting algorithm is suitable for real-time data processing. Refined models (bi-exponential decay, multi-exponential decay, stretched exponentials) can be also applied to time-resolved data. Nonetheless, an extensive dataset and a much longer fitting time are required and still the fitting may be compromised by insufficient signal-to-noise ratio of data.

2.3. Time-Resolved Photoluminescence Spectroscopy

Time-resolved photoluminescence (TRPL) analysis consists in the measurement of the evolution of the luminescence spectrum over time. In contrast to FLIM, TRPL spectroscopy studies the luminescence emission from a single point in the sample and not from an entire image. Different set-ups can be built to perform TRPL analysis. All of them combine: (a) a pulsed laser source; (b) a triggering system; (c) a proper optical path to deliver the laser pulse to the sample; (d) light collecting optics; (e) a spectral dispersive element; (f) a detector unit. In particular, in Conservation Science, a time-gated Optical Multichannel Analyzer (OMA) [27,28], a fast streak camera based system [28], and a portable Time-Correlated Single Photon Counting (TCSPC) apparatus [17] have been employed in the past for the analysis of the spectrally-resolved luminescence decay kinetics of pigments and binding media. The time-resolved photoluminescence (TRPL) measurements reported in this article were carried out using streak camera-based instrumentation. A scheme of the set-up is shown in Figure 2.

Figure 2. The TRPL setup. ND: neutral density attenuator; PD: photodiode; FI: Faraday isolator; PCF: photonic crystal fiber; FM flipping mirror; BBO: type I β-barium borate crystal; F1: low pass filter; DM: dichroic mirror; Obj.: microscope objective; F2: high pass filter.

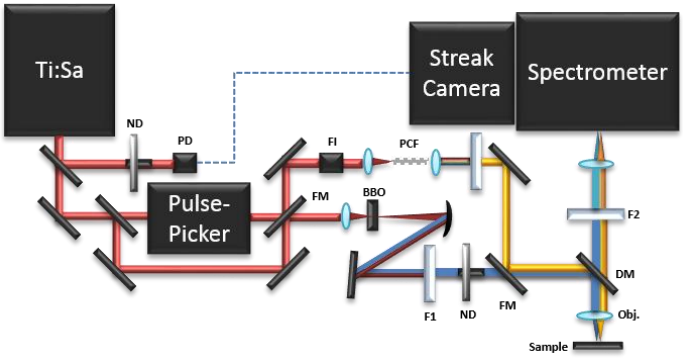

The pulsed excitation source consists of a passive mode-locking Ti:Sapphire laser (Chameleon Ultra II, Coherent, Santa Clara, CA, USA) tunable from 680 to 1,080 nm and emitting 140 fs pulses with a maximum energy of about 50 nJ. The laser repetition rate is 80 MHz and can be reduced down to 1 kHz by letting the beam pass through an acousto-optical modulating pulse picker (APE). To extend the excitation wavelength into the UV and visible ranges, a 1 mm type I β-barium borate crystal frequency-doubles the optical signal (340–540 nm). By using of a thin absorbing filter (BG38, Schott AG, Mainz, Germany) the residual fundamental is removed. In order to cover the remaining gap in the visible wavelength range (540–680 nm), a pulsed supercontinuum (SC) is generated by focusing the light pulses at 780 nm, by means of an aspheric singlet lens (C150TM, Thorlabs GmbH, Dachau, Germany), into a 20 cm long Photonic Crystal Fiber (PCF) (NL-2.4-800, Blaze Photonics Limited, Blaze Photonics Limited, Bath, UK). PCF consists of a silica fiber with a core (diameter of about 2.4 μm) surrounded by a mesh of air-filled holes. SC is generated over the spectral range 480–1100 nm through a combination of several nonlinear phenomena in the PCF [29]. The desired wavelength range is sliced from the broad SC spectrum using a suitable interference filter. In order to avoid back reflection into the Ti:Sapphire cavity, a Faraday Isolator is used before focusing into the PCF.

The light pulses are delivered into a custom-built epi-fluorescence microscope based on a dichroic mirror, chosen on the basis of the excitation wavelength, and a proper long working distance objective lens. The fluorescence radiation is collected by the same objective, filtered by a proper long pass filter to remove residual excitation light, and focused into the entrance slit of an imaging spectrometer (focal length 300 mm, f/3.9, 50 lines/mm grating, Acton SP2300, Princeton Instruments, Trenton, NJ, USA) with a spectral resolution of about 1 nm. The spectrometer is coupled to a streak camera detector (C5680, Hamamatsu Photonics, Hamamatsu, Japan), triggered by delivering a small portion of the laser beam to a photodiode. The streak camera detector can work in two different modalities, according to the required temporal range and related temporal resolution. The highest temporal resolution of about 2 ps can be reached in synchroscan operation mode working at 80 MHz repetition rate [30]. When it is necessary to study longer time decays, the slow sweep acquisition mode can be employed, with a maximum temporal resolution of about 50 ps and a highest repetition rate of 2 MHz [31].

3. Case Studies

In the following section, a short review of applied cases is given to highlight the effectiveness of the time-resolved approach to the analysis of luminescence. Without any claim for completeness, the examples range from model samples and Renaissance paintings to modern pigments and polymeric materials, sharing a similar approach that reveals many advantages.

3.1. FLIM of Model Samples and Organic Materials

The analysis of organic materials has long received attention using fluorescence spectroscopy, and has included time-resolved approaches [3,8,32]. The analysis of binding media—which contain proteins (egg white, animal glue and casein) and lipids (drying oils), mixed media (egg yolk which contains both proteins and lipids), as well as varnishes—has suggested that differences in media are appreciable in time-resolved spectra. Different amino acids or degradation products in proteins, and the

formation of conjugated bonds and chromophores in oils and resins give rise to the observed fluorescence and to different fluorescence lifetimes.

The analysis of protein-based binding media like egg white, collagen-based glue and egg yolk, performed with FLIM can highlight differences in the fluorescence lifetime according to media. For example, while the fluorescence of egg white and collagen-based glues is greater than 5.5 ns, egg yolk, which also contains fatty acids, the oxidation of which gives rise to the formation of new fluorophores, is associated with a shorter fluorescence lifetime (Figure 3).

Figure 3. Fluorescence lifetime of (**a**) egg white; (**b**) collagen-based glue; (**c**) egg yolk.

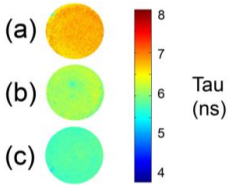

A set of painted model samples containing whole egg mixed with linseed oil as the binder and lead white with significant concentrations of other pigments (copper-containing carbonate pigments and madder lake), painted *a fresco* and *a secco*, was analyzed with FLIM (Figure 4). The analysis of the model samples is of interest for a better comprehension of the interactions between a binder and the surrounding micro-environment. Indeed, the influence of pigments on the detected fluorescence depends on a number of factors which include the optical absorption of the pigment [15,33], possible luminescence of the pigment, and chemical interactions (e.g., quenching) between the binder and pigment and between the binder and the substrate [16]. Copper (II) ions are well-known quencher for fluorescence, and it has been shown that they influence the fluorescence spectrum of protein-based binding media [12]. Basic lead carbonate ($2PbCO_3$ Ꝑ$Pb(OH)_2$, lead white) can react with fatty acids to form lead soaps [34]. Madder lake is a fluorescent pigment which emits around 610 nm [35] and has a short fluorescence lifetime (on the order of few ns) [17,36].

Figure 4. FLIM analysis (shown in false colour in circular insets) from a model sample painted in different mixtures of pigments in an egg yolk + linseed oil binder applied either to dry plaster (*secco*) or to fresh plaster (*fresco*).

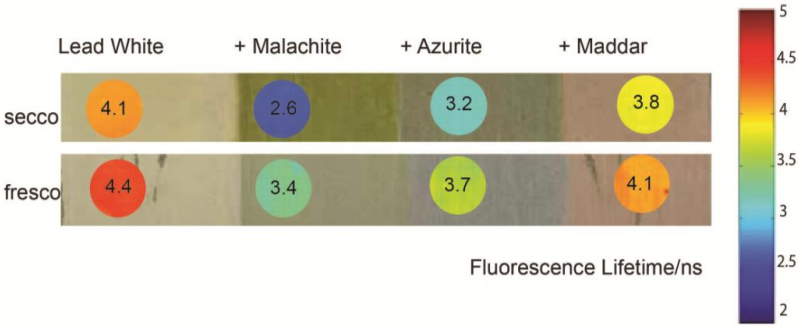

Although the general shape of the spectra of the different samples containing egg-oil mixed with pigments is similar (data not shown), the fluorescence lifetime is different for each mixture. The presence of madder has the effect of reducing the fluorescence lifetime with respect to areas painted in lead white; this is ascribed to the contribution of emissions from the lake pigment, which, on its own has a lifetime of approximately 1.5 ns [17]. The copper-based pigments significantly reduce the fluorescence lifetime, and this could be due to the quenching of fluorescence by Cu^{2+} ions, which may occur by a Förster resonance energy transfer (FRET) mechanism [37]. The fluorescence lifetime of paint containing malachite is shorter than that observed in azurite-containing paint, which may be related to the slightly greater solubility of the pigment in the oil-egg mixture [38], as well as the greater concentration of malachite compared to azurite in the sample, resulting in an increased quenching of the binder emission lifetime. Finally, areas painted *a fresco* have increased fluorescence lifetime with respect to those painted *a secco*. The reason behind this phenomenon is not certain; however, it has been shown that calcium ions increase the fluorescence lifetime of amino acids and other fluorophores [39]. Therefore, it is possible that the increase in fluorescence lifetime in areas painted *a fresco* is due to the interaction between Ca^{2+} and fluorophores present in binding media.

3.2. Analysis of Pigments and Paintings

3.2.1. Organic Lake Pigments

The presence of an organic lake pigment was successfully mapped using FLIM on a Renaissance wall painting by Masolino da Panicale (1383–1447). The analysis was part of a three year monitoring campaign on the paintings of the Baptistery of Castiglione Olona (Varese, Italy) and it was combined with other advanced imaging techniques and with laboratory analyses on an historical micro-sample from the painted surface [40]. The FLIM maps were obtained from various areas, but the most interesting information came from the figure of Salome, as reported in Figure 5.

In particular, in Salome's headdress (shown in Figure 5a) it is possible to discern a dot in the center of two of the ovals. In these areas the lifetime is shorter (effective τ close to 3.1 ns) compared with the one detected in the surrounding area (effective τ close to 3.5 ns). The measurement of the lifetime is difficult to interpret and not strictly analytical by itself, but when combined with the spectrally resolved fluorescence imaging device and a photograph (taken in 1932 before the restoration conducted by Pellicioli and della Rotta) it allows us to understand more about the physical history of the wall paintings. The emission from the headdress was ascribed to an anthraquinone-based lake pigment mixed with an organic binder. The shorter emission lifetime from the dots was explained with a higher content of the red lake pigment with respect to the binder, added to the painting as *a secco* decorations, which are no longer visible to the naked eye. The hypothesis was extended to the dress worn by Salome (Figure 5b), which was probably decorated with same lake-based vertical stripes in order to give a tridimensional volume to the entire figure.

Figure 5. FLIM analysis of the wall painting of the Life of John the Baptist (Colleggiata, Castiglione Olona, Varese, Italy) by Masolino: the fluorescence lifetime maps taken from the figure of Salome were superimposed on the color image. In the ovals of the headdress (**a**) and in the vest (**b**) areas with different lifetimes can be discriminated, which are related to a different content of red lake.

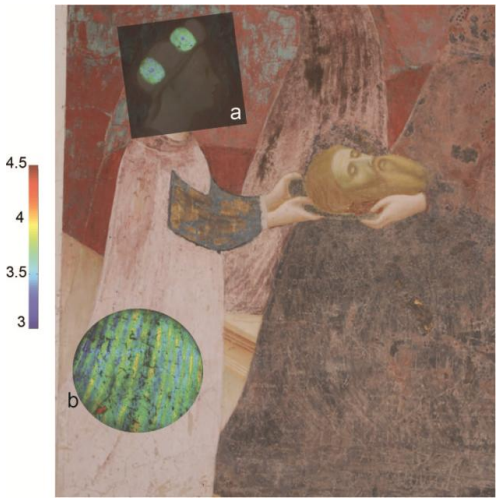

3.2.2. Semi-Conductor Pigments Based on Cadmium and Zinc

During the 19th century, cadmium-based pigments were rapidly adopted by artists as they were bright and had a particularly high covering power [41]. Different shades of cadmium pigments were available and varied from light yellow to deep red on the basis of the chemical composition: the lighter colours are based on cadmium sulphide ((Cd,Zn)S), while the deeper shades are based on cadmium sulphoselenide (Cd(S,Se)). The two compounds belong to the IIb-VIa semiconductor group and are characterized by a large band gap energy and a direct transition [19,42].

A group of sixteen commercially-available modern cadmium-based pigments, which are binary alloys of ZnS and CdS ($Zn_{1-x}Cd_xS$ with $0 < x < 1$), and of CdS and CdSe (CdS_xSe_{1-x} with $0 < x < 1$), were studied in the laboratory with the TRPL device opening new frontiers both for the characterization of the material itself and for the understanding of their degradation paths. Our attention focused on the photoluminescence emissions from the band edge (E_g) and the first deep trap state (E_{t1}) [19,42], respectively related to the crystal lattice and to defects and vacancies present in it. The time-resolved analysis permitted a deeper study of this class of pigments compared to the spectrally resolved results obtained in previous studies [6,42]. The gated spectra and the emission decay kinetics from one of the yellow shades are presented in Figure 6.

The band edge emission (E_g), with a maximum peak between 476 nm and 630 nm for the various samples, has a lifetime on the order of picoseconds and can be used to discriminate between the two different pigment compositions, since there is at least a 10 ps difference in the τ, with emission from CdS pigments decaying more rapidly than that from CdSe. Secondly, the trap state emission (E_{t1}),

characterized by a λ_{Peak} between 660 nm and 800 nm, presents a μs decay profile, without a direct correlation with the pigments composition.

Figure 6. TRPL analysis of a yellow ((Zn,Cd)S) sample: gated PL spectra (**a**) in the 0–7 ps and 8–36 ps temporal windows; (**b**) decay kinetic from the band edge (475–505 nm); (**c**) gated PL spectra in the 0–3 μs and 10–12.5 μs temporal windows; (**d**) decay kinetic from the first trap state (640–740 nm).

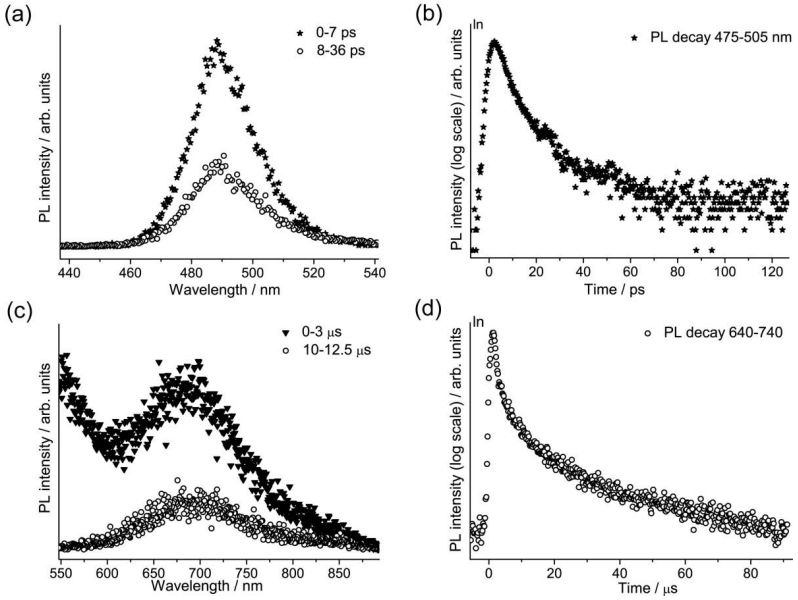

Other semiconductors found in paint are based on zinc calcogenides—the white pigments zinc oxide (ZnO), zinc sulphide (ZnS) and lithopone (ZnS + $BaSO_4$), which were all produced on a massive scale during the 19th C and 20th C. Due to the intensity, purity, cost and covering power, zinc-based whites often outclassed the traditional pigment white lead. In-situ lifetime imaging was employed for the mapping of a white luminescent pigment present on Van Gogh's painting "Les bretonnes et le pardon de pont Aven" [43]. For these investigations, the gating window of the intensified camera was set to 100 ns, and the emission decay was recorded from 0 to 1,000 ns with a variable sampling step. The dynamics of the decay of the luminescent pigment, analysed with a multiexponential decay model assuming a maximum of three discrete components, highlighted a very long-lived emission at 520 nm with an effective lifetime close to 1,100 ns that we ascribe to traces of ZnS with the presence of Cu ions unintentionally introduced during the pigment manufacturing. Indeed, well into the 20th century metal impurities were often introduced into the crystal matrix of the pure substances depending on the method of synthesis and purification of raw materials.

3.3. Analysis of Works on Stone

The FLIM device has been applied to the analysis of marble sculptures, with most important studies including the investigation of two Michelangelo's masterpieces, the David and the Piet à Rondanini.

In all cases, the time gated imaging camera was set in the nanosecond gating mode in order to filter out the long-living luminescence from marble. As was outlined in the introduction, minerals often emit a characteristic luminescence with lifetimes from microseconds to milliseconds, ascribable to impurities located inside the crystal lattice of the material, such as Mn^{2+} ions substituting for Ca^{2+} ions in calcite. This working principle allowed us the detection of the nanosecond emission from organic compounds which have been absorbed in the porous marble matrix. For example, analysis of different areas of Michelangelo's David revealed the presence of an intense nanosecond emission heterogeneously distributed on the sculpture surface. Areas with lifetimes close to 6 and 4.5 ns were detected and, with the aid of complementary Fourier Transform Infrared Spectroscopy (FTIR) of samples, allowed the mapping of beeswax (which has a longer lifetime), which permeates most of the statue surface, and of calcium oxalate deposits (shorter lifetime) in vertical patterns. The former organic contaminant was ascribed to a beeswax-based conservation treatment carried out in 1813 on the sculpture. Oxalate accumulation was likely due to the outdoor display of the David until 1873, when the statue was moved inside the museum (Galleria dell'Accademia, Florence, Italy) where it is today. The shorter mean lifetime from areas with the inorganic deposits could be due to traces of fluorescent compounds in the patina with a lifetime shorter than that of beeswax.

3.4. Applications to Polymer-Based Materials

Recently, both FLIM and TRPL have been extended to the monitoring of polymers and their degradation [44]. A range of polymers can be found in cultural heritage, and the changes in chemical properties of modern materials—whether those found in design objects or museum collections, or materials based on polymers which are used for conservation treatments (such as adhesives or consolidants)—are of particular concern. FLIM and TRPL are both useful tools for monitoring changes in luminescence which may develop or change with polymer degradation. For example, the photo-oxidation of acrylonitrile butadiene styrene (ABS) has been shown to lead to significant modifications of the fluorescence spectrum and the fluorescence lifetime. On the ps time scale, the lifetime of fluorescence related to styrene is reduced, which is ascribed to modifications of the molecular weight of ABS. In objects made of ABS, FLIM is useful for the identification of differences in formulation (and the presence, for example, of optical brighteners and other impurities) in objects made of different parts in ABS, as well as the build-up of longer-lived fluorophores (with lifetimes of *ca*. 5 ns) due to degradation.

4. Discussion

Time-resolved luminescence techniques applied to the analysis of cultural heritage provide a rapid means for differentiating materials, mapping distribution or, in some cases, detecting chemical changes. The real strength in FLIM is that it gives quantitative measurements with a portable and versatile instrument and the fact that new information, which complements steady-state fluorescence imaging, can be obtained regarding the nature of luminescent materials on a surface. The distribution of trace original materials (for example the fluorescent pigments in wall paintings by Masolino, or the phosphorescent white semi-conductor pigments present in an impressionist painting by Van Gogh) can be mapped rapidly and in conditions which do not require complete darkness, which is a distinct

advantage for the in situ analysis of cultural heritage artworks. In other cases, added materials, like wax (in the case of the David) or organic binding media (for example shown in replicas of wall paintings) may be responsible for signal detected by FLIM. While ps-resolved analysis using a streak camera is confined to the laboratory, analysis of pigments and polymers demonstrates how fluorescence spectra shift, how fluorescence lifetime changes with degradation or how it may depend on pigment manufacture. Indeed, time-resolved fluorescence has proved to be an optimal sensor for specific materials (including semiconductors) found in cultural heritage.

Despite these advantages, the interpretation of changes in emission lifetime is complex, and it is made more so due to the heterogeneity intrinsic in artist materials and works of art. Indeed it is often useful to employ complementary elemental and molecular analyses for a better understanding of chemical differences associated with different time-resolved emissions. Some non-invasive instrumentation can be utilised for this purpose, and this has become more straightforward with the introduction of commercial non-destructive instrumentation, as has been shown in many projects (including, for example, the Cultural Heritage Advanced Research Infrastructures (CHARISMA) project [45]). Nonetheless, it is rarely possible to precisely ascribe modifications in fluorescence lifetime in complex materials without fundamental studies of reference materials which, albeit pure, are far removed from the complex surfaces encountered in works of art. Current research is focusing on fundamental studies of the interactions of organic and inorganic materials in model paintings using a range of instrumentation including TRPL.

Data analysis and processing are an important part of FLIM and TRPL—as is the careful selection of experimental conditions. In addition, the optoelectronic components which are part of the FLIM and TRPL device and the laser-excitation both limit the availability of the techniques for routine analysis. Technological advances in time-resolved detecting systems have recently been quite impressive, with the introduction of compact low-cost SPAD arrays for TCSPC measurements. Indeed, biological and medical applications could drive technology and the development of very compact and low cost time-resolved imaging devices.

4. Conclusions and Outlook

In this work applications of FLIM and TRPL to cultural heritage have been presented along with technical details regarding their implementation. The techniques can provide useful information about a range of inorganic and organic materials either in situ (FLIM) or in the laboratory (TRPL), as has been illustrated with applied case studies. While the data acquired may be difficult to interpret and ascribe, it can inform sampling or further analysis. Both techniques are ideally suited to monitoring as they are non-destructive and luminescence has been shown to change as a consequence of material degradation. Future applications of FLIM should focus on the study of a larger range of semiconductor materials, including historic samples, as well as on other long-lived luminescent materials (for example Egyptian blue) found in art. As the imaging device can be easily adapted to an optical microscope, analyses should be extended to the micro scale for the study of pigment particles. Finally, spectral extensions of the detection systems used for TRPL will allow the monitoring of oxidation of organic materials which emit in the UV (for example amino acids and small aromatic molecules present in binding media and plastics).

Acknowledgments

Research presented has been partially funded through the Italian Ministry for Univeristies and Research (MIUR) Future in Research (FIRB) project FUTURAHMA: Tecniche pittoriche, critica delle varianti e problemi conservativi. Tra Futurismo e ritorno al classico (1910–1922) (RBFR12PHL4_003) which is gratefully acknowledged. Analysis of model samples of wall paintings was carried out as part of the Organic Materials in Wall Paintings (OMWP) project coordinated by the Getty Conservation Institute. Analysis of semiconductor pigments was partially founded within the international Joint Program Initiative Cultural Heritage LeadART.

Author Contributions

All authors have contributed to research and writing this article. Nevin has coordinated the publication, and carried out analysis of organic materials and analysis of works of art. Comelli, Valentini and D'Andrea were responsible for instrumental development, analysis of samples and interpretation of results. Toniolo has worked on case studies. Cesaratto has worked both on Time-resolved measurements and the analysis of data; Bellei has worked on the analysis of pigments and the preparation of the manuscript.

Conflicts of Interest

The authors declare no conflict of interest.

References

1. Nevin, A.; Spoto, G.; Anglos, D. Laser spectroscopies for elemental and molecular analysis in art and archaeology. *Appl. Phys. A* **2012**, *106*, 339–361.
2. De la Rie, R. Fluorescence of paint and varnish layers (part I-II-III). *Stud. Conserv.* **1982**, *27*, 1–7, 65–69, 102–108.
3. Miyoshi, T.; Ikeya, M.; Kinoshita, S.; Takashi, K. Laser-Induced Fluorescence of Oil Colours and Its Application to the Identification of Pigments in Oil Paintings. *Jpn. J. Appl. Phys.* **1982**, *21*, 1032–1036.
4. Bottiroli, G.; Gallone-Galassi, A.; Bernacchi, E. Microspectrofluorometric techniques as applied to the analysis of binding media and varnishes in color samples taken from paintings. In Proceedings of the Symposium on Scientific Methodologies Applied to Works of Art, Florence, Italy, 2–5 May 1984; pp. 168–170.
5. Larson, L.J.; Shin, K.K.; Zink, J.I. Photoluminescence Spectroscopy of Natural Resins and Organic Binding Media of Paintings. *J. Am. Inst. Conserv.* **1991**, *30*, 89–104.
6. Anglos, D.; Solomidou, M.; Zergiotti, I.; Zafiropulos, V.; Papazoglou, T.; Fotakis, C. Laser-Induced Fluorescence in artwork diagnostics: An application in pigment analysis. *Appl. Spectrosc.* **1996**, *50*, 1331–1334.
7. Thoury, M.; Elias, M.; Frigerio, J. M.; Barthou, C. Nondestructive varnish identification by ultraviolet fluorescence spectroscopy. *Appl. Spectrosc.* **2007**, *61*, 1275–1282.

8. Nevin, A.; Comelli, D.; Valentini, G.; Anglos, D.; Burnstock, A.; Cather, S.; Cubeddu, R. Time-resolved fluorescence spectroscopy and imaging of proteinaceous binders used in paintings. *Anal. Bioanal. Chem.* **2007**, *388*, 1897–1905.
9. Nevin, A.; Comelli, D.; Valentini, G.; Cubeddu, R. Total Synchronous Fluorescence Spectroscopy Combined with Multivariate Analysis: Method for the Classification of Selected Resins, Oils, and Protein-Based Media Used in Paintings. *Anal. Chem.* **2009**, *81*, 1784–1791.
10. Gaft, M.; Reisfeld, R.; Panczer, G. Laser-induced time-resolved luminescence of minerals. *Spectrochim. Acta. A. Mol. Biomol. Spectrosc.* **1998**, *54*, 2163–2175.
11. Frosinini, C. Giotto in Florence: Shedding light on the Peruzzi Chapel. Available online: http://www.nga.gov/content/dam/ngaweb/research/CASVA/pdfs/center-33.pdf (accessed on 1 March 2014).
12. Nevin, A.; Anglos, D.; Cather, S.; Burnstock, A. The influence of visible light and inorganic pigments on fluorescence excitation emission spectra of egg-, casein- and collagen-based painting media. *Appl. Phys. A* **2008**, *92*, 69–76.
13. Toja, F.; Saviello, D.; Nevin, A.; Comelli, D.; Lazzari, M.; Levi, M.; Toniolo, L. The degradation of poly(vinyl acetate) as a material for design objects: A multi-analytical study of the effect of dibutyl phthalate plasticizer. Part 1. *Polym. Degrad. Stab.* **2012**, *97*, 2441–2448.
14. Elias, M.; Magnain, C.; Barthou, C.; Nevin, A.; Comelli, D.; Valentini, G. UV-fluorescence spectroscopy for identification of varnishes in works of art: Influence of the underlayer on the emission spectrum. In Proceedings of SPIE Vol. 7391, O3A: Optics for Arts, Architecture, and Archaeology II, Bellingham, WA, USA, 2009.
15. Verri, G.; Clementi, C.; Comelli, D.; Cather, S. Correction of Ultraviolet-Induced Fluorescence Spectra for the Examination of Polychromy. *Appl. Spectrosc.* **2008**, *62*, 1295–1302.
16. Lakowicz, J.R. *Principles of Fluorescence Spectroscopy*, 3rd ed.; Springer: London, UK, 2006.
17. Romani, A.; Clementi, C.; Miliani, C.; Brunetti, B.G.; Sgamellotti, A.; Favaro, G. Portable equipment for luminescence lifetime measurements on surfaces. *Appl. Spectrosc.* **2008**, *62*, 1395–1399.
18. Grazia, C.; Clementi, C.; Miliani, C.; Romani, A. Photophysical properties of alizarin and purpurin Al(III) complexes in solution and in solid state. *Photochem. Photobiol. Sci.* **2011**, *10*, 1249–1254.
19. Cesaratto, A.; D'Andrea, C.; Nevin, A.; Valentini, G.; Tassone, F.; Alberti, R.; Frizzi, T.; Comelli, D. Analysis of cadmium-based pigments with time-resolved photoluminescence. *Anal. Methods* **2014**, *6*, 130–138.
20. Accorsi, G.; Verri, G.; Bolognesi, M.; Armaroli, N.; Clementi, C.; Miliani, C.; Romani, A. The exceptional near-infrared luminescence properties of cuprorivaite (Egyptian blue). *Chem. Commun. (Camb).* **2009**, 3392–3394.
21. Pozza, G.; Ajo, D. Photoluminescence of the inorganic pigments Egyptian blue, Han blue and Han purple. *J. Cult. Herit.* **2000**, *1*, 393–398.
22. Mason, R.; Clouter, M.; Goulding, R. The luminescence decay-time of Mn^{2+} activated calcite. *Phys. Chem. Miner.* **2005**, *32*, 451–459.

23. Castillejo, M.; Martin, M.; Oujia, M.; Silva, D.; Torres, R.; Manousaki, A.; Zafiropulos, V.; Van den Brink, O.F.; Heeren, R.M.A; Teule, R.; *et al*. Analytical study of the chemical and physical changes induced by KrF laser cleaning of tempera paints. *Anal. Chem.* **2002**, *74*, 4662–4671.
24. Nevin, A.; Cather, S.; Anglos, D.; Fotakis, C. Analysis of protein-based binding media found in paintings using laser induced fluorescence spectroscopy. *Anal. Chim. Acta* **2006**, *573–574*, 341–346.
25. Miyoshi, T. Fluorescence from Varnishes for Oil Paintings under N_2 Laser Excitation. *Jpn. J. Appl. Phys.* **1987**, *26*, 780–781.
26. Bridgman, C.F.; Gibson, H. Lou Infrared luminescence in the photographic examination of paintings and other art objects. *Stud. Conserv.* **1963**, *8*, 77–83.
27. Comelli, D.; D'Andrea, C.; Valentini, G.; Cubeddu, R.; Colombo, C.; Toniolo, L. Fluorescence lifetime imaging and spectroscopy as tools for nondestructive analysis of works of art. *Appl. Opt.* **2004**, *43*, 2175–2183.
28. Borgia, I.; Fantoni, R.; Flamini, C.; Di Palma, T.M.; Guidoni, A.G.; Mele, A. Luminescence from pigments and resins for oil paintings induced by laser excitation. *Appl. Surf. Sci.* **1998**, *127–129*, 95–100.
29. D'Andrea, C.; Spinelli, L.; Bassi, A.; Giusto, A.; Contini, D.; Swartling, J.; Torricelli, A.; Cubeddu, R. Time-resolved spectrally constrained method for the quantification of chromophore concentrations and scattering parameters in diffusing media. *Opt. Express* **2006**, *14*, 1888–1898.
30. Dozzi, M.V.; D' Andrea, C.; Ohtani, B.; Valentini, G.; Selli, E. Fluorine-Doped TiO_2 Materials : Photocatalytic Activity vs Time- Resolved Photoluminescence. *J. Phys. Chem.* **2013**, *117*, 25586–25595.
31. Li, H.; Brescia, R.; Krahne, R.; Bertoni, G.; Alcocer, M.J.P.; D' Andrea, C.; Scotognella, F.; Tassone, F.; Zanella, M.; De Giorgi, M.; Manna, L. Blue-UV-Emitting ZnSe(Dot)/ ZnS(Rod) Core/Shell Nanocrystals Prepared from CdSe/CdS Nanocrystals by Sequential Cation Exchange. *ACS Nano* **2012**, *6*, 1637–1647.
32. Nevin, A.; Echard, J.-P.; Thoury, M.; Comelli, D.; Valentini, G.; Cubeddu, R. Excitation emission and time-resolved fluorescence spectroscopy of selected varnishes used in historical musical instruments. *Talanta* **2009**, *80*, 286–293.
33. Clementi, C.; Miliani, C.; Verri, G.; Sotiropoulou, S.; Romani, A.; Brunetti, B.G.; Sgamellotti, A. Application of the Kubelka-Munk correction for self-absorption of fluorescence emission in carmine lake paint layers. *Appl. Spectrosc.* **2009**, *63*, 1323–1330.
34. Keune, K.; Boon, J. Analytical imaging studies of cross-sections of paintings affected by lead soap aggregate formation. *Stud. Conserv.* **2007**, *52*, 161–176.
35. Clementi, C.; Doherty, B.; Gentili, P.L.; Miliani, C.; Romani, A.; Brunetti, B.G.; Sgamellotti, A. Vibrational and electronic properties of painting lakes. *Appl. Phys. A* **2008**, *92*, 25–33.
36. Romani, A.; Clementi, C.; Miliani, C.; Favaro, G. Fluorescence spectroscopy: A powerful technique for the noninvasive characterization of artwork. *Acc. Chem. Res.* **2010**, *43*, 837–846.
37. Hötzer, B.; Ivanov, R.; Altmeier, S.; Kappl, R.; Jung, G. Determination of copper(II) ion concentration by lifetime measurements of green fluorescent protein. *J. Fluoresc.* **2011**, *21*, 2143–2153.

38. Preis, W.; Gamsjäger, H. Solid–solute phase equilibria in aqueous solution. XVI. Thermodynamic properties of malachite and azurite—Predominance diagrams for the system $Cu^{2+} – H_2O – CO_2$. *J. Chem. Thermodyn.* **2002**, *34*, 631–650.
39. Ross, J.B.A.; Laws, W.R.; Rousslang, K.W.; Wyssbrod, H.R. Tyrosine FLuorescnece and Phosphorescence in Proteins and Polypeptides. In *Topics in Fluorescence Spectroscopy*; Lakowicz, J.R., Ed.; Springer: London, UK, 2002; Volume 3, pp. 1–64.
40. Comelli, D.; Nevin, A.; Valentini, G.; Osticioli, I.; Castellucci, E.M.; Toniolo, L.; Gulotta, D.; Cubeddu, R. Insights into Masolino's wall paintings in Castiglione Olona: Advanced reflectance and fluorescence imaging analysis. *J. Cult. Herit.* **2011**, *12*, 11–18.
41. Fiedler, I.; Bayard, M. Cadmium Yellows, Oranges and Reds. In *Artists' Pigments: A Handbook of Their History and Characteristics*; Feller, R.L., Ed.; Cambridge University Press and National Gallery of Art: Cambridge, MA, USA, 1986; pp. 65–108.
42. Thoury, M.; Delaney, J.K.; De la Rie, E.R.; Palmer, M.; Morales, K.; Krueger, J. Near-infrared luminescence of cadmium pigments: In situ identification and mapping in paintings. *Appl. Spectrosc.* **2011**, *65*, 939–951.
43. Comelli, D.; Nevin, A.; Brambilla, A.; Osticioli, I.; Valentini, G.; Toniolo, L.; Fratelli, M.; Cubeddu, R. On the discovery of an unusual luminescent pigment in Van Gogh's painting "Les bretonnes et le pardon de pont Aven". *Appl. Phys. A* **2011**, *106*, 25–34.
44. Comelli, D.; Toja, F.; D'Andrea, C.; Toniolo, L.; Valentini, G.; Lazzari, M.; Nevin, A. Advanced non-invasive fluorescence spectroscopy and imaging for mapping photo-oxidative degradation in acrylonitrile-butadiene-styrene: A study of model samples and of an object from the 1960s. *Polym. Degrad. Stab.* **2014**, in press.
45. Miliani, C.; Rosi, F.; Brunetti, B.G.; Sgamellotti, A. *In Situ* Noninvasive Study of Artworks: The MOLAB Multitechnique Approach. *Acc. Chem. Res.* **2010**, *43*, 728–738.

JAAS

PAPER

View Article Online
View Journal

Cite this: DOI: 10.1039/c4ja00385c

An integrated approach based on micro-mapping analytical techniques for the detection of impurities in historical Zn-based white pigments†

V. Capogrosso,*[a] F. Gabrieli,[c] S. Bellei,[ab] L. Cartechini,[c] A. Cesaratto,[ad] N. Trcera,[e] F. Rosi,[c] G. Valentini,[a] D. Comelli[a] and A. Nevin[b]

Received 3rd November 2014
Accepted 10th February 2015

DOI: 10.1039/c4ja00385c

www.rsc.org/jaas

In this work we propose an integrated approach, based on synchrotron analysis with micrometric spatial resolution and sub-ppm sensitivity and μ-Raman mapping, for investigating impurities and heterogeneous inclusions in historical samples of Zn-based white pigments. Analysis was performed at the LUCIA beamline at the SOLEIL synchrotron radiation facility for the simultaneous detection of the elemental distribution in suitably prepared pigment samples using micro-X-ray fluorescence (μ-XRF) mapping and for the investigation of oxidation states and coordination of metals using micro-X-ray near edge absorption (μ-XANES) spectroscopy. The identification of specific molecular signatures and the detection of their spatial distribution throughout samples by μ-Raman measurements supported and complemented X-ray analysis, allowing the identification of Cr- and Fe-based inclusions in historical samples. In ZnO pigments, common impurities are due to the production process and include Fe and, depending on samples, Cd, Cl and Pb. In one of the Zn-containing pigments, identified as Lithopone, μ-XRF mapping revealed the presence of Co, both as highly concentrated micrometric inclusions and as impurities throughout the pigment.

Introduction

At the beginning of the 20th century new classes of pigments based on semiconductors, including the white ZnO, ZnS, TiO_2 and a range of CdS and CdSe yellows and reds, substituted pigments used by artists in earlier periods. In the specific case of the new Zn-based white pigments, despite their improved properties in terms of hiding and handling power with respect to the traditional ones (*i.e.* lead white), early synthetic pigments proved to be chemically unstable. Semiconductor synthesis, following the so called *wet process*, was complex and impurities were inevitably introduced during manufacture, giving rise to chemically complex semiconductors far removed from pigments available today. Indeed, the complexity of historical zinc-based whites has recently received significant attention in work by Osmond[1] in investigations of the formation of Zn carboxylates in paint. The aim of our work is to apply a method based on complementary analytical spectroscopic mapping techniques on the micrometer scale to study historical samples of Zn-based white pigments from different sources (paint tubes, pastels and from an historic pigment powder). The aim of the approach is to document inclusions and impurities in samples, which can be ascribed to production methods.

There are various reports of the analysis of Zn-based whites using both imaging and spectroscopic techniques. For example, *in situ* luminescence imaging spectroscopy of a painting by Van Gogh described a peculiar luminescence emission attributed to copper impurities in a Zn-based white pigment.[2] In another work, spectroscopic investigations on both pure ZnO and paint models have demonstrated that physical and chemical interactions affect the UV and visible emissions, leading to considerably different optical emissions to those in the pure pigment.[3] The investigation of both the vibrational and luminescence properties highlights further interactions between semiconductor Zn-based pigments when mixed with the lipidic binder in paint samples and has revealed the formation of chemisorbed carboxylates from the interaction of the lipidic binder and the ZnO surface.

The use of synchrotron-based techniques to investigate original components and degradation products in artist materials has increased significantly during the last ten years. In particular, micro-X-ray fluorescence (μ-XRF) and micro-X-ray near edge absorption (μ-XANES) techniques are very powerful

[a]Politecnico di Milano, Physics Department, Piazza Leonardo da Vinci 32, 20133 Milan, Italy. E-mail: valentina.capogrosso@polimi.it

[b]Istituto di Fotonica e Nanotecnologie–Consiglio Nazionale delle Ricerche (IFN-CNR), Piazza Leonardo da Vinci 32, I-20133 Milan, Italy

[c]Istituto di Scienze e Tecnologie Molecolari-Consiglio Nazionale delle Ricerche (ISTM-CNR), Via Elce di Sotto 8, 06123 Perugia, Italy

[d]Department of Scientific Research, The Metropolitan Museum of Art, 1000 Fifth Avenue, New York, USA

[e]Synchrotron SOLEIL, Saint-Aubin, BP 48, F 91192, GIF-sur-Yvette, France

† Electronic supplementary information (ESI) available. See DOI: 10.1039/c4ja00385c

analytical methods in probing the spatial distribution and valence of a given chemical element on the microscopic scale.[4–6] The chemical characterization of paints on the nanoscale, using high resolution nanoprobe XRF mapping, has shown impurities from Pb and Fe ions and has provided insights into both the fabrication and the chemical reactivity of ZnO pigments.[7] Photo-luminescent heterogeneities in paint samples containing ZnO have been also investigated at the DISCO beamline at the SOLEIL synchrotron radiation facility through the use of raster-scanning micro-spectroscopy and full-field micro-imaging.[8] By combining synchrotron and macroscopic photoluminescence spectroscopy and imaging, it was shown that three historical powder samples of Zn white pigments were homogeneous on the macroscale yet highly heterogeneous on the micro- and nano-scales.[9]

Our work focuses on the analysis of microscopic heterogeneities in historical samples of Zn-based white pigments from the late 19th and early 20th centuries. After preliminary elemental and molecular characterization of materials using XRF and micro-Raman spectroscopies, we investigated the presence of trace metal ions in prepared samples by μ-XRF mapping using synchrotron radiation. The high-energy synchrotron X-ray beam provides sensitivities three orders of magnitude higher than that of scanning electron microscopy coupled to energy dispersive X-ray spectroscopy (SEM-EDX), leading to sub-ppm sensitivity. In addition, the oxidation and coordination states of some metallic inclusions (including Fe and Cr) have been analysed with μ-XANES spectroscopy. Interpretation of complex data from synchrotron measurements is complemented by the molecular characterization of samples on the μ-scale level with micro-Raman (μ-Raman) spectroscopy.

Historical background on zinc oxide and lithopone synthesis

ZnO was formerly used only as a white pigment and was named *zinc white*. The use of this white pigment spread rapidly and replaced white lead because it had the advantages of being less toxic,[10] of not darkening in the presence of sulphureous gases and of having better hiding power. Today the term *zinc white* denotes ZnO produced by the combustion of metallic Zn according to the *French process* (also called *indirect process*).[11,12] According to this process, Zn is used as starting material and volatilized in a special form of retort; the vapour issuing from the retort is oxidized in the presence of air and collected in long settling chambers. The crystallographic and physical properties of the ZnO can be controlled by adjusting the combustion conditions (flame turbulence and the concentration of oxygen). The typical composition is overall ZnO (99.69–99.99%) with small concentrations of Pb, Cd and Fe.[7,10,12] The cost of production of ZnO from the metal is considerably higher than that of ZnO produced directly from the ore (*American process* described below), but it ensures the absence of impurities, such as Cd, which is considerably more volatile than zinc, and produces a brown oxide which leads to the discoloration of the finished product if it is not removed in the process of the manufacture of the metal.

In the United States the largest proportion of ZnO produced is derived from the ore. In the *American process* (also called the *direct process*) the zinc is reduced by the partial combustion of coal and reoxidized at the entrance to the furnace. The direct process is noted for its simplicity, low cost and excellent thermal efficiency, but it produces a less pure form of ZnO (purity > 98.5%) with possible impurities of Pb, Cd, Fe, S, Cu, and Mn.[7,10,11]

A third industrial production process is known as the *wet process*. ZnO is produced industrially from purified solutions of $ZnSO_4$ or $ZnCl_2$ by precipitating $ZnCO_3$, which is then washed, filtered and finally calcined. This method produces a grade of ZnO with a specific surface area.[11] The product obtained from this method is known as "precipitated zinc white".

Another white Zn-based pigment is based on ZnS, and was first developed and patented in 1850 in France.[13] This white pigment, with the largest sales volume, is *lithopone*, which is a generic name for a white pigment produced through co-precipitation and calcination of ZnS and $BaSO_4$. Despite the cheapness of its manufacturing processes, and its good properties as a pigment (for example, its hiding power is better than that of zinc oxide, and it shows little interaction with other artistic pigments), it has the objectionable property of degrading upon exposure to UV light, darkening and turning grey after exposure to daylight. For this reason, lithopone never earned a good reputation as an artists' pigment. Nevertheless, as Capua argues,[14] lithopone was likely used as a cheap extender for other white pigments such as ZnO. Starting from 1928, small quantities of Co (from 0.02 to 0.5 parts per thousand) were added prior to calcination of the crude lithopone, and this was found to prevent the discoloration of the pigment under sunlight.[15,16]

Experimental details

Material and sample preparation

The four Zn-based samples presented in this work are a selection from a wider collection of historical white pigment samples

Table 1 Summary of the results obtained from preliminary laboratory measurements

Samples	Bulk-XRF	Raman	Grain and agglomerate size
WN1	Zn (Fe, Ba, Ca, Cr, Sn)	ZnO	100–500 nm; 0.7–1 μm
LF1	Zn (Fe, Pb, Ba, Ca)	ZnO + lipidic component	200–500 nm; 0.5–1 μm
LF2	Zn (Fe, Pb, S, Cr)	ZnO, $ZnCO_3$	0.2–1 μm
LF3	Zn, Ba (Sr, S, Pb, Fe, Ca)	Lithopone + lipidic component	0.5–1 μm

and are representative of the different artist materials available at the turn of the 20th C.: pastels, paints and the pigments from which they were made.

One sample is from a paint tube of *Chinese white* Winsor & Newton from the Courtauld Institute of Art in London (WN1). In 1834 Winsor & Newton developed a new method of heating the ZnO to increase its opacity.[17] This new type of Zn white was called Chinese white.

The remaining three samples have been drawn from the well known French manufacturer, Lefranc-Bourgeois, which, at the beginning of the 20th century, was the largest producer of ZnO in Europe.

The first Lefranc sample is a small white pastel fragment from a collection of Lefranc-Bourgeois Raffaelli pastels (LF1). The second sample (LF2) was supplied as a powder by the Colart Lefranc factory, and is a Lefranc watercolour pigment, from a bottle labelled *Blanc de Neige*, Vieille-Montagne Mars, Le Mans (1893). The last sample comes from a Lefranc paint tube belonging to the collection of Grubicy-Benvenuti of the Livorno Foundation (Livorno, Italy) (LF3).

Preliminary XRF and μ-Raman analysis were performed on samples without any specific preparation in order to identify the pigment and binder composition.

Scanning electron microscopy was carried out on samples coated with a thin layer of gold to gain information on grain morphology. For μ-X-ray synchrotron and μ-Raman mapping measurements, small quantities of samples (10 mg on average) were pressed as pellets of 0.5 cm diameter on a boron nitride substrate. During sample preparation we aimed to avoid contamination through proper handling, but we cannot exclude previous contamination prior to sampling of the four pigments.

Experimental apparatus

X-ray fluorescence spectroscopy. Laboratory measurements on samples were carried out using a portable XRF spectrometer (Elio, XGLab srl). The instrument is a fast system with a large area silicon drift detector (SDD) (25 mm^2), and it is particularly efficient due to the X-ray transmission generator that can reach up to 50 kV and to a high solid detection angle geometry. The excitation source works with a Rh anode and the beam is collimated to a spot diameter on the sample surface of about 1.3 mm. XRF measurements have been carried out by fixing the tube voltage at 40 kV and 15 kV exploring a field of analysis from 1 to 30 keV.

Scanning electron microscopy. The scanning electron microscope (SEM) employed was a Philips XL30 instrument equipped with a LaB_6 source and an EDAX/DX4 detector. The acceleration potential voltage was maintained at 15 kV, the magnification was held at 20 000×. For the sake of concision, secondary electron (SE) images of samples are reported in the ESI.†

Raman spectroscopy. μ-Raman measurements were performed using a laboratory JASCO NRS-3100 spectrophotometer equipped with a diode laser at 785 nm, a grating of 800 lines per mm, an optical microscope and a charge coupled device (CCD) cooled to −50 °C with a Peltier cooling system. The areas of

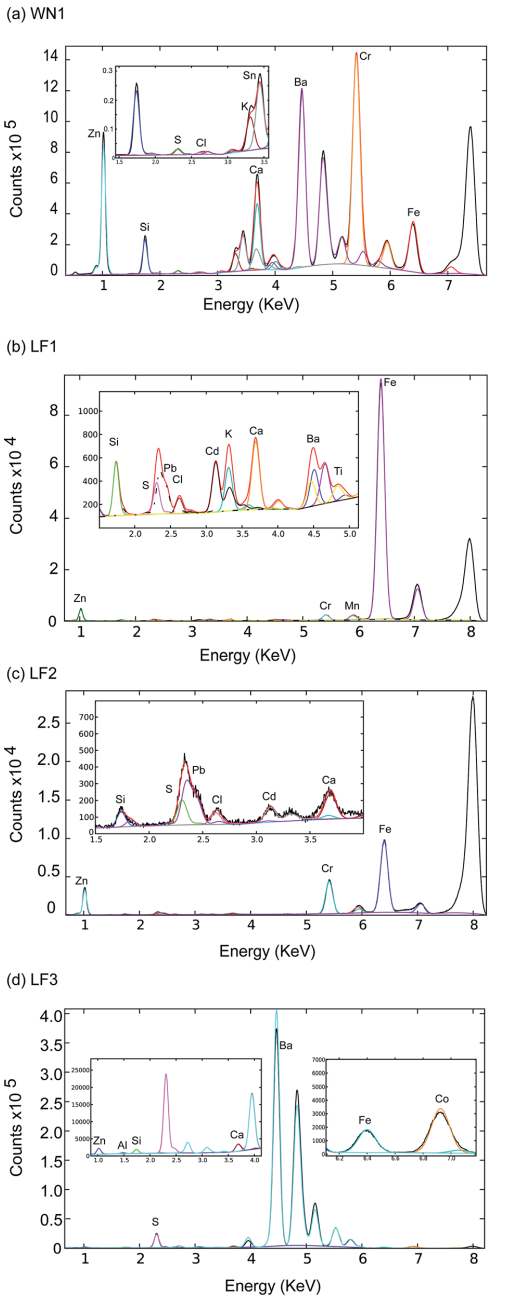

Fig. 1 μ-XRF cumulated spectra, obtained as the sum in all points of a mapped area 100 × 100 μm^2 in size (black line), for the four samples. The result of the fitting of the cumulative spectrum with PyMca software is shown by the red line. In the insets, magnifications of energy regions are shown in order to highlight trace elements.

Table 2 Summary of the results obtained from μ-XRF and μ-Raman techniques

Samples	μ-XRF (impurities)	μ-XRF (inclusions)	μ-Raman
WN1	K	Ba, Cr, Ca, Si, Cl, Fe	$BaCrO_4$
LF1	Pb, Cd, Fe, Al, K, S, Cl, Ca, Si	Fe, Cr, Mn, Ti, Ba	FeO(OH)
LF2	Cl, Fe, Pb, S, Cd, Ca, Si	Cr, Fe	
LF3	Ba, S, Al, Si, Co	Co, Ca, Fe	

interest were focused with the objective 100× and the spectra were recorded in the range 180–1800 cm^{-1} with a spectral resolution of about 2 cm^{-1} and a beam spot size of 3 μm.

For preliminary measurements on samples the exposure time varied from 10 to 20 s and the number of accumulations from 10 to 15; for mapping of pellets exposure times varied from 5–10 s with 10 accumulations. The laser power was changed from 1 mW to a maximum of 18 mW on the sample.

Synchrotron-based X-ray spectroscopy. Simultaneous detection of the atomic distribution and the oxidation state of some

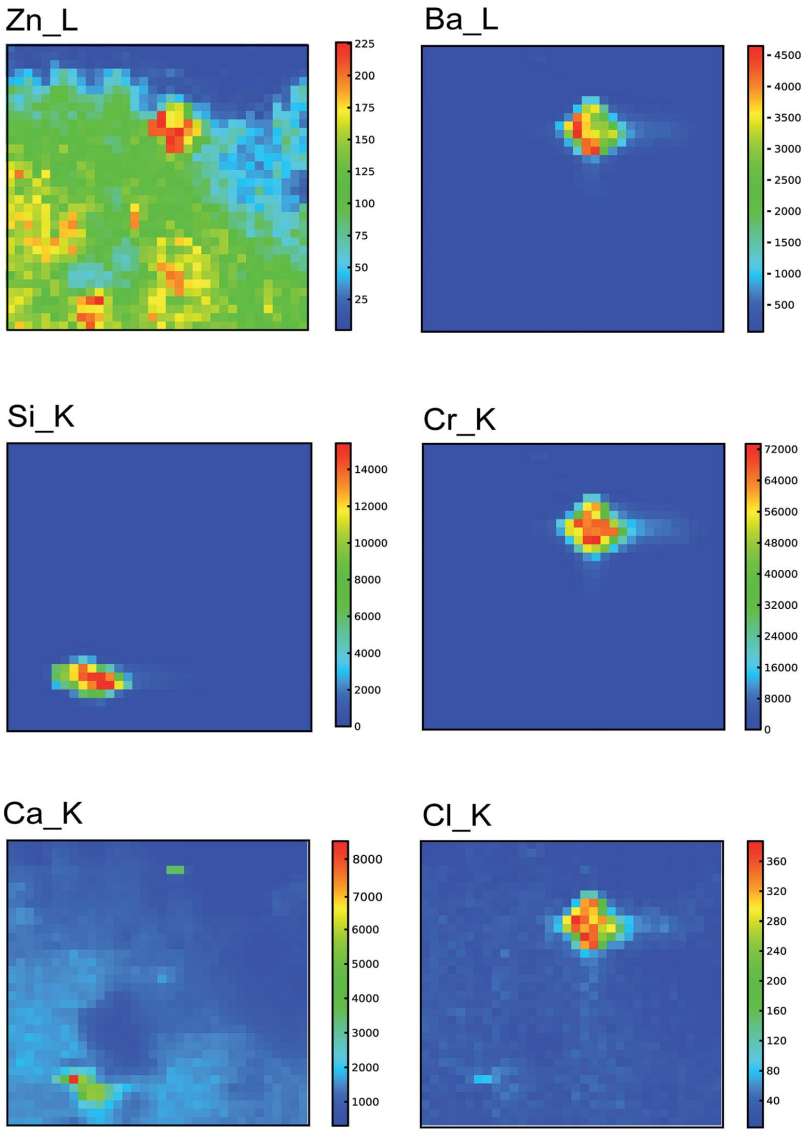

Fig. 2 WN1 sample: μ-XRF maps showing the spatial distribution of Zn, Ba, Si, Cr, Ca and Cl over an area of 100 × 100 μm^2 with a step of 3 μm.

specific heterogeneities was carried out using the set-up at the LUCIA beamline at SOLEIL.[18] The LUCIA beamline is a tender (0.8–8 keV) X-ray microprobe able to detect chemical speciation and to carry out elemental mapping by μ-XANES and μ-XRF spectroscopy respectively. The instrument uses a photon source based on an undulator of the APPLE-II type and a double crystal monochromator for selecting X-ray energy. Analysis was performed in a low vacuum chamber in which samples were placed on a micro-positioning (x, y, z) sample stage. Fluorescence spectra were collected using a 4-element SDD detector. Representative μ-XRF maps of 1000 × 1000 μm^2 with steps of 50 μm were collected in order to identify potential heterogeneities. Afterwards, focused areas containing heterogeneities were chosen and μ-XRF maps of 100 × 100 μm^2 with a step size of 3 μm were collected using a beam spot of 3 × 3 μm^2, and with an excitation energy between 7.4 and 8 keV for the analysis of different elements. At this energy only X-ray fluorescence L-lines of Zn at 1.0 keV are excited and used for detection. μ-XANES spectra were acquired by simultaneously measuring the fluorescence yield (FY) and the total electron yield (TEY), but results are reported only for FY. XANES spectra were collected from inclusions for the Fe K-edge and Cr K-edge.

XRF data were processed using the PyMca software, which has also been used to obtain fluorescence maps.[19] Single element imaging was performed setting Regions Of Interest (ROI) around the characteristic element peaks. In case of overlapping peaks due to the superposition of different lines, it was necessary to fit all spectra separately in order to differentiate contributions and for the reconstruction of an image from the fitted areas using a batch fitting tool. False colour images were generated to represent the presence of different elements in samples, and the scale of each image was chosen to best highlight the heterogeneities detected. Absorption data, after background subtraction, were normalized using Athena.[20]

For the estimation of the size of localized inclusions, the full width at half maximum of a line scan in the μ-XRF or μ-Raman maps was used.

Results

Preliminary laboratory measurements

Results of the preliminary laboratory analysis of samples are summarised in Table 1. All samples contain Zn, as detected with XRF.

In preliminary XRF spectra from WN1, traces of Fe, Ba, Ca, Cr and Sn were detected. Raman spectra identified the pigment as ZnO due to bands at 438 (vs), 383 (w) and 331 (w) cm^{-1}.[16] The sample is characterized by submicron grains in the range of 100–500 nm with a nodular shape typical of fast burning synthesis, which suggests a thermal production process.[13] Few larger conglomerates of about 0.7–1 μm with subhedral hexagonal shape are also visible in SEM images.

XRF measurements on LF1 highlight minor quantities of Fe and traces of Pb, Ba and Ca. Raman spectra confirmed the presence of ZnO,[21] and bands between 1440 and 1060 cm^{-1} indicate the presence of a lipidic component, ascribed to the binder.[22] Indeed, the presence of a lipid binder hinders the observation of the grain morphology in SEM due to the incorporation of the pigments in an amorphous matrix. However, few polyhedral shaped conglomerates with dimensions of 0.5–1 μm are visible. Furthermore, needle-like shapes of about 200–500 nm are present around the large conglomerates.

LF2 has traces of Fe, Pb, S and Cr. From μ-Raman analysis the sample has been identified as a mixture of ZnO and $ZnCO_3$. The pigment grains have variable dimensions, in the range of 0.2–1 μm, and morphology varying from large polycrystalline angular conglomerates to smaller prismatic or acicular crystallites. This morphology can be explained by a non-controlled slow crystallization process, such as the *wet process*. This production method is in agreement with the presence of carbonates, as described in the historical background section.[11]

In contrast to the three ZnO samples (WN1, LF1 and LF2), XRF on LF3 highlighted the presence of Ba in addition to Zn, with weaker signals of Sr and S along with traces of Pb, Fe and Ca. μ-

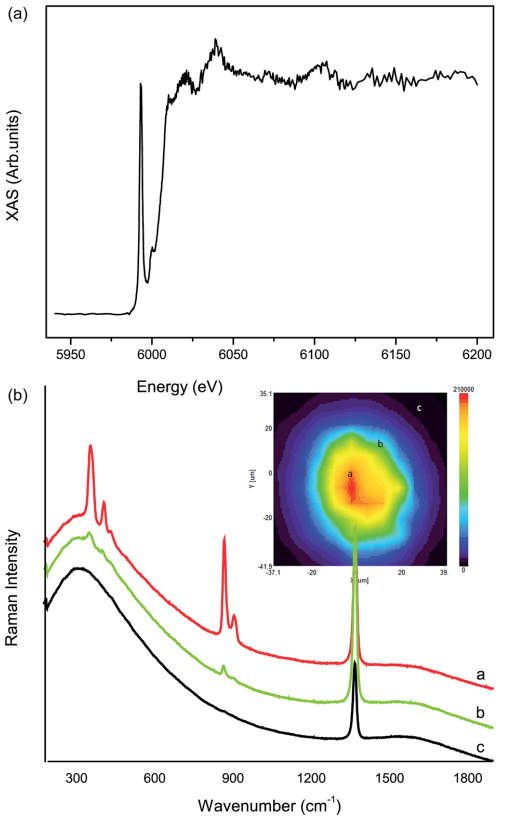

Fig. 3 WN1 sample: (a) μ-XANES spectrum at Cr K-edge recorded from the inclusion highlighted in the Cr map shown in Fig. 2; (b) μ-Raman map, resulting from the integration of the chromate band at 862 cm^{-1} over an area of 77 × 77 μm^2, and μ-Raman spectrum registered at the core of the inclusion (a), at the border (b) and outside the inclusion (c).

Raman spectra of the powdered sample showed peaks of $BaSO_4$ and a weak band at 348 cm^{-1}, assigned to ZnS.[21] The spectrum is consistent with the reference spectra of *lithopone*. The observation of additional bands at 1440 cm^{-1} and 1297 cm^{-1} suggests the presence of a lipidic component.[22] Few polyhedral shaped conglomerates with dimensions of 0.5–1 μm are visible in SEM images due to the presence of the lipidic binder.

From bulk XRF measurements, a common trace element present in all four samples is Fe, which could be ascribed to the use of the raw material sphalerite (Zn, Fe)S in synthesis. This cubic resinous sulphide mineral is the most common of the zinc minerals, and it is nearly always associated with Al, resulting from acidic weathering of rock and sulphide minerals, and may also include Pb, resulting from mine drainage activity.[23]

μ-XRF and μ-Raman mapping

As it will be shown hereafter for the considered samples, the μ-XRF and μ-Raman combined approach allows us to distinguish amongst elements homogeneously distributed throughout the pigment matrix and elements spatially localized in a confined area. In the text, the former and the latter will be referred to with the notation of *impurities* and *inclusions*, respectively. Moreover, with the combination of the two μ-mapping techniques we can further obtain insights into the size of localized inclusions. This information can provide understanding of the origin of trace metals in samples.

WN1

In Fig. 1a the cumulative spectrum from μ-XRF mapping using synchrotron radiation, fitted using PyMca, is reported. μ-XRF measurements highlight the presence of Ba and Cr, combined with traces of Ca, Fe and Si. Weak emissions are assigned to K, S, and Cl. μ-XRF maps of compositional distribution provided evidence of the spatial correlation of different elements, allowing the differentiation between homogeneously distributed *impurities* and localized *inclusions*, as summarized in Table 2 for all samples.

μ-XRF maps (Fig. 2) revealed the spatial correlation between Si and Ca in an asymmetric agglomerate inclusion estimated as 21 × 12 μm^2 in size. No molecular identification has been achieved for these inclusions; the spatial correlation may be an indication of possible calcium containing silicates, but other compounds cannot be excluded.

An excellent spatial correlation between Ba, Cr and Cl distributions is seen in an agglomerate 20 μm in diameter. In order to clarify the oxidation state of the Cr in the inclusion,

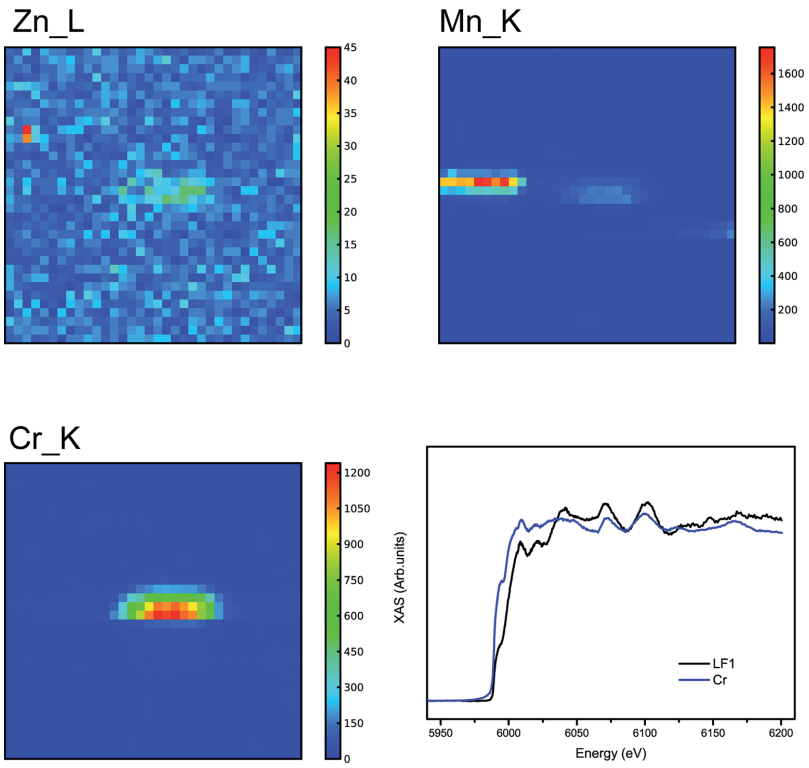

Fig. 4 LF1 sample: (a) μ-XRF maps showing the spatial distribution of Zn, Mn and Cr over an area of 100 × 100 μm^2 with a step of 3 μm. On the bottom right, μ-XANES spectra recorded from the Cr inclusion (black) and a reference sample of metallic Cr (blue).

μ-XANES measurements have been performed on the same area. The measured Cr K-edge μ-XANES spectrum (Fig. 3a) shows a well-defined pre-edge peak at 5.993 keV, typical of Cr(VI) compounds with a tetrahedral coordination geometry. This peak corresponds to a bound state 1s to 3d dipole-forbidden transition, and it is related to the non-centrosymmetric nature of the tetrahedral structure that favours a strong hybridization of the Cr 3d and O 2p orbitals.[24] The spectrum is comparable with that of $BaCrO_4$ reported by Monico.[6]

The presence of $BaCrO_4$ in sample WN1 is confirmed by μ-Raman spectra acquired from yellow crystals (of about 45 × 45 μm^2) visible on the pellet investigated at the synchrotron. An example image of a $BaCrO_4$ crystal from μ-Raman mapping is reported in Fig. 3b. The map is 77 × 77 μm^2 and was obtained by acquiring each spectrum with a step of 7 μm. The false-colour image was obtained by integration of the band relative to the symmetric stretching mode of the CrO_4^{2-} group at 862 cm^{-1}.[21]

In Fig. 3b, the Raman spectrum recorded at the center of the inclusion (a) clearly shows bands distinctive to $BaCrO_4$, including the symmetric stretching modes at 862 and 900 cm^{-1} as well as the bending at 403 cm^{-1}. As expected these diagnostic bands diminish in intensity when moving towards the boundaries of the inclusion (spectra b and c in Fig. 3b) where the boron nitride signal from the substrate is mainly present at 1368 cm^{-1}.

$BaCrO_4$ can be synthesized by co-precipitating barium hydroxide with potassium chromate ($Ba(OH)_2 + K_2CrO_4 \rightarrow BaCrO_4 + 2KOH$) or, alternatively, by the interaction of barium chloride ($BaCl_2$) with sodium chromate (Na_2CrO_4).[25,26] This synthesis method would explain the presence of Cl in the same inclusion. $BaCrO_4$ is usually associated with *lemon yellow*, and in WN1 this is possibly an unintentional contamination introduced during the mixing of the pigments in the paint.

LF1

μ-XRF measurements on LF1 are shown in Fig. 1b. LF1 is characterised by the presence of Fe, and to a lesser extent Cr and Mn, with traces of Al, Si, S, Pb, Ba, Cl, Cd, K and Ti.

Pb and Cd, distributed homogeneously throughout the ZnO matrix, are ascribed to residues of the production process. The presence of Cd may exclude the French process in the synthesis of the sample. Ti, which appears as localized inclusions, was probably due to TiO_2 added to the ZnO matrix as a whitening agent.

Zn, Mn and Cr μ-XRF maps obtained on an area of 100 × 100 μm^2 are reported in Fig. 4, with Mn and Cr appearing as inclusions which are not spatially correlated with one another.

Regarding the presence of Mn inclusions (30 × 3 μm^2 in size), it has been reported that Mn oxides (in particular pyrolusite) and dehydrated Mn salts were added in small proportions to paint tube formulations in order to improve the siccative properties of lipid binders.[27] A similar explanation may account for the presence of Al; in fact aluminum stearate was a common additive to paints as an emulsifier.[1]

To better understand the presence of the Cr inclusion (30 × 10 μm^2 in size), μ-XANES measurements at the Cr K-edge were collected. The spectrum reported in Fig. 4d is comparable with that of a metallic Cr reference. The presence of metallic Cr could be explained by *fly ash* (mineral residue resulting from the combustion of coal in electric generating plants and in reducing environments) during the production process, so, in this sample the wet process is excluded and we hypothesise that this sample was produced by the *American process*.

Significant concentrations of Fe were mapped on different areas of the sample, with the element found both as a localized heterogeneity and homogeneously distributed throughout the sample matrix. In the latter case, its presence can be explained as a residue of the production process, whereas in the former it is likely due to sample contamination. As an example, in an area with a concentrated Fe inclusion (9 × 12 μm^2 in size), the μ-XANES spectrum at the Fe K-edge has been measured (Fig. 5a). The spectrum is comparable with an iron oxide reference.[28] μ-Raman measurements identified this Fe-based

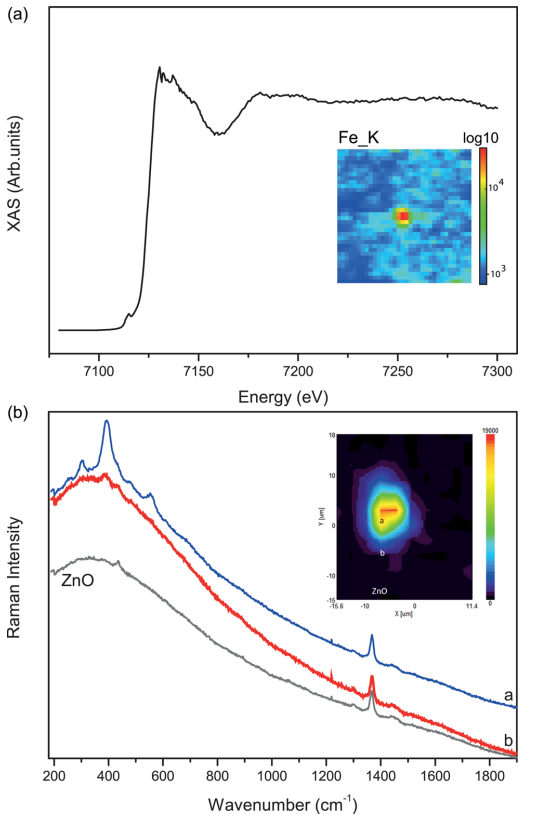

Fig. 5 LF1 sample: (a) μ-XANES spectrum at the Fe K-edge acquired from an area with a concentrated Fe inclusion seen in the μ-XRF map shown in the inset on a logarithmic scale; (b) μ-Raman map acquired on the same Fe inclusion, resulting from the integration of the band at 389 cm^{-1} over an area of 36 × 30 μm^2, and micro-Raman spectrum registered at the core (a) and at the border of the inclusion (b) and on a ZnO reference sample.

compound as goethite (α-FeO(OH)) by the presence of three bands at 300 (m), 389 (s) and 550 (m) cm^{-1}, related to the vibrational modes of the Fe–O and Fe–OH bonds.[29]

μ-Raman mapping has been carried out on the same area analysed by μ-XANES, scanning a surface of 36 × 30 μm^2 with a 3 μm step size. The chemical image shown in Fig. 5b has been obtained by integration of the most intense band at 389 cm^{-1}, and suggests the dimensions of the α-FeO(OH) inclusion to be approximately 10 × 10 μm^2, in good agreement with μ-XRF data.

LF2

In Fig. 1c the μ-XRF spectrum of LF2 is dominated by the presence of Fe and Cr with traces of S and Pb. The micrometric maps also highlight the presence of Si, Ca, Cd and Cl.

This sample is primarily of interest because it is representative of the *wet process*, as reported above. The identification of traces of Cl and its homogeneous distribution throughout the sample matrix, as shown in the μ-XRF Cl map (Fig. 6), suggest the use of a $ZnCl_2$ solution as a precursor in the *wet process*.

Homogeneously distributed impurities of Fe, Pb, and Cd are typical residues of this production process.[10] Fe was detected both homogeneously distributed throughout the sample matrix and as localized heterogeneities. Cr is found as an inclusion (20 μm in diameter), and it is reasonable that it has been unintentionally added to the pigment. In contrast to WN1, no Ba was detected in LF2, and hence the metal could be associated with a different Cr-based pigment.

Ca and Si are homogeneously distributed in the sample and were probably added as extenders during the production process.

LF3

The cumulative μ-XRF spectrum is reported in Fig. 1d, and it is dominated by the presence of Ba and S.

The investigation of the sample with a micrometric resolution allowed the mapping of the presence of particles containing Al, Si, Ca, Fe and traces of Co. The small amount of Si homogeneously distributed in the matrix is likely due to the presence of an extender. Similarly to the other lipid-based sample (LF1), the presence of Al in LF3 is likely due to the presence of an aluminum stearate in the paint tube formulation.

μ-XRF maps reported in Fig. 7 show a strong correlation between the distributions of Ba, S and Zn. This confirms the results from μ-Raman measurements that identified the pigment as lithopone.

Finally, the Co map (shown in Fig. 7 with a logarithmic scale) highlights the presence of both highly concentrated cobalt

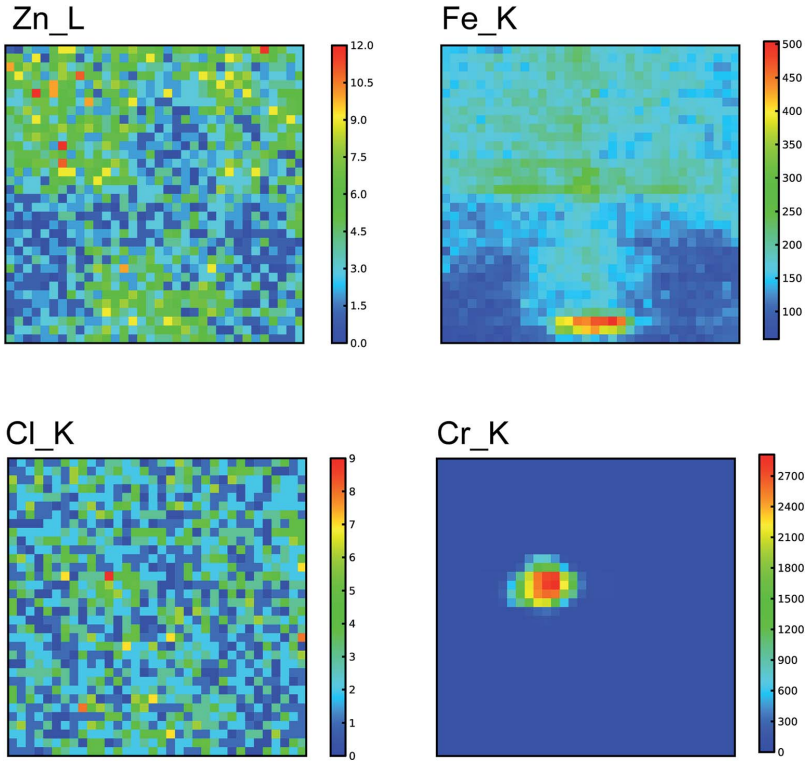

Fig. 6 LF2 sample: μ-XRF maps showing the spatial distribution of Zn, Fe, Cl and Cr over an area of 100 × 100 μm^2 with a step of 3 μm.

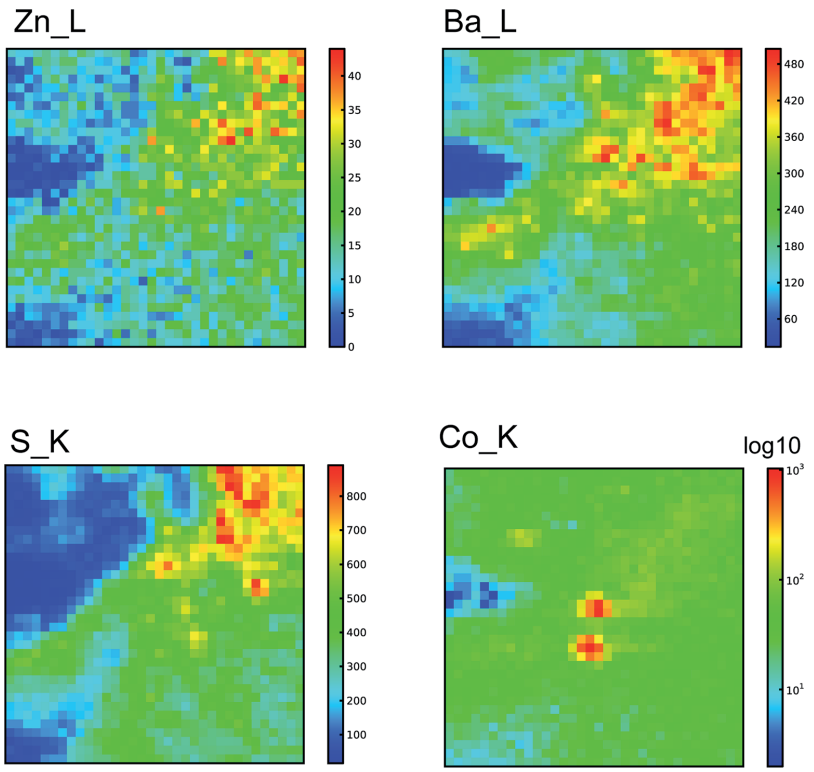

Fig. 7 LF3 sample: μ-XRF maps showing the spatial distribution of Zn, Ba, S and Co (in logarithmic scale only for Co) over an area of 100 × 100 μm^2 with a step of 3 μm.

micrometric *inclusions* together with the homogeneous distribution of trace Co correlated with Zn and Ba, suggesting that the paint tube was produced after 1928, as explained in the introduction.[15,16] This information suggests that the paint tube was not part of the collection of Vittore Grubicy de Dragon (1851–1920) but rather of Benvenuto Benvenuti (1881–1959).

Discussion

In the previous section the results obtained from the analysis of historical Zn-based white samples of different origin were reported.

The results demonstrate how bulk analysis with limited sensitivity can yield diagnostic information for the identification of ZnS or ZnO, as well as data regarding the presence of trace elements, but careful sample preparation and study using micro-analytical techniques is necessary for a better understanding of *inclusions* and *impurities*. While morphological information obtained by SEM is useful for the assessment of pigments in powder, the presence of binder (as in the case of paint tube) hinders the observation of grain dimensions or morphology, thus motivating the use of complementary molecular analysis.

In the case of the identification of $BaCrO_4$ and goethite in WN1 and LF1, respectively, bulk analysis would have led to misleading conclusions, because of the impossibility to distinguish the two contaminants from impurities of the production process. Another example of the necessity to combine bulk and micrometric analysis is highlighted in the detection of metallic Cr, which is present as an inclusion in LF1 and is indirect evidence of the thermal production process.

The real novelty presented in this work is the possibility, offered by a micrometric resolution, to distinguish between *impurities* and *inclusions*. This distinction is fundamental for ascribing a particular element to a residue of the manufacturing process, as in the case of an impurity, or to a contamination, as in the case of a localized inclusion. In the case of sample LF2, Raman and SEM measurements suggested the wet production process, a hypothesis supported by the presence of homogeneously distributed impurities of Fe, Pb and Cd.

It is, however, more tricky to establish if contamination in samples was accidental or not. This is shown in sample WN1 which contains crystals of $BaCrO_4$ which cannot be related to

the production of ZnO. On the other hand, the identification of traces of Co in LF3 as an intentional impurity rather than isolated inclusions allows the dating of the lithopone sample to a specific historical period. Establishing production processes is complex, and only in some cases can morphology (as evidenced by SEM) and impurities give convincing proof of a particular production process. Indeed in the four samples studied, while the wet process is clear for LF2 from the particle size, the presence of carbonates and Cl, other production processes are more elusive. In LF1, traces of Cd and metallic Cr suggest the *American process*, while in the case of WN1 it is only possible from elemental data to exclude the *wet process*. More in depth investigations of a statistical number of samples of known production type would be required to correlate impurities with a specific production method or geographical origin.

Conclusions

Our work proposes a multi-analytical methodological approach for the chemical characterization of modern Zn-based pigments with a micrometric resolution. This is achieved by combining μ-XRF, μ-XANES and μ-Raman techniques, and could become a tool for investigating not only a particular class of semiconductor pigments, as in this work, but different modern pigments.

The identification and distinction between homogeneously distributed *impurities* and localized *inclusions* in samples allowed for discrimination between elements that are residues of the pigment production processes and the elements that were introduced after the synthesis process, mainly as a result of contamination.

The mapping of impurities and inclusions within pigment particles, with the support of SEM measurements, provides information which, in some cases, allows for discrimination between different manufacturing routes. Data obtained in this work will inform the definition of elemental markers for future *in situ* analysis of paint samples, with implications for the analysis of Zn-based whites from early 20th century paintings. Future research should focus on the study of modifications in the optical properties of the pigments due to transition metal impurities and the characterization of Co-based salts in lithopone pigments.

Acknowledgements

Access to the SOLEIL Facility was funded through the CALIPSO European program.[30] Funding for research was provided through the FUTURAHMA project (http://www.futurahma.it), *From Futurism to Classicism (1910–1922). Research, Art History and Materials Analysis*. The research project FUTURAHMA (2013–2016) is financed by the Italian Ministry of Education, University and Research (MIUR) within the Future in Research 2012 program. We gratefully acknowledge the Fondazione Livorno for the sample from the Grubicy Benvenuti Collection, Prof. Aviva Burnstock from the Courtauld Institute of Art, and COLART for samples from the Lefranc Collection. Prof. Lucia Toniolo of the Politecnico of Milan is thanked for providing other samples.

Notes and references

1 G. Osmond, J. Boon, L. Puskar and J. Drennan, *Appl. Spectrosc.*, 2012, **66**, 1136–1144.
2 D. Comelli, A. Nevin, A. Brambilla, I. Osticioli, G. Valentini, L. Toniolo, M. Fratelli and R. Cubeddu, *Appl. Phys. A*, 2011, **106**(1), 25–34.
3 C. Clementi, F. Rosi, A. Romani, R. Vivani, B. G. Brunetti and C. Miliani, *Appl. Spectrosc.*, 2012, **66**(10), 1233–1241.
4 L. Bertrand, L. Robinet, M. Thoury, K. Janssens, S. X. Cohen and S. Schöder, *Appl. Phys. A*, 2011, **106**(2), 377–396.
5 M. Cotte, J. Susini, J. Dik and K. Janssens, *Acc. Chem. Res.*, 2010, **43**(6), 705–714.
6 L. Monico, G. Van der Snickt, K. Janssens, W. De Nolf, C. Miliani, J. Verbeeck, H. Tian, H. Tan, J. Dik, M. Radepont and M. Cotte, *Anal. Chem.*, 2011, **83**(4), 1214–1223.
7 F. Casadio and V. Rose, *Appl. Phys. A*, 2013, **111**(1), 1–8.
8 M. Thoury, J.-P. Echard, M. Réfrégiers, B. Berrie, A. Nevin, F. Jamme and L. Bertrand, *Anal. Chem.*, 2011, **83**(5), 1737–1745.
9 L. Bertrand, M. Réfrégiers, B. Berrie, J.-P. Echard and M. Thoury, *Analyst*, 2013, **138**(16), 4463–4469.
10 A. Moezzi, A. M. McDonagh and M. B. Cortie, *Chem. Eng. J.*, 2012, **185–186**, 1–22.
11 G. Buxbaum and G. Pfaff, *Industrial Inorganic Pigments*, Wiley-vch, Germany, 2005.
12 C. D. Holley, *The lead and zinc pigments*, J. Wiley and Sons, California, USA, 1909.
13 N. Eastaugh, V. Walsh, T. Chaplin and R. Siddall, *Pigment compendium: a dictionary and optical microscopy of historical pigments*, Butterworth-Heinemann, Oxford, UK, 2004.
14 R. Capua, *J. Am. Inst. Conserv.*, 2014, **53**(2), 75–88.
15 G. Jantsch and P. Wolski, *US pat.* 1693902, United States Patent Office, 1928.
16 M. Bacci, M. Picollo, G. Trumpy, M. Tsukada and D. Kunzelman, *J. Am. Inst. Conserv.*, 2007, **46**(1), 27–37.
17 http://www.winsornewton.com/na/discover/articles-and-inspiration/spotlight-on-chinese-white, accessed 02/10/2014.
18 A.-M. Flank, G. Cauchon, P. Lagarde, S. Bac, M. Janousch, R. Wetter, J.-M. Dubuisson, M. Idir, F. Langlois, T. Moreno and D. Vantelon, *Nucl. Instrum. Methods Phys. Res., Sect. B*, 2006, **246**(1), 269–274.
19 V. a. Solé, E. Papillon, M. Cotte, P. Walter and J. Susini, *Spectrochim. Acta, Part B*, 2007, **62**(1), 63–68.
20 B. Ravel and M. Newville, *J. Synchrotron Radiat.*, 2005, **12**, 537–541.
21 R. J. H. Clark, *Spectrochim. Acta, Part A*, 2001, **57**(7), 1491–1521.
22 P. Vandenabeele, B. Wehling, L. Moens, H. Edwards, M. De Reu and G. Van Hooydonk, *Anal. Chim. Acta*, 2000, **407**, 261–274.

23 D. M. McKnight, B. A. Kimball and R. L. Runkel, *Hydrol. Processes*, 2001, **15**(10), 1979–1992.
24 A. Pantelouris, H. Modrow, M. Pantelouris, J. Hormes and D. Reinen, *Chem. Phys.*, 2004, **300**, 13–22.
25 H. Dourif, *US pat.* 1587704, United States Patent Office, 1926.
26 N. Heaton, *Outlines of Paint Technology*, Charles Griffin & Co., London, 3rd edn, 1947.
27 P. Fleury, *The preparation and uses of white zinc paints*, Scott, Greenwood & Son, London, 1912.
28 T. E. Westre, P. Kennepohl, J. G. Dewitt, B. Hedman, K. O. Hodgson and E. I. Solomon, *J. Am. Chem. Soc.*, 1997, **119**, 6297–6314.
29 D. L. A. de Faria, S. Venâncio Silva and M. T. de Oliveira, *J. Raman Spectrosc.*, 1997, **28**, 873–878.
30 http://www.calipso.wayforlight.eu/, accessed 02/10/2014.

analytical chemistry

Article

pubs.acs.org/ac

Multianalytical Study of Historical Luminescent Lithopone for the Detection of Impurities and Trace Metal Ions

Sara Bellei,*[,†,‡] Austin Nevin,[†] Anna Cesaratto,[‡,∥] Valentina Capogrosso,[‡] Hervé Vezin,[§] Caroline Tokarski,[⊥] Gianluca Valentini,[‡] and Daniela Comelli[‡]

[†]Istituto di Fotonica e Nanotecnologie - Consiglio Nazionale delle Ricerche (CNR-IFN), Piazza Leonardo da Vinci 32, Milano, 20133 Italy

[‡]Dipartimento di Fisica, Politecnico di Milano, Piazza Leonardo da Vinci 32, Milano, 20133 Italy

[§]Laboratoire de Spectrochimie Infrarouge et Raman (LASIR), UMR CNRS 8516, Université de Lille 1 Sciences et Technologies, 59655 Villeneuve d'Ascq Cedex, France

[⊥]Miniaturisation pour la Synthèse, l'Analyse & la Protéomique (MSAP), USR CNRS 3290, Université de Lille 1 Sciences et Technologies, 59655 Villeneuve d'Ascq Cedex, France

Supporting Information

ABSTRACT: We have explored the performance of an integrated multianalytical approach to the analysis of a series of microsamples of historical lithopone (a coprecipitate of ZnS + $BaSO_4$) produced at the beginning of the 20th century, based on the combination of spectrally- and lifetime-resolved photoluminescence (PL) microscopy imaging and electron paramagnetic resonance (EPR) spectroscopy. Multispectral imaging of the PL emission from microsamples revealed the presence of different luminescence centers emitting in the visible spectrum, which we have hypothesized as trace Cu and Mn impurities unintentionally introduced into the ZnS crystal lattice during synthesis, which act as deep traps for electrons. Time-resolved PL imaging analyses highlighted the microsecond decay-kinetic behavior of the emission, confirming the trap state nature of the luminescence centers. EPR confirmed the presence of Cu and Mn, further providing information on the microenvironment of defects in the ZnS crystalline lattice related to specific paramagnetic ions. The multianalytical approach provides important insights into the historical synthesis of lithophone and will be useful for the rapid screening and mapping of impurities in complex semiconductor pigments and other artists' materials.

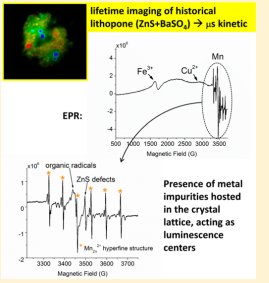

Lithopone is a modern inorganic white pigment composed of a coprecipitate of zinc sulfide (ZnS) and barium sulfate ($BaSO_4$). It was manufactured on a commercial scale starting in 1874 and sold under different names (Griffith white, Charlton White, Orr's Zinc White). It found its application first in the cheaper grades of polish varnishes, floor paints, and paints for interiors as a substitute of lead white. Despite the cheapness of its manufacturing processes and good property as pigment, lithopone had the tendency to darken when exposed to sunlight.[1] To prevent discoloration, starting in 1928, a small amount of cobalt, varying from 0.02% to 0.5% of the zinc content, was added prior to the calcination process.[2] Nevertheless, due to the photodarkening effect, lithopone earned a bad reputation that made its usage as an artists' pigment difficult to establish.[3] Lithopone was likely used as a cheap extender for other white pigments like ZnO or sold under ambiguous names and then involuntarily used by artists. Lithopone as a pigment can be still purchased today.

The identification of lithopone is not straightforward with elemental analysis such as X-ray fluorescence (XRF), since data does not permit the distinction between lithopone from mixtures of barium sulfate and zinc sulfide or zinc oxide present as unprecipitated compounds. A noninvasive protocol for identification of the pigment has been proposed with the aid of different molecular spectroscopy techniques, such as fiber-optic reflectance spectroscopy (FORS) in the UV-vis-NIR and micro-Raman analyses.[4] Few studies have dealt with the photoluminescence (PL) properties of lithopone: in 2012, Comelli et al.[5] published results of PL attributed to Zn-based whites in a painting by *Vincent Van Gogh "Les bretonnes et le pardon de Pont Aven"* (Milan, Galleria di Arte Moderna). In 2014, Capua[3] attributed a green phosphorescent emission on some watercolors by American artist *John La Farge* to lithopone.

The PL properties of lithopone depend essentially on those of ZnS. ZnS is a II–VI compound semiconductor with two main crystalline forms: the more stable cubic form (zinc blende or sphalerite) and the hexagonal form (wurtzite), which is formed after treatment at high temperature.[6] The semiconductor has a direct band gap of 3.54 eV (cubic) or 3.91 eV (hexagonal) at room temperature. After annealing, pure ZnS shows an emission band in the blue region, with an emission

Received: February 10, 2015
Accepted: May 15, 2015
Published: May 28, 2015

DOI: 10.1021/acs.analchem.5b00560
Anal. Chem. 2015, 87, 6049−6056

Table 1. List of Samples Analyzed as Part of This Study with Historical Information Regarding Their Manufacture

sample name	pigment name	manufacturer	geographical location	manufacturing period
commercial_ZnS	--	Kremer Pigmente GmbH&Co	Germany	commercially available
commercial_lithopone	--	Kremer Pigmente GmbH&Co	Germany	commercially available
S1	unknown	New Jersey Zinc Company (now HorseHead Corporation)	New Jersey, USA	1848−1966
S2	unknown	Acme	unknown	>1922
S3	unknown	DuPont	Delaware, USA	>1922
S4	unknown	The Chemical	unknown	unknown
S5	Ponolith	Krebs Pigment and Chemical Company (now DuPont)	Delaware, USA	1902−1929
S6	Ponolith	Krebs Pigment and Chemical Company (now DuPont)	Delaware, USA	1902−1929

maximum ranging from 416 to 478 nm assigned to vacancies or interstitial defects in ZnS.[7,8] The addition of a few ppm of a suitable activator into the ZnS matrix creates an efficient light-emitting material, which has been exploited both in bulk material and in nanocrystalline form. In doped ZnS, recombination occurs via shallow trap states or via deep trap states of different kinds which are created by the interaction of the doping element with the semiconductor matrix. Most common activators for phosphorescent ZnS are Mn,[9−11] Cu,[10−13] and Ag;[11,14,15] other impurities, including Al[16,17] and Cl ions,[13,17] have also been investigated. Thus, it has been hypothesized that historical lithopone pigments, which were produced using nonperfect synthesis processes, can be associated with metal impurities which can act as luminescent centers.

In this work, we aim to provide new insights into the optical properties of historical lithopone samples through the combination of spectrally- and time-resolved PL imaging, for the quick identification and mapping of luminescent impurities, and electron paramagnetic resonance (EPR) analysis for the assessment of the presence of specific impurities and defects, which are responsible for the luminous properties of the pigment.

MATERIALS AND METHODS

Six historical samples (S1−6) of lithopone from the beginning of the 20th Century, synthesized in the United States of America, have been investigated. Samples come from the Chamot-Cornell collection and were provided by Joseph Barabe, McCrone Pigments. In Table 1, a list of samples with the indication of the manufacturers is provided. One commercial sample of lithopone and one of ZnS (Kremer Pigmente GmbH&Co., Germany) were studied for comparison.

Powder from each sample was divided into three portions. The first part was used for bulk analysis; the second portion was adequately dispersed between two layers of UV-transparent silica glass of approximately 40 μm thickness to perform PL microscopy, and the third part was used for EPR analysis. For EPR analysis, each sample powder was placed in a thin-walled quartz sample tube with inner dimensions of 1 mm.

System Setup. *X-ray Fluorescence (XRF).* XRF analysis was performed with a portable EDXRF spectrometer (Elio Spectrometer, XGlab srl, Milan, Italy).[18] The instrument can detect elements from Na to U, with a field of analysis between 1 and 40 keV.

Raman Analysis. Raman analysis was performed using a portable Raman spectrometer,[19] based on a 785 nm semiconductor laser (Lion, Sacher Lasertechnik GmbH, Germany) with adjustable power from 0 to 280 mW. A spectrometer (SpectraPro2150, Princeton Instruments, USA) equipped with a 1200 grooves/mm grating and coupled to a front illuminated cooled CCD (PIXIS 100, Princeton Instruments, USA) is employed for spectra registration, covering a spectral range of 150−1200 cm^{-1} at a resolution of approximately 15 cm^{-1}. Through fiber optics, the laser and the spectrometer are connected to a properly designed microprobe, working in backscattering geometry and focusing laser light in a 100 μm (diameter) spot. Density power on samples has always been kept below 500 W/cm^2.

Scanning Electron Microscopy (SEM). Morphologies and the microstructure of samples were imaged with a scanning electron microscope (SEM, Zeiss EVO 50 EP). Powders were deposited on a carbon tape suitable for SEM analyses and sputter-coated with a 10 nm layer of gold.

Multispectral PL Microscopy. Multispectral PL microscopy was performed with an optical microscope (Leica DM RE) equipped for epi-fluorescence measurements. Emission was excited by the 365 nm line of a mercury lamp with the aid of a microscope cube mounting proper excitation and dichroic filters (ET365/10 and ZT390dclp, Chroma Technology Corporation.). Seven band-pass transmission filters from 400 to 700 nm with a spectral band of 40 nm (FKB-VIS-40, Thorlabs Inc.) were used to measure a selected part of the emission spectrum. The image detector employed was a low-noise monochrome CCD camera (Retiga 2000R, QImaging, Canada). Images were typically acquired using 20× or 50× objectives, with a resulting sampling pitch of 1.8 and 0.7 μm, respectively, due to the camera pixel size. A sequence of seven spectral images between 400 and 700 nm in steps was acquired by changing the filter manually. Assuming the spectral transmission of each filter as a Dirac delta function peaked on the central wavelength and following proper correction for the detector efficiency, emission spectra at all points of the field of view were reconstructed. The color image of the emission, calculated on the basis of the RGB color space, was employed as a rapid indication of the emission in the analyzed area.

Time-Resolved PL Microscopy. Time-resolved measurements have been performed on the same microscope but exciting emission through a Q-switching frequency-tripled diode-pumped Nd:YAG laser (FTSS 355-50 Crylas GmbH, Berlin, Germany, λ = 355 nm, Pulse energy = 70 μJ, pulse duration = 1.0 ns). The laser beam is coupled to a 600 μm silica optical fiber and projected onto the object plan through a proper optical system composed of three plano-convex lenses (focal length = 10, 100, and 50 mm) in order to uniformly illuminate the field of view. The dynamics of the emission is detected by a gated intensified CCD camera (C9546-03, Hamamatsu Photonics, 100 ns gate width, temporal jitter ~0.1 ns) based on a GaAs photocathode with spectral sensitivity from 380 to 850 nm. Spatial resolution essentially depends on that of the intensifier (57 lp/mm), resulting in a value of 1.5

DOI: 10.1021/acs.analchem.5b00560
Anal. Chem. 2015, 87, 6049−6056

μm when employing the 50× objective. For data analysis, luminescence lifetime maps have been produced by modeling data with a monoexponential decay, providing a qualitative estimation of the heterogeneity of the decay kinetic of the emission from samples. Following this, in each lifetime map areas with similar kinetic emissions have been clustered together by employing image segmentation on the basis of k-means clustering. The mean luminescence decay extracted in each cluster has then been fitted on the basis of a multiexponential decay model (with a maximum of three components) as described elsewhere.[5] Multispectral and time-resolved PL measurement have been performed on the same area in order to correlate results.

Electron Paramagnetic Resonance (EPR) Spectroscopy. EPR spectra of all the samples were recorded at room temperature using a Bruker E500 spectrometer operating at X-band frequency of 9 GHz, having a 2 G of amplitude modulation and 5 mW for the microwave power.

RESULTS

Preliminary bulk measurements on historical samples with Raman and XRF spectroscopy confirmed that the pigments contained elemental and molecular signals attributed to lithopone: representative Raman and XRF spectra of sample S2 are shown in Figure 1, with typical Raman shifts of ZnS (348 cm^{-1}) and $BaSO_4$ (455 and 987 cm^{-1}) and the presence of Zn, S, and Ba as the main elements. XRF did not detect other trace elements, suggesting that, if metallic impurities are present, their concentration is below the detection limit of the portable XRF analyzer.

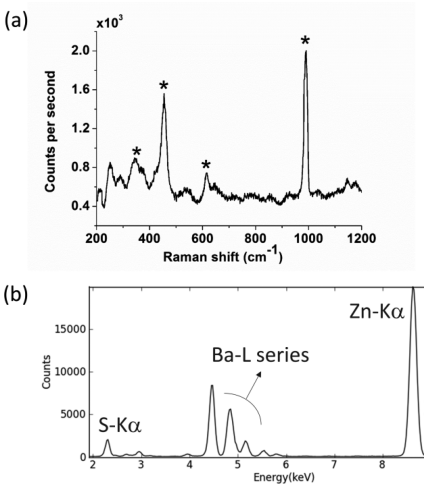

Figure 1. Analysis of Sample 2 with (a) Raman spectroscopy with 785 nm excitation; ZnS (348 cm^{-1}) and $BaSO_4$ (455, 616, and 987 cm^{-1}) Raman bands are marked with asterisks. (b) X-ray fluorescence spectroscopy.

SEM images for commercial lithopone and for representative historical samples are shown Figure 2. The intimate mixture of white ($BaSO_4$) and light gray (ZnS) particles demonstrates that coprecipitates of different dimensions have been formed, with the largest particles, on the order of 1 μm in diameter, present in samples S1, S3, and S4 (see SEM images of all samples in the Supporting Information). Differences in particle size can be attributed both to a different grinding grade and to effects of thermal treatments, which led to the formation of crystals of different sizes.

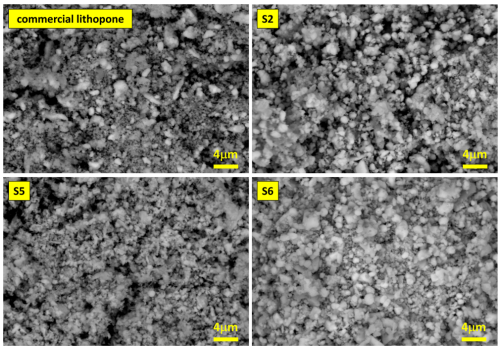

Figure 2. Scanning electron microscope images for commercial lithopone and historical samples S2, S5, and S6. Images highlight the presence of a uniform distribution of particles of ZnS and $BaSO_4$. Differences in particle size are ascribed to grinding grade or thermal treatments during pigment preparation. See Supporting Information for SEM images of other samples.

Preliminary PL measurements on bulk samples (data not shown) highlighted a noticeable emission from historical samples with a high variability among them, which was better investigated with PL microscopy: from an inspection of the RGB reconstructed maps of the emission (Figure 3), the historical samples have small localized luminescent centers, with a variable diameter of a few micrometers, emitting at different wavelengths, and are distributed over a more uniform and less-intensely emitting matrix. In general, blue (BL, λ = 500 nm), green-yellow (GL, λ = 550 nm), and orange (OL, $\lambda \geq$ 600 nm) luminescent centers can be clearly detected. In comparison, both commercial samples of lithopone and ZnS show a less intense emission with only few emitting centers.

Strong variations in historical samples are probably due to differences either in synthesis processes or in ores from which the pigments were produced. According to the color of the emission of the matrix and the distribution of impurities, three classes of lithopone are observed: samples S2 and S3 have strong-emitting luminescent centers mainly with maxima in the blue and in the green-yellow region of the electromagnetic spectrum; samples S1, S4, and S5 are associated with a weakly red-emitting matrix and have small multicolored luminescent centers; sample S6 has a strong blue-emitting matrix and a variety of small emitting centers of different colors. For all samples, we hypothesize that the localized emission centers are metallic impurities in trace concentrations unintentionally introduced into the ZnS crystal lattice during synthesis. The correlation between the wavelength emitted by the emitting center and its nature will be discussed in the following section.

Time-resolved imaging analysis, performed on the same areas observed using multispectral imaging, provided a characterization of their decay kinetics. The decay emission parameters of luminescent centers detectable in four samples (S2, S5, and S6, representing the three classes described above, and S4, characterized by a lower emission intensity) have been

DOI: 10.1021/acs.analchem.5b00560
Anal. Chem. 2015, 87, 6049−6056

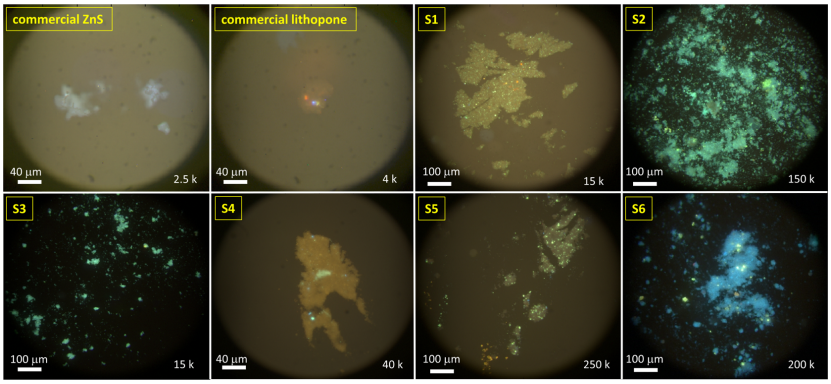

Figure 3. Reconstructed RGB images of the UV-induced PL emission for commercial samples of ZnS and lithopone and for the six historical lithopone samples (S1−6). At the bottom right of each image, the maximum PL intensity recorded is reported in counts. For commercial pigments, only a few luminescent centers have been detected, confirming the high purity of the material. Historical samples present a very bright luminescence, a uniform emitting matrix, and several localized centers of different size.

Table 2. Results of Analysis of Time-Resolved PL Decay Curves Fitted with a Multiexponential Model with a Maximum of Three Components, as Described in Ref 5, with Lifetime (τ_i) and Relative Weight ($A_i\tau_i$%) Values Given for Blue (BL), Green-Yellow (GL), and Orange (OL) Centers

	τ_1 (μs)	τ_2 (μs)	τ_3 (μs)	τ_1A_1 (%)	τ_2A_2 (%)	τ_3A_3 (%)	τ_{mean} (μs)	R^2
S2 (BL)	0.10	0.93	7.51	7.0	25.1	67.9	5.34	0.999
S2 (OL)	0.07	0.78	6.92	14.5	26.7	58.8	4.29	0.997
S4 (BL)	0.02	0.48	5.44	14.7	29.9	55.4	3.16	0.993
S4 (OL)	0.01	0.45	5.47	28.7	29.3	42.0	2.43	0.993
S5 (BL)	0.09	0.85	6.56	14.7	25.7	59.6	4.14	0.994
S5 (GL)	0.03	0.33	5.03	56.8	23.4	19.8	1.09	0.987
S5 (OL)	0.01	0.42	4.27	27.9	28.8	43.4	1.98	0.995
S6 (BL)	0.11	0.77	6.90	7.0	23.3	69.7	5.00	0.998
S6 (GL)	0.05	0.40	5.89	11.8	23.0	65.1	3.93	0.997
S6 (OL)	0.06	0.43	5.97	12.2	24.4	63.4	3.89	0.996

summarized in Table 2: PL decay curves are multiexponential in nature; all the samples are characterized by the presence of long-lived luminescent centers with an effective emission on the order of microseconds; the longest effective lifetime is always associated with the blue centers. The same trend was observed for all the samples (data not shown).

A detailed analysis of the emission from two representative samples, S5 and S6, is shown in Figures 4 and 5, with reconstructed RGB maps of the color of the emission, the emission lifetime map, PL spectra, and mean decay profiles of clustered emitting centers. In sample S5 (Figure 4), blue centers show effective lifetime τ_{mean} = 4.14 μs, green centers have τ_{mean} = 1.09 μs, and orange centers have τ_{mean} = 1.98 μs. The same analysis for sample S6 (Figure 5) highlights a blue luminescent matrix (τ_{mean} = 4.57 μs), blue emitting localized centers (τ_{mean} = 5.00 μs), green-yellow emitting centers (τ_{mean} = 3.93 μs), and a small cluster of orange luminescent inclusions (τ_{mean} = 3.89 μs). In sample S2, BL with the longest measured lifetime (τ_{mean} = 5.34 μs) and OL (τ_{mean} = 4.29 μs) emitting centers are detected, while in sample S4 BL (τ_{mean} = 3.16 μs) and OL (τ_{mean} = 2.43 μs) are identified. For these two samples, the analysis of the decay kinetics of the few green-yellow emitting centers gave inconsistent results, suggesting that more centers emitting at different wavelengths are superimposed, and we are unable to resolve them with our instrument. The presence of multiple superimposed centers was also found for sample S1.

EPR spectra registered from all historical samples exhibit a small peak at g = 4.3, a broad signal around g = 2.2, and a resolved hyper-fine pattern centered at g = 2 (shown in Figure 6a for sample S3). Figure 6b displays a highlight for the g = 2 region of the EPR spectrum for two representative samples (S1 and S3). A detailed discussion of the EPR results is provided below.

DISCUSSION OF RESULTS

Results obtained with PL and EPR can be explained by considering the historical synthesis of lithopone which involved the mixing of a solution of barium sulfide and zinc sulfate; the resulting coprecipitate of zinc sulfide and barium sulfate was then filtered, washed, and dried. Coprecipitation of the same amount of reagents is described by the following formula: $ZnSO_4 + BaS \rightarrow ZnS + BaSO_4$, yielding a product that is 29.4 wt % ZnS and 70.6 wt % $BaSO_4$.[20] This precipitate, generally referred to as crude lithopone, was then calcined at temperatures ranging from 600 to 900 °C and subsequently wet milled, filtered, and dried. The quality of the final lithopone depended essentially on two factors: the amount of ZnS with respect to that of $BaSO_4$[3] and the care exercised in the preparation of the two soluble salts, BaS and $ZnSO_4$, which

DOI: 10.1021/acs.analchem.5b00560
Anal. Chem. 2015, 87, 6049−6056

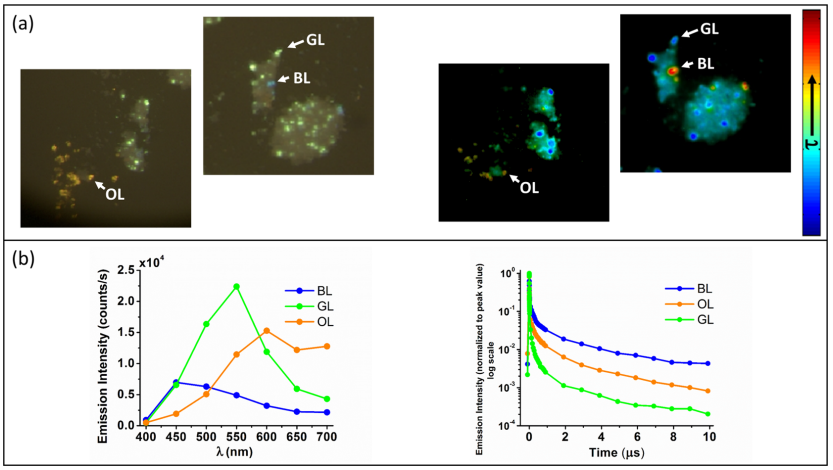

Figure 4. (a) RGB color maps of the PL emission for two selected areas of sample S5 (left) and lifetime maps of the same areas following monoexponential decay data fitting, shown in false color (right). RGB maps highlight the presence of small localized emitting centers giving rise to blue (BL), green-yellow (GL), and orange (OL) luminescence. Lifetime maps indicate that blue centers are the longest-living ones, followed by OL and GL. (b) PL spectra (left) and decay curves (right) recorded for the same sample in the areas labeled as BL, GL, and OL. The microsecond-decay kinetic behavior suggests that traps are responsible for the emitting centers.

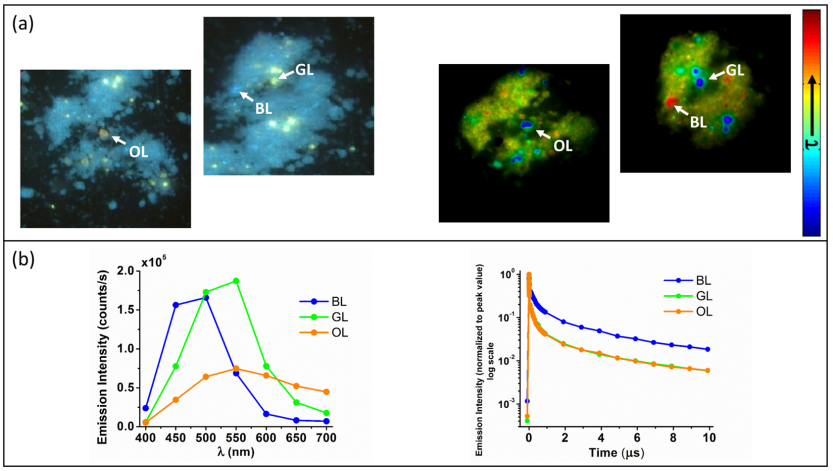

Figure 5. (a) RGB color maps of the PL emission for two selected areas of sample S6 (left) and lifetime maps of the same areas following monoexponential decay data fitting, shown in false color (right). These maps confirm the trend already observed for sample S5 in Figure 4: BL has a longer lifetime than GL and OL. (b) PL spectra (left) and decay curves (right) recorded for sample S6 in the areas labeled as BL, GL, and OL.

were prepared in the lithopone factory. $ZnSO_4$ was obtained by reprocessing zinc containing waste materials or directly from zinc ore. The most common ore employed was sphalaerite (historically known as zinc blende), a cubic resinous zinc iron sulfide mineral of composition (Zn,Fe)S.[21] Sphalerite is nearly always found with aluminum (Al) resulting from acidic weathering of rock and sulfide minerals, including salts of Mn, Cu, Ag, Cd, and Pb, resulting from mine drainage activity.[22] In order to obtain $ZnSO_4$, the zinc source material was leached in sulfuric acid, and other metallic impurities were precipitated as insoluble sulfides. The solution obtained was then filtered, washed, dried, and pulverized. Due to the impurity of the Zn sources and variability in the preparation of solutions, different metal impurities may have been introduced during various steps of lithopone synthesis.

Blue luminescence (BL) centers observed in lithopone samples can be attributed to interstitial Ag and Cu or to intrinsic ZnS defects. Ag substitutes Zn in the matrix and acts as an electron acceptor center, giving rise to an emission ranging from 420 to 440 nm depending on the presence of coactivators like Al (which usually causes a red-shift of the luminescence[17]). Cu forms two types of acceptor centers in ZnS matrix, and the

DOI: 10.1021/acs.analchem.5b00560
Anal. Chem. 2015, 87, 6049−6056

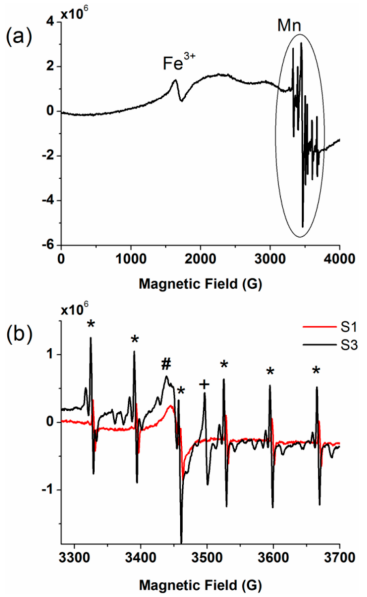

Figure 6. (a) EPR spectrum for sample S3. The Fe^{3+} signal with $3d^5$ electron configuration is observed at about $g = 4.3$. At about $g = 2$, a broad background signal is attributed to Mn ions in clusters. (b) Mn_{Zn}^{2+} hyperfine structure for samples S1 and S3 (the six peaks have been marked with asterisks): both the spectra are characterized by a system of lines surrounding each of the sextet sites, ascribable to crystal field effects small enough to be treated as perturbations. Organic radicals are also observed ($g = 2.009$, #) and ZnS defects ($g = 2.002$, +).

emission wavelength closely depends on the Cu-doped concentration:[13] the blue-Cu luminescence (BL) peaked at 472 nm is formed by positively charged interstitial Cu^+ ions $[Cu_i^+]$; Cu_i^+ centers trap electrons from the conduction band, which immediately recombine with free holes nonradiatively. Since the diffusion of Cu into the ZnS matrix is difficult, formation of interstitial Cu_i^+ centers can occur only with an excess of Cu doping. The so-called self-activated emission from crystals of ZnS, ascribed to the presence of intrinsic defects, also gives rise to blue luminescence.[7,8] A green-Cu luminescence (GL) peaked at 520 nm is formed by Cu substitutionally sitting at the Zn^{2+} site $[Cu_{Zn}^{2+}]$ acting as a recombination center for electrons from either conduction band or shallow donor sites (e.g., S vacancies). Green Cu emission can be quenched when the concentration of Cu impurities increases beyond a certain limit, indicated as 3.5×10^{-4} mol %,[10] which promotes the blue Cu_i^+ luminescence. Therefore, the ratio between these two peaks may be a good indicator of the concentration of Cu doping. Orange luminescence (OL) arises from the incorporation of traces of Mn^{2+} in the crystal lattice and is peaked at around 580 nm.[10] The mechanism for the orange luminescence from Mn^{2+} doped ZnS is similar to that of Cu_{Zn}^{2+}, but in this case, Mn^{2+} acts as an isoelectronic dopant that substitutes at the Zn valence sites and acts as an attracting site for holes $[Mn_{Zn}^{2+}]$ which therefore recombine with conduction band electrons or electrons in shallow donor sites.

PL properties show a complex behavior that reflects the great heterogeneity (different impurities and concentrations), confirmed by the multiexponential behavior of the luminescence decays. Few studies address the analysis of the dynamics of doped ZnS materials, and most highlight how differences in lattice structure are responsible for marked differences in kinetic properties: Lisensky et al.[23] modeled the dynamics of Cu-doped phosphors as a second-order equation, consistent with the recombination of equal populations of holes and electrons. Jayanthi et al.[12] measured the time-resolved decay of PL for undoped ZnS and ZnS/Cu nanoparticles, suggesting that, beneath the band gap excitation, carrier dynamics involves band to band excitation, trapping at sulfur vacancies, recombination at valence band or Cu level, and conduction band to Zn valence acceptor centers. Chen et al.[17] studied the role of codoping in the variation of the decay constant in Cu-doped ZnS phosphors. Due to the large range of applications of doped ZnS, its kinetic properties can be tuned from a microsecond up to several minutes; therefore, a comparison of time constants reported in this work with literature is not straightforward.

As a general feature, we can affirm that the type and concentration of dopants, as well as the local environment of an activator center, play a key role in determining the optical properties of the luminescence of lithopone, such as the intensity of the transitions and the energy at which the transitions occur. In addition, the environment of the activator may strongly affect the radiative decay time and the nature of the de-excitation mechanism.

EPR spectroscopy provides information on some of the structural and dynamic phenomena of lithopone samples and gives insights into impurities that influence their PL properties. The narrow peak at $g = 4.3$ (Figure 6a) arises from high spin $S = 5/2$ Fe^{3+} species; this peak is constant in all samples, and the concentration of Fe^{3+} can be considered similar for all samples. Fe is a common contaminant associated with spharelite with Fe^{2+} substitution for cation lattice Zn sites.[24] The presence of the Fe^{3+} state rather than Fe^{2+} might therefore be due to oxidation of spharelite $[Zn(S,Fe) + 2O_2 \rightarrow Zn(S,Fe)O_4]$ during the grinding process of the mineral.[25] The broad line around $g = 2.2$, observed for all samples, can be ascribed to the presence of trace Cu_{Zn}^{2+}, which was predicted by PL analysis as a justification for the GL. At around $g = 2$, a broad signal superposed over hyperfine structure is consistent with the presence of Mn as a cluster and Mn^{2+} substituting Zn^{2+} sites, which is a reasonable explanation for the OL.[26] Figure 6b highlights that this signal, consisting of a complex of six sharp lines, identified as hyperfine structure Mn^{2+}, is due to the interaction of electron spin of Mn_{Zn}^{2+} with its nuclear spin $I = 5/2$. The spectrum further contains a system of lines between each component of the sextet, identified as the so-called forbidden transitions coming from the zero field splitting interactions, when the nuclear spin changes simultaneously with the orientation of the electron spin, due to high spin state of Mn^{2+} species.[26,27] The other two components, respectively centered at $g = 2.009$ and $g = 2.002$, can be attributed to the presence of organic radicals and ZnS defects,[28] which might be partially responsible for the blue luminescence detected in historical samples, which could be ascribed to the self-activated emission from ZnS crystals.[7,8]

DOI: 10.1021/acs.analchem.5b00560
Anal. Chem. 2015, 87, 6049−6056

CONCLUSIONS

Laboratory analyses on six historical luminescent lithopone samples revealed the presence of several emitting centers associated with metal ion impurities unintentionally introduced during the pigment synthesis. PL microscopic imaging revealed the presence of centers emitting at different wavelengths in the visible region, of different color and intensity from blue to red.

The combination of spatial and temporal PL microscopic imaging enabled the identification and qualitative characterization of luminescent lithopone impurities, while EPR allowed a more complete description of the chemical composition of the material. The EPR results confirm the presence of Cu_{Zn}^{2+} and Mn_{Zn}^{2+} ions, acting as impurities in all the historical samples, whereas Ag traces could not be detected. Further, the EPR results indicate the presence of Fe as a constituent of the ZnS mineral ores.

A complete understanding of the PL emission mechanisms in this material is not straightforward and would require the determination of the concentration of impurities and the ratio between different impurities. In the future, such information could be achieved via inductively coupled plasma mass spectrometry (ICPMS) or secondary ion mass spectrometry (SIMS). Nevertheless, these techniques require the destruction of sample which was not possible in our study due to the limited amount of available material. Furthermore, to determine the concentration of impurities through ICPMS, calibration standards would be required.

EPR data complement the analysis of the defect luminescence mechanism in lithopone without any sample destruction. This work demonstrates that, in the future, the investigation of the microenvironmental complexity of painting materials could benefit from the use of EPR imaging over conventional EPR techniques: indeed, visualizing the spatial distribution of paramagnetic centers and their physical and chemical properties could provide absolute and direct quantitative comparison with luminescence imaging results. Moreover, further complementary mapping techniques would help to better characterize the pigment and its impurities, as μ-Raman and synchrotron-based μ-XRF imaging.

The multianalytical approach described in this work was designed to answer specific research questions about the optical properties of lithopone. In particular, in the historical lithopone samples studied, an intense PL emission is attributed to a synthesis process developed within a specific period and geographical area. The analysis of further historical samples of this pigment could help in understanding a possible correlation between these luminescence properties and sources and production methods. The results obtained encourage further exploration of the same protocol for the study of the intrinsic heterogeneity of other painting materials. Moreover, the information gained through this laboratory-based protocol can help in the future in the interpretation of results obtainable by means of in situ, nondestructive investigation of the luminescence properties of real paintings.

ASSOCIATED CONTENT

Supporting Information

Scanning electron microscope (SEM) images for all the samples shown in this work. The Supporting Information is available free of charge on the ACS Publications website at DOI: 10.1021/acs.analchem.5b00560.

AUTHOR INFORMATION

Corresponding Author

*E-mail: sara.bellei@polimi.it. Fax: +39 02 23996126.

Present Address

[‖]A.C.: Department of Scientific Research, The Metropolitan Museum of Art, 1000 Fifth Avenue, New York, USA.

Funding

Research was partially funded by the Italian Ministry of Education, Universities and Research within the framework of the JPI Cultural Heritage – JHEP Pilot call through the LeadART project "Induced decay and aging mechanisms in paintings: focus on interactions between lead and zinc white and organic material"; within the Future in Research 2012 program through the FUTURAHMA project "From Futurism to Classicism (1910–1922). Research, Art History and Materials Analysis"; and through the Bilateral Project between Italy and The United States of America, funded by the Italian Ministry for Foreign Affairs and International Cooperation.

Notes

The authors declare no competing financial interest.

ACKNOWLEDGMENTS

The authors gratefully acknowledge Joe Barabe of McCrone Associates for providing all the historical lithopone samples discussed in this artwork and Dr. Maria Cristina Mozzati (University of Pavia) for her contribution in the interpretation of EPR data.

REFERENCES

(1) Goshorn, J. H.; Black, C. K. *Ind. Eng. Chem.* **1929**, *21*, 348–349.
(2) Jantsch, G.; Wolski, P. US Patent 1,693,902, 1928.
(3) Capua, R. *J. Am. Inst. Conserv.* **2014**, *53*, 75–88.
(4) Boselli, L.; Ciattini, S.; Galeotti, M.; Lanfranchi, M. R.; Lofrumento, C.; Picollo, M.; Zoppi, A. *e-Preservation Sci.* **2009**, *6*, 38–42.
(5) Comelli, D.; Nevin, A.; Brambilla, A.; Osticioli, I.; Valentini, G.; Toniolo, L.; Fratelli, M.; Cubeddu, R. *Appl. Phys. A: Mater. Sci. Process.* **2012**, *106*, 25–34.
(6) Fang, X.; Zhai, T.; Gautam, U. K.; Li, L.; Wu, L.; Bando, Y.; Golberg, D. *Prog. Mater. Sci.* **2011**, *56*, 175–287.
(7) Denzler, D.; Olschewski, M.; Sattler, K. *J. Appl. Phys.* **1998**, *84*, 2841.
(8) Kurbatov, D.; Opanasyuk, A.; Kshnyakina, S.; Myelnik, V.; Nesprava, V. *Rom. Rep. Phys.* **2010**, *55*, 213–219.
(9) Cao, J.; Yang, J.; Zhang, Y.; Yang, L.; Wang, Y.; Wei, M.; Liu, Y. *J. Alloys Compd.* **2009**, *486*, 890–894.
(10) Ben, P. V.; Tue, P. T. *J. Sci. Math.* **2008**, *24*, 181–187.
(11) Chung, H. V.; Huy, P. T.; An, T. T.; Chien, N. D. *J. Korean Phys. Soc.* **2008**, *52*, 1562–1565.
(12) Jayanthi, K.; Chawla, S.; Chander, H.; Haranath, D. *Cryst. Res. Technol.* **2007**, *42*, 976–982.
(13) Manzoor, K.; Vadera, S. R.; Kumar, N.; Kutty, T. R. N. *Mater. Chem. Phys.* **2003**, *82*, 718–725.
(14) Hao, E.; Sun, Y.; Yang, B.; Zhang, X.; Liu, J.; Shen, J. *J. Colloid Interface Sci.* **1998**, *204*, 369–373.
(15) Murugadoss, A.; Chattopadhyay, A. *Bull. Mater. Sci.* **2008**, *31*, 533–539.
(16) Kawai, H.; Kuboniwa, S.; Hoshina, T. *Jpn. J. Appl. Phys.* **1974**, *13*, 1593–1603.
(17) Chen, Y. Y.; Duh, J. G.; Chiou, B. S.; Peng, C. G. *Thin Solid Films* **2001**, *392*, 50–55.
(18) Cesaratto, A.; D'Andrea, C.; Nevin, A.; Valentini, G.; Tassone, F.; Alberti, R.; Frizzi, T.; Comelli, D. *Anal. Methods* **2014**, *6*, 130.

DOI: 10.1021/acs.analchem.5b00560
Anal. Chem. 2015, 87, 6049–6056

(19) Brambilla, A.; Osticioli, I.; Nevin, A.; Comelli, D.; D'Andrea, C.; Lofrumento, C.; Valentini, G.; Cubeddu, R. *Rev. Sci. Instrum.* **2011**, *82*, 063109.
(20) Völz, H. G.; Kischkewitz, J.; Woditsch, P.; Westerhaus, A.; Griebler, W.-D.; De Liedekerke, M.; Buxbaum, G.; Printzen, H.; Mansmann, M.; Räde, D.; Trenczek, G.; Wilhelm, V.; Schwarz, S.; Wienand, H.; Adel, J.; Adrian, G.; Brandt, K.; Cork, W. B.; Winkeler, H.; Mayer, W.; Schneider, K.; Leitner, L.; Kathrein, H.; Schwab, E.; Jakusch, H.; Ohlinger, M.; Veitch, R.; Etzrodt, G.; Pfaff, G.; Franz, K.-D.; Emmert, R.; Nitta, K.; Besold, R.; Gaedcke, H. In *Ullmann's Encyclopedia of Industrial Chemistry*; Wiley-VCH Verlag GmbH & Co. KGaA: New York, 2000.
(21) Balabin, A. I.; Sack, R. O. *Mineral. Mag.* **2000**, *64*, 923−943.
(22) Cook, N. J.; Ciobanu, C. L.; Pring, A.; Skinner, W.; Shimizu, M.; Danyushevsky, L.; Saini-Eidukat, B.; Melcher, F. *Geochim. Cosmochim. Acta* **2009**, *73*, 4761−4791.
(23) Lisensky, G. C.; Patel, M. N.; Reich, M. L. *J. Chem. Educ.* **1996**, *73*, 1048.
(24) Hoffmann, H.; Heitz, R.; Broser, I. *Phys. Rev. B* **1990**, *41*, 5806−5816.
(25) Steger, H. F.; Desjardins, L. E. *Can. Mineral.* **1980**, *18*, 365−372.
(26) Liu, J.; Liu, C.; Zheng, Y.; Li, D.; Xu, W.; Yu, J. *J. Phys.: Condens. Matter* **1999**, *11*, 5377−5384.
(27) Stefan, M.; Nistor, S. V.; Ghica, D.; Mateescu, C. D.; Nikl, M.; Kucerkova, R. *Phys. Rev. B: Condens. Matter Mater. Phys.* **2011**, *83*, 1−11.
(28) Murase, N.; Jagannathan, R.; Kanematsu, Y.; Watanabe, M.; Kurita, A.; Hirata, K.; Yazawa, T.; Kushida, T. *J. Phys. Chem. B* **1999**, *103*, 754−760.

DOI: 10.1021/acs.analchem.5b00560
Anal. Chem. 2015, 87, 6049−6056

Appl. Phys. A (2016) 122:1053
DOI 10.1007/s00339-016-0578-6

Applied Physics A
Materials Science & Processing

Photoluminescence properties of zinc white: an insight into its emission mechanisms through the study of historical artist materials

A. Artesani[1] · S. Bellei[1] · V. Capogrosso[1] · A. Cesaratto[3] · S. Mosca[1] · A. Nevin[2] · G. Valentini[1] · D. Comelli[1]

Received: 6 July 2016 / Accepted: 17 November 2016 / Published online: 28 November 2016

Abstract While the photophysical properties of ZnO nanostructures have been widely explored, less research has focused on the bulk material present in artist pigments. This study is based on the analysis of historical pastels, representative of artist materials available at the turn of the twentieth century, and of the pure powder pigment as the control sample. The study of the intensity of the photoluminescence emission as a function of the fluence and of the nanosecond and microsecond emission decay kinetic properties allows the elucidation of the emission mechanisms in control ZnO and historical samples containing ZnO. Data suggest that in historical samples the near-band-edge free-exciton photoluminescence emission, typically occurring in the pure semiconductor, is influenced by the interaction of the pigment with surrounding organic binding material. Conversely, crystal defects, typically expected in historical samples following the imperfect synthesis process available at the beginning of the twentieth century, introduce minor modifications to the photoluminescence emission. The study further suggests that zinc carboxylates, detected in all historical samples and known to introduce characteristic groups on the surface of ZnO, could be responsible for changes in emission mechanisms. Research demonstrates how photoluminescence decay kinetics and the study of the dependence of the emission intensity on the fluence are powerful methods for elucidating the nature of the mechanism processes in luminescent semiconductor pigments.

Electronic supplementary material The online version of this article (doi:10.1007/s00339-016-0578-6) contains supplementary material, which is available to authorized users.

✉ A. Artesani
alessia.artesani@polimi.it

[1] Dipartimento di Fisica, Politecnico di Milano, Piazza Leonardo da Vinci 32, 20133 Milan, Italy

[2] Istituto di Fotonica e Nanotecnologie - Consiglio Nazionale delle Ricerche (IFN-CNR), Milan, Italy

[3] Department of Scientific Research, The Metropolitan Museum of Art, New York, NY, USA

1 Introduction

Zinc as a mineral has been known since antiquity, but historians agree that it was first used as a white pigment in the form of zinc oxide (ZnO) only at the end of the eighteenth century. The ZnO-based pigment, despite some initial concerns of its quality, substituted the lead white mainly because of its non-toxicity and its intense whiteness, and it was manufactured all over the world [1]. Zinc white was produced mainly via three processes: the indirect (or French) process, which produced the oxide by burning zinc metal in air, the direct (or American) process, which involved smelting zinc ore in a furnace [2], and the less common wet chemical process, in which ZnO was produced from purified solutions of other zinc-based compound [3]. The final pigment achieved with the three synthesis methods has different chemical properties and composition. Generally, the French process yields a very pure pigment (with a typical composition of ZnO in 99.69–99.99 wt% and trace concentrations of Pb, Cd and Fe) [4]. Conversely, the direct process was widely noted for its simplicity, low cost and excellent thermal efficiency, but it produced a less pure form of ZnO (purity $> 98.5\%$) with a variety of possible impurities, including Pb, Cd, Fe, S, Cu and Mn [5]. Significant traces of Pb, Cd and S are also associated with the pigment produced through the wet process [4, 6].

In its pure form, ZnO is a semiconductor belonging to II–VI group and has two main crystalline forms. The hexagonal structure (wurtzite) is the most stable at ambient conditions and therefore the most common with band gap energy of 3.37 eV (368 nm) at room temperature. The second structure is the cubic one (zincblende), typically formed at high pressure [7] and for this reason less common, with a lower absorption edge energy (2.7 eV, 459 nm). In the 1970s, ZnO gained substantial interest for its optoelectronics applications as a potential material for light emitting devices [8, 9]. Subsequently, interest in ZnO has been motivated as it is a promising material for the synthesis of a variety of nanostructures and nanostructured devices [10].

One of the most suitable ways to study the energy levels of semiconductors is through photoluminescence (PL) spectroscopy [11]. ZnO exhibits different PL bands: one corresponding to an emission near the band-edge (NBE) in the UV region, while a broad band in the visible region is due to emission from trap states (TS) caused by intrinsic defects and impurities in the crystal structure. One of the most common TS emissions is centred in the green spectral region (around 5200 nm). The source of this green luminescence was first attributed to extrinsic defects incorporated in synthesis processes, particularly Cu ions [12]. At present this hypothesis is questioned and many agree that various centres may be simultaneously involved in green luminescence, principally intrinsic defects such as interstitial or vacancies of zinc and oxygen [13].

In order to obtain a pictorial material, ZnO, as a powder, is dispersed in a binder typically of lipidic or proteinaceous nature and, in commercial paint or pastels, is mixed with additives. Pictorial binders allow the insoluble pigment to bind and adhere to a pictorial surface. Clearly, ZnO as a white pigment or embedded in painted layers has a much more complex matrix than that of the pure semiconductor material. However, only few works have focused on the PL of ZnO paint. For example, Clementi et al. [14] studied the PL properties of zinc oxide in oil paints; it was reported that the direct recombination emission of the white pigment is notably enhanced in intensity by interactions with lipid binders, suggesting that this was caused by covalent bonds between zinc atoms and carboxylates (known also as zinc soaps). On the contrary, the green emission was poorly specific and possibly overlapped with the emission of the binding medium. With the aid of synchrotron-based PL microscopy [15, 16], it has been shown that historical ZnO-based samples, which emitted homogeneously on the macroscale in the region 490–510 nm, were spatially inhomogeneous on the sub-micrometre scale with the addition of specific PL signals at 410 and 425 nm. It has been suggested that these emissions, ascribed to defect-induced states within the band gap, could be indicative of manufacturing processes or long-term alterations of the pigment. Hence, zinc-based pigments present additional issues with respect to the pure semiconductor material which merit further studies.

Here, we have applied an in-depth study of the PL properties of ZnO-based historical pastels and of the pure zinc white pigment, used as a reference sample. The study is based on the recovery of the lifetimes of the different PL emission mechanisms and on the study of the dependence of the PL emission intensity on the fluence. With respect to traditional PL spectroscopy, both approaches provide quantitative information correlated with the presence of competitive radiative and non-radiative decay paths and allow the elucidation of the nature of the PL mechanism processes in semiconductor materials and pigments [17–19].

2 Materials and methods

2.1 Samples

Twelve historical Zn-based samples from the beginning of the twentieth century have been investigated. The samples, produced by Lefranc & Bourgeois, are in the form of pastel fragments of different hues (Table 1; Fig. 1). A reference sample was prepared by pressing zinc white (Kremer Pigmente GmbH) in powder form as a pellet (in the following, labelled as control ZnO). The significance of this group of samples relies on the fact that they are representative of complex modern painting materials, produced after the second Industrial Revolution by one of the most important pigment producers.

2.2 Methods

2.2.1 Raman spectroscopy

Analysis was performed using a portable Raman spectrometer [20] to detect the molecular bulk composition of samples. The device is based on a 785-nm CW laser source and a spectrometer, mounting a 600 grooves/mm grating and coupled to a front-illuminated cooled CCD. The system allows the detection of Raman peaks in the spectral range 150–3000 cm^{-1} with a spectral resolution close to 15 cm^{-1}. The laser and the spectrometer are connected through optical fibres to the probe, working in back-scattering geometry. The working distance is $\sim$3 mm, while the spot size on the sample is 50 μm in diameter. The power density on samples has always been kept below 1500 W cm^{-2}. Following spectral calibration and baseline correction, each spectrum is treated with the mathematical subtracted shift Raman spectroscopy (SSRS) method (with a spectral shift of 15 cm^{-1}) [21–23] to reduce the

Table 1 Spectroscopic analyses of historical and commercial samples

Sample	Hue	XRF	FE-SEM	Raman	FTIR	Identification
S01	White	**Zn**. Fe, Co, Ni, Ca	**ZnO, ZnS**. Al, Si, Ca, Cu	ZnO (438 cm^{-1}) (s) wax (1064 cm^{-1}) (m) linseed oil (1157, 1085 cm^{-1})	Zinc stearate wax linseed oil	Zinc white* zinc sulphide
S02		**Zn**. Fe, Co, Ni, Pb	**ZnO, ZnS**. Al, Si, Cu			
S03			**ZnO, ZnS**. Al, Cu Ca localized			
S04		**Zn**. Fe, Co, Ni, Ba	**ZnO, ZnS**. Al, Si, Ca, Cu, Fe			
S05	Lilac	**Zn, Mn**. Fe, Co, Ni, Ca, (Ba)	**ZnO, ZnS**. Al, P, Mn	ZnO (438 cm^{-1}) (s) wax (1064 cm^{-1}) (m) linseed oil (1157, 1085 cm^{-1})	Zinc stearate wax linseed oil Manganese violet	Zinc white* manganese violet
S06	Pale pink	**Zn**. Fe, Co, Ni	**ZnO, ZnS**. Al, Si, Ca, Cu Mg, K, Fe	ZnO (438 cm^{-1}) (s) wax (1064 cm^{-1}) (m) linseed oil (1157, 1085 cm^{-1})	Zinc stearate wax linseed oil	Zinc white* zinc sulphide Lake pigment
S07	Red	**Zn, Hg**. Fe, Co, Ni, S, Ca	**ZnO, ZnS**. Al, Si, Ca, Cu Hg, S correlated	HgS (252, 343 cm^{-1}) (vs.)		Zinc white* zinc sulphide Cinnabar
S08	Blue	**Zn**. Fe, Co, Ni, S, Ca	Not measured	Ultramarine (548 cm^{-1}) (vs.)	Zinc stearate wax linseed oil Ultramarine	Zinc white* ultramarine blue
S09	Green	**Zn, As, Cu**. Fe, Co, Ni	**ZnO, ZnS**. Al As, Cu correlated	ZnO (438 cm^{-1}) (s) wax (1064 cm^{-1}) (m) linseed oil (1157, 1085 cm^{-1})	Zinc stearate wax linseed oil Emerald green	Zinc white* zinc sulphide Emerald green
S10	Light grey	**Zn**. Fe, Co, Ni, Ca, Ba	Not measured	ZnO (438 cm^{-1}) (s) wax (1064 cm^{-1}) (m) linseed oil (1157, 1085 cm^{-1}) Carbon black (1325 cm-1) (br vs)	Zinc stearate wax linseed oil	Zinc white* carbon Black
S11			**ZnO, ZnS, $BaSO_4$** Al, Si, P, Cu Ca localized			Zinc white* zinc sulphide Lithopone carbon Black
S12	Red	**Zn, Fe**. Co, Ni, (Ba)	**ZnO, ZnS, $BaSO_4$**. Al, Si, Ca, Cu Fe	Fe_2O_3 (222 cm^{-1}) (vs) wax (1064 cm^{-1}) (m)		Zinc white* zinc sulphide Lithopone Fe-red pigment lake pigment
ZnO	White	**Zn**. Fe, Co, Ni	**ZnO**. Al	ZnO (438 cm^{-1}) (s)	Zinc oxide	Zinc oxide

Elements or compounds with strong signals are highlighted in bold, and other trace elements are reported. Some elements are listed in parentheses because their presence is unsure. If not specified, elements revealed with FE-SEM analysis were uniformly distributed, otherwise they are marked as localized or correlated if they are present as spots alone or localized in the same spatial position of other elements. The intensity of Raman peaks is specified using the usual symbols (*s* strong, *m* medium, *w* weak, *v* very, *sh* shoulder, *br* broad). Note that the peak at 438 cm^{-1} of ZnO with Raman is not always visible because of the luminescence in some pigments (S07, S08 and S12). In 'Identification' column, we have called zinc white* the basic composition zinc oxide, wax and linseed oil

Fig. 1 Colour picture of the historical samples

fluorescence background which is combined with Raman vibrations in the spectrum. The Raman spectrum is reconstructed by integrating the SSRS profile. The identification of pigments is finally achieved through comparison with Raman spectra from published databases [24, 25].

2.2.2 XRF spectroscopy

Measurements on samples were carried out using a portable X-ray fluorescence (XRF) spectrometer (Elio, XGLab srl) to detect their elemental bulk composition. The instrument is a fast system with a large-area silicon drift detector (SDD) (25 mm^2). The excitation source works with a Rh anode (Lα emission line at 2.69 keV), and the beam is collimated to a spot diameter on the sample of about 1.3 mm. The spectrometer detects elements from Na to Ur with an energy resolution below 135 eV, whereas lighter elements cannot be detected since the spectral region below 3 keV is covered by the intense emission of Rh tube. For all measurements, the following experimental conditions have been used: working distance $\sim$1.4 cm, tube voltage = 40 kV, tube anode current = 100 A, acquisition time = 40 s. XRF spectra of all samples have been processed in order to identify the detected emission lines. For the purpose, we have used the PyMCA software [26], based on a nonlinear least-squares fitting procedure which optimizes zero, gain, noise and Fano factors for the entire fitting region and for all XRF peaks simultaneously. The background was estimated with the strip background model.

2.2.3 FE-SEM

Morphologies and microstructure of samples were imaged with a field-emission scanning electron microscope (FE-SEM) designed for high vacuum operational mode (Tescan-Mira High Resolution Schottky FE-SEM). Working at 30 kV acceleration voltage allowed to achieve 1.2 nm as resolution for secondary electrons. The same system was used for energy-dispersive X-ray (EDX) analysis to map distribution of selected elements, allowing the inspection of the spatial correlation between two or more elements. Samples were prepared for FE-SEM/EDX analysis by removing very little material from the surface of pastel grains and subsequently depositing it onto carbon tape adhesive tabs. The FE-SEM method allows also the reconstruction of the mean elemental composition of samples in the analysed field of view (100 × 100 μm). In comparison with the bulk elemental composition detected with XRF spectroscopy, the method is also sensitive to lighter elements.

2.2.4 FTIR

Microsamples from the pastels were collected and analysed by Fourier transform infrared spectroscopy (FTIR), using a Nicolet 6700 spectrophotometer coupled with Nicolet Continuum FTIR microscope equipped with an MCT detector (acquired between 4000 and 600 cm^{-1} with 128 acquisitions and 4 cm^{-1} resolution) and equipped with a microcompression diamond cell. The spectra were baseline corrected using Omnic software and normalized on the intensity of the CH_3 stretching vibration (at about 2910 cm^{-1}).

2.2.5 Time-resolved photoluminescence spectroscopy

The system is based on a pulsed laser and on a fast-gated intensified camera coupled to a spectrometer. The camera is capable of high-speed gating to capture the decay kinetic of PL emission spectra. Excitation of PL from samples is provided by the third harmonic of a Q-switching Nd:YAG laser, emitting sub-ns pulses at 355 nm (CryLas FTSS 355-50, Crylas GmbH, Berlin, Germany) at a repetition rate of 100 Hz. The laser light is delivered to the sample through a multimode silica fibre (600 μm core). An optical probe allows the excitation of the PL signal from sample surface in a circular spot of 1 mm in diameter with a maximum fluence per pulse of 10^2μJ cm^{-2} equivalent to an average power density of 0.1 W cm^{-2}. PL emission from samples is collected in a back-scattering geometry and focused into the entrance slit of an imaging spectrometer. The spectrometer (Acton Research 2300i, focal length = 300 mm, *f*/4 aperture) mounts a 150-lpmm grating and enables us to record PL spectra in the spectral range 380–700 nm with a spectral resolution of 10 nm. The kinetics of the emission is detected by a gated intensified camera (C9546-03, Hamamatsu Photonics, Japan), mounted at the exit port of the spectrometer. The detector features an acquisition gate adjustable from 3 ns to continuous mode. A custom-built trigger unit and a precision delay generator complete the system, which has a temporal jitter close to 500 ps. The measurement procedure is based on the detection of a sequence of PL-gated spectra at different delays with

respect to the laser pulses. In this work, the NBE emission was detected by employing a gate width of 5 ns and properly sampling the first 30 ns of the decay kinetic. Emission from TS levels was detected with a gate width of 1 μs and recording the long-lived decay kinetic in the first 20 μs. In the last configuration, a long-pass filter (SCHOTT 400 nm) was placed in the collection path to remove the NBE emission. Following proper calibration of spectral data and correction for the detector efficiency, it is possible to observe PL spectra from the samples in a selected temporal gate window (in the following quoted as gated spectra) or to observe the emission decay kinetic in a proper spectral window. In the latter case, a multiexponential decay (with a maximum of three components) was fitted to the kinetic data integrated over a selected spectral region [27], using a nonlinear least-squares fitting methods applied to the model function:

$$f(x) = \sum_{i=1}^{3} A_i \tau_i \left(1 - e^{-w/\tau_i}\right) e^{-t/\tau_i} \quad (1)$$

where τ_i and A_i are the lifetime and the intensity of the ith decay component, respectively, while w is the width of the experimental gate. The effective lifetime is then calculated as the average of the lifetimes weighted over the number of photons originating from each decay path, according to the equation:

$$\tau_{\text{eff}} = \frac{\Sigma_i A_i \tau_i^2}{\Sigma_i A_i \tau_i} \quad (2)$$

2.2.6 PL spectroscopy at different fluences

PL spectroscopy was performed by employing a CW compact spectrometer and the same 355-nm pulsed laser source employed for TRPL measurements. The compact spectrometer (TM-CCD C10083CA-2100, Hamamatsu Photonics) mounts a back-thinned CCD image sensor and a transmission-type grating, which allows the recording of spectra in the range 320–1100 nm with a spectral resolution of 6 nm. Through fibre optics, both the laser and the spectrometer are connected to a remote optical probe, working in the 45°–0° configuration. The probe focuses the excitation light as a spot of approximately 1 mm in diameter on the sample at a distance of 35 mm and collects the fluorescence emission as well. The optical probe is equipped with a variable neutral density filter that allows the variation of the fluence of two orders of magnitude: in the present case, fluence on samples was varied from 0.1 to 1 μJ cm^{-2} . PL spectra are reported following background subtraction (achieved by acquiring the detected signal with the laser switched off) and correction for the spectral efficiency of the device.

2.2.7 Analysis of PL and TRPL-gated spectra

PL spectra and TRPL-gated spectra are always shown following correction for self-absorption phenomena in coloured samples on the basis of a Kubelka–Munk correction model described elsewhere [28]. The diffuse reflectance $R(\lambda)$ of the samples at all emission wavelengths and at the 355-nm excitation, required for applying the correction model, was collected with a visible reflectance spectroscopy device. This device is based on the same set-up employed in steady-state PL spectroscopy by substituting the UV laser source with a fibre-coupled halogen lamp (Lamp HL-2000-HR) having a nominal output power of 8.4 mW. Reflectance spectra of samples were determined using a diffusive reference sample (Spectralon Labsphere 0D074-2298). Following correction for self-absorption phenomena PL and TRPL-gated spectra, linked to the visible emission from trap state levels in the ZnO samples, were deconvoluted as the sum three Gaussian shape functions to provide a rough discrimination of decay paths originating from different TS levels. Peak positions of the three Gaussian functions were retrieved by applying a nonlinear fitting procedure, based on the minimization of the χ^2 error, while the spectral width of the Gaussian function was kept fixed at a third of the total spectral width of the visible emission. This constrain was necessary to better interpolate the curves in terms of errors of fitting parameters.

3 Results

3.1 Preliminary characterization of samples in terms of composition

Results of preliminary analyses are summarized in Table 1, and all spectra data (XRF, Raman and FTIR) plus SEM images are shown in Supplementary Material. The historical samples all contain zinc oxide (ZnO), in some cases zinc sulphide (ZnS), probably added as an extender of the white pigment, and wax and linseed oil as binders. The different hues of pastels were achieved with the addition of coloured pigments, in most cases easily identified by Raman and XRF spectroscopy: Carbon Black in grey pastels (S10, S11), Ultramarine Blue and Emerald Green in the blue (S08) and green pastels (S09), respectively. Reddish hues were achieved with the addition of Cinnabar (S07), Manganese violet (S05) and a Fe-based red pigment (S12). Interestingly, FE-SEM analysis showed the presence of Ca, K, S in S06 and in S12. These elements are usually correlated with the presence of a lake pigment that could also contribute to the colour of these samples.

Trace element impurities were further detected. For example, XRF highlighted Fe, Co and Ni in all samples, and Ca and Ba in some of them. Complementary, FE-SEM analysis detected elements uniformly distributed within the samples, such as Al and Cu, while others are more localized. The most complex composition was found in samples labelled S06, S12. A lower but still significant number of elements were also detected in samples S03 and S04. These samples contain, in addition to the elements cited above, traces of Mg, Si and P. These trace elements can be related to the presence of other pigments, added to achieve a specific hue, or to impurities unintentionally introduced during the imperfect synthesis processes. FE-SEM images of samples are shown in Supplementary Material and reveal very fine particles of ZnO distributed in an organic matrix, which vary with sample in concentration and morphology. The control sample has the finest particle size.

FTIR analysis, besides confirming the presence of wax and a drying oil, detected zinc stearate in all historical samples. This compound might be an additive, or more often it is associated with the formation and aggregation of zinc soaps [29, 30].

Finally, it is worth noting that the control ZnO sample was found to be quite pure, containing only Al impurities revealed by FE-SEM analysis and traces of Fe, Co and Ni highlighted by XRF analysis.

3.2 Photoluminescence spectroscopy

PL spectra of all samples, shown in Fig. 2, were detected upon an excitation fluence of 10 μJ cm^{-2}. Samples show a narrow emission band in the near-UV and a broad emission band in the green spectral range associated, respectively, with radiative recombination from the band-edge (BE) and via trap state (TS) levels. In terms of the spectral shape of the NBE emission, all samples share similar features: a narrow emission peaked at 382.7 nm with a FWHM around 13.2 in the control sample, and a close emission peaked at 382.3 nm (±0.4, 1σ) with a FWHM around 12.5 nm (±0.1, 1σ) in all historical samples.

The TS emission is more complex. In historical samples, we detected an emission centred at 530 nm with significant variation among samples, such as the FWHM and its relative intensity with respect to the NBE, as shown in Fig. 2. Conversely, in control ZnO the TS emissions less intense than that in historical samples. Further, it is red shifted with a broad emission centred at 570 nm. The broad TS emission detected in all samples is clearly the superposition of the emission from a variety of trap state levels close each other. In order to provide a simple decomposition for this broad emission, PL spectra of all samples were fitted as the sum of three Gaussian components, with maxima at 490 nm (TS1), 530 nm (TS2) and 570 nm (TS3). Despite the slight differences among samples in the peak position and weight of each Gaussian contribution, every interpolation resulted in a good 2 value, always higher than 0.999 (Table SM2). As an explanatory example, the fit result for sample S02 is reported in Supplementary Material: experimental data appear to be perfectly reproduced by the sum of three Gaussian functions with a prediction bound of 1 sigma, and the fitting residuals being lower than 2% than the intensity of the emission. Similar fitting results have been achieved for all the other samples (data not shown).

We systematically investigated the fluence dependency of NBE and TS emission for the control ZnO sample and a representative selection of five historical samples (those characterized by the most different chemical composition). It is worth noting that at the maximum employed excitation fluence (10^2 μJ cm^{-2}), we have not detected any photo-induced effect and any visible modification or darkening of samples, as expected for the stable crystalline structures of semiconductors. First, the NBE emission in all samples has a non-symmetric quasi-Gaussian shape

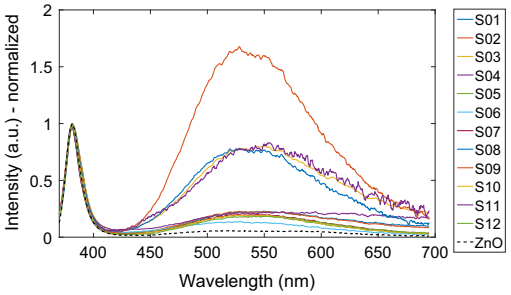

Fig. 2 Photoluminescence spectra acquired with 355 nm excitation for historical samples (*continuous lines*) and control sample (*dashed line*) under fluence of 10 μJ cm^{-2}. Spectra are corrected for self-absorption and instrumental efficiency

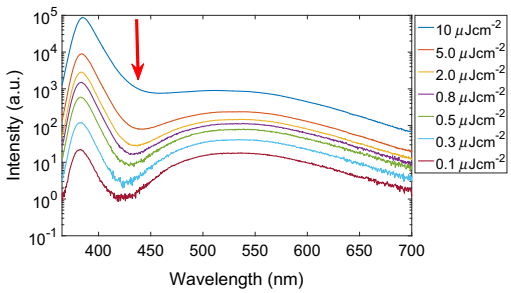

Fig. 3 PL spectra of control ZnO as a function of fluence, from 10 to 0.1 μJ cm^{-2}. At higher fluence, the shoulder of the NBE emission (indicated with a *yellow arrow*) is observed, yielding an apparent *red* shift of the NBE peak position of 3 nm

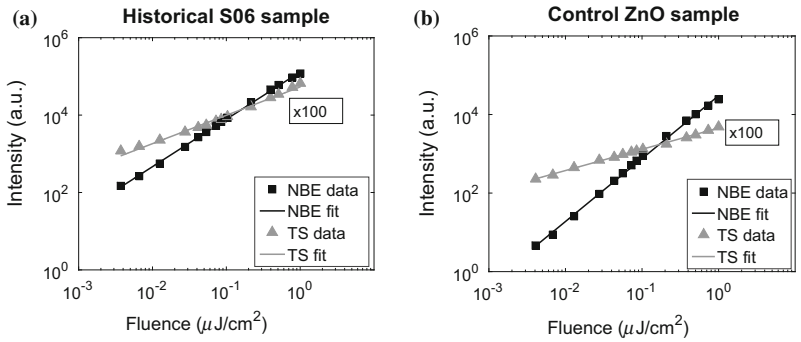

Fig. 4 PL intensity (as total emitted counts) in the NBE spectral band peaked at 382 nm (*grey triangles*) and in the TS spectral band peaked at 530 nm (*black squares*) versus the fluence in log–log scale for **a** historical S06 sample and **b** control zinc oxide sample. For better visibility, data of TS intensity are multiplied by a factor of 100. The results of linear fitting of data in the log–log scale are reported as *continuous lines*

Table 2 Characteristic coefficients for NBE and TS emissions

	NBE		TS		
	k	τ_{eff} (ns)	k	τ_{eff} (μs)	$\hat{\lambda}$ (nm)
S01	1.35	1.27	0.74	2.66	530
S02	–	1.23	–	3.35	529
S03	1.40	1.68	0.66	3.84	533
S04	1.23	1.38	0.71	2.85	534
S05	–	1.22	–	3.23	531
S06	1.20	1.15	0.72	2.52	532
S07	–	1.38	–	2.99	534
S08	–	1.49	–	3.21	524
S09	–	1.00	–	4.18	523
S10	–	1.29	–	3.45	526
S11	–	1.18	–	3.86	525
S12	1.24	1.46	0.66	2.94	541
Average ($\pm\sigma$)	1.28 ± 0.09	1.31 ± 0.20	0.70 ± 0.04	3.26 ± 0.60	530 ± 5
ZnO	1.58	0.55	0.54	5.27	567

The coefficient k expresses the angular dependence of intensity on fluence in log–log scale ($\log(I) = \log(I_0) + k \cdot \log(F)$). The effective lifetime (τ_{eff}) is calculated following a nonlinear fit of (a) bi-exponential decay model for NBE ($\lambda = 390$ nm, $\Delta\lambda = 10$ nm) and (b) tri-exponential decay model for TS ($\lambda = 530, \Delta\lambda = 100$ nm). $\hat{\lambda}$ represents the centre of the TS emission band. The average value in historical samples of the coefficients is reported together with the variance (σ)

that becomes more evident at higher fluences. In fact, changing the fluence from 0.1 to 10 μJ cm^{-2}, the shoulder of the NBE emission increases at longer wavelengths yielding an apparent red shift of the NBE peak position of 3 nm (Fig. 3). This effect is present in both control and historical samples. The asymmetric shape of the NBE emission has been interpolated with two Gaussian functions, peaked at 382 nm and 390 nm. The latter peak is referred to as the blue emission (BL) from herein. Second, the intensity of the NBE and TS emission was plotted as a function of excitation fluence, and an example of the results is shown in Fig. 4 for sample S06 and control ZnO. Similar data were recorded from historical samples (data not shown). In plots on the log–log scale, it can be seen that the NBE emission intensity is more pronounced than the TS emission and this difference is more evident in the control sample. The slope of the log–log curve is reported in Table 2, following the modelling of data with the relationship $I = I_0 \cdot F^k$ (that in a log–log scale gives rise to a linear behaviour $\log(I) = \log(I_0) + k\log(F)$), where I is the emission intensity and F is the laser fluence on sample [17, 18].

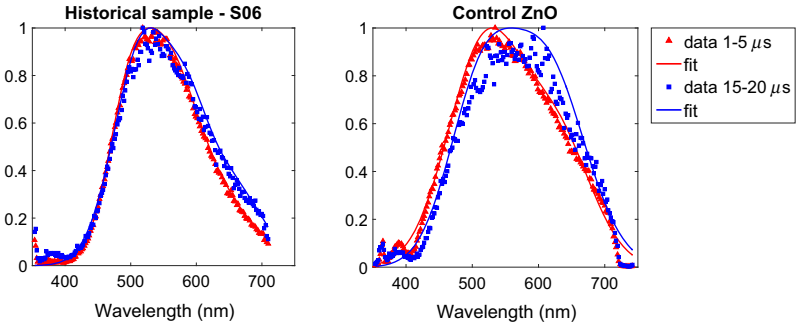

Fig. 5 Time-gated spectra of one historical sample (S06) and control ZnO sample. The *red line* is the interpolation for the emission gated in 1–5 μs, while the *blue line* is the interpolation for 15–20 μs gated spectra. Spectra are corrected for self-absorption and instrumental efficiency

Finally, TRPL spectroscopy analysis on all samples with an excitation fluence of 10^2 μJ cm^{-2} was performed to estimate the emission decay kinetics of the NBE and TS emissions. NBE emission gave rise to a nanosecond decay, which was well modelled with a bi-exponential decay. The full results of the fitted decay kinetic parameters are provided in Supplementary Material, whereas synthetic results, in terms of the effective lifetime, are reported in Table 2. It is noted that the lifetime values recorded from historical samples are comparable with an average value of $\tau_{eff} = 1.31$ ns, $\sigma = 0.20$ ns (with values ranging in the interval 1.0–1.7 ns), whereas control ZnO has a much shorter lifetime ($\tau_{eff} = 0.55$ ns).

For the TS emission, the use of a gated detector was particularly effective for the removal of the nanosecond emission from organic compounds in historical samples (such as that associated with organic binders and carboxylates [31]). In fact, emission from organic compounds, typically occurring in the visible spectral range, is spectrally superimposed with the visible TS emission and hence represents a serious limit to the proper analysis of trap state levels with conventional steady-state PL spectroscopy devices, as recognised previously. In all samples (historical and the control), the TS emission is characterized by decay kinetics with detectable differences in the different regions of the analysed spectral range. This confirms that the broad TS emission is actually the superposition of the contributions from different trap state levels, characterized by different trapping lifetimes. In particular, TRPL-gated spectra are slightly red shifted at longer delays, and the effect is most visible in the control sample (Fig. 5): from a physical point of view, this phenomenon suggests that the deepest traps (occurring at lower energy in the band gap and hence at longer emission wavelengths) have the slowest decay kinetic. The TS decay kinetic has been modelled as the sum of three exponential decay functions. Results, in terms of the effective lifetime detected in the whole spectral range, are reported in Table 2. Lifetime values are similar among historical samples varying between 2.5 and 4.2 μs and have an average value of $\tau_{eff} = 3.26$ μs ($\sigma = 0.60$ μs). In comparison, control zinc oxide has an effective lifetime for trap state emission of $\tau_{eff} = 5.27$ μs.

4 Discussion

Many studies have reported on the PL emission of ZnO, but at present, some of the photophysical properties of this semiconductor pigment in complex painted layers or in complex artist materials are still poorly understood. It is important to stress here that the recent literature on ZnO is primarily focused on the semiconductor employed as a nanomaterial, whereas few works deal with bulk ZnO. Erdem [32] reported a study on analogies and differences among photoluminescence produced by bulk and nanoparticles ZnO. The main result was that the latter produced a more intense emission in the green region, while for bulk materials the recombination via the conduction band is the strongest. Moreover, Djurisic and Leung [33] suggested that the defect behaviour in nanoparticle and bulk materials is similar and the main difference is the density of defects on the surface that is greater in nanoparticles.

Bearing in mind that the majority of contemporary literature deals with nanoparticle materials, we here discuss the current attribution for the green emission in ZnO. While the origin of photoluminescence in zinc oxide is contested, generally, the peak around 380 nm is associated with near-band-edge emission, while different defects are responsible for the green emission around 530 nm. This broad emission is well known in literature, and some hypotheses for its attribution have been suggested. Many agree that the main species responsible for the green

emission are oxygen and zinc vacancies (V_O and V_{Zn}) and interstitial defects of Zn (Zn_i). In studies on nanoparticles, Han et al. [34] have discriminated the emission from Zn_i to the valence band, which produces luminescence at 430 nm, and the emission from Zn_i to V_{Zn} which lead to emission at 480 nm. Other authors ascribe V_O as being mainly responsible for 530-nm emission [13, 35]. Interestingly, many recent studies achieved by combining experimental and computational simulation have pointed out that the green emission originates from surface intrinsic defects [36–38]. Apart from these simple findings, the analysis of the fluence dependence of the PL emission and the analysis of the PL emission lifetimes have provided additional information on the different recombination paths detected in control ZnO and historical samples, which are summarized and discussed below.

4.1 Control zinc oxide

The study of the behaviour of the PL intensity as a function of the fluence allows the identification of the underlying recombination process [17]. As a general result, it has been reported that the intensity of the NBE PL emission is proportional to F^k, where F is the fluence of the exciting laser radiation and $1 < k < 2$ for exciton-like transitions and $k < 1$ for free-to-bound and donor–acceptor pair transitions, respectively [17, 18]. Here, the dependency on fluence of the NBE emission was found to be over-linear with a characteristic coefficient of $k = 1.58$, which clearly suggests a free-exciton recombination path, as reported for other studies on pure ZnO samples [41]. The finding is confirmed by time-resolved PL analysis: the NBE emission of control ZnO has a sub-nanosecond lifetime, in very good agreement with data reported in the literature for ZnO as a thin film or single crystal, showing a typical lifetime value of 0.55–0.70 ns at 300 K temperature [39].

Recombinations via trap states are more complex. The k value for TS emission was less than one $k = 0.54$, suggesting a sub-linear dependency on fluence, which is characteristic of free-to-bound and donor–acceptor transitions originated from trap state levels in non-perfect crystals. Further, the detection of a microsecond decay kinetic confirms the nature of this green emission as originating from trapped electrons. More interestingly, in this broadband, ascribed to emission from a variety of trap state levels, the effective lifetime increases with increasing of wavelength and conversely the k value decreases, as reported in Table 3. This finding suggests that for recombination in deeper trap state levels (characterized by a PL emission occurring at longer wavelengths) trapped electrons are more stable (longer lifetime) and the related trap levels are less easily depopulated (lower k value). Even though it is not possible to provide an identification of the type of defects emitting at shorter/longer wavelengths in this broad visible band (with particular reference to defects related to Zn and O vacancies), it is worth noting that a similar behaviour of the k coefficient has been reported in reference [40], where the visible PL and cathodo-luminescence emission from Zn- and O-rich ZnO samples have been investigated. In both types of non-stoichiometric ZnO samples, the visible emission has a sub-linear dependence on fluence, with the emission observed in Zn-rich samples occurring at shorter wavelengths and with an intensity that increases at a significant faster rate than what observed in O-rich samples.

Finally, another result provided by the study of the PL emission as a function of fluence is that NBE emission is characterized by a second near emission (BL), with peak position around 390 nm that is enhanced with fluence intensity. The red shift of NBE emission with excitation is a known effect for semiconductors [34, 41]. This phenomenon might be due to shallow levels (on the order of 50 meV below the conduction band) that recombine directly with holes in the valence band. BL emissions in general are related to state levels which are particularly sensitive to temperature and irradiance conditions, while without stressing the system, they are basically negligible [42]. Indeed, the peculiarity of the NBE emission merits further study.

Table 3 Characteristic coefficients for TS

	k			τ_{eff} (μs)		
	TS1	TS2	TS3	TS1	TS2	TS3
Average	0.76	0.68	0.65	3.18	3.25	3.36
ZnO	0.59	0.52	0.54	5.01	5.23	6.04

k expresses the fluence dependence of intensity on fluence ($I = I_0 \cdot F^k$). Effective lifetime (τ_{eff}) is calculated following a non-linear fit of a three-exponential decay model in a selected spectral region window of 10 nm of width. Both k and τ_{eff} are evaluated for three different spectral bands: TS1 (490 nm), TS2 (530 nm) and TS3 (570 nm)

4.2 Historical zinc oxide

The PL emissions from our historical samples match results reported by others, which deal with the study of PL of zinc oxide as white pigment. In fact, we confirm the evidence of narrow peak at 390 nm and a broader green emission in region the 490–600 nm. Additionally, as explained in reference [16], the authors were able to detect a specific emission at 410 and 425 nm from localized spots at the sub-micrometre scale that was not achievable with our experimental set-up. The NBE PL emission of historical samples shows clear differences with respect to that observed in control ZnO in terms of emission mechanisms

as described below. The historical samples have a substantially higher effective lifetime value and an over-linear dependence of PL intensity on fluence with the value of the k coefficient smaller than the one retrieved in the control sample. These differences cannot be explained with reference to an increased number of competitive radiative and non-radiative recombination paths originating from the greater concentration of crystal defects expected in the less-perfect historical samples. In fact, it is well known that additional competitive paths give rise to a more rapid depopulation of the excited level (i.e. shorter lifetime) and to an increase in the k coefficient [43]. On the other hand, the increase in the lifetime of the NBE emission cannot be explained with the simple superposition of the optical emission from the organic matter present in historical samples, as the detected emission is still characterized by an over-linear dependence with the excitation intensity, which is typical of PL emission from semiconductors. Hence, it is supposed that the NBE emission, ascribed to free-exciton direct recombination in pure ZnO samples, follows a different near-band-edge emission mechanisms in historical samples, possibly introduced by the chemical interaction of the pigment with the organic binder and the formation of zinc carboxylates, which are well known to introduce characteristic groups on the surface of ZnO [43].

Regarding the PL emission ascribed to TS levels, as seen in control zinc oxide, the value of lifetime increases with increasing wavelength, while the k value decreases, as reported in Table 3. Hence, the same hypotheses advanced for the control sample can be drawn for historical samples. Indeed, the effective lifetime in historical sample was found to be smaller than that reported for the pure ZnO sample (with an average value of $\tau_{eff} = 3.26$ μs), whereas the k value in historical samples ($k = 0.70$) is in general greater than the k value for the control ZnO ($k = 0.54$). Shibata et al. [18] have demonstrated that with decreasing crystal lattice perfection of the samples, the value of k for the free-to-bound or donor–acceptor transitions is expected to increase. This reference suggests that in historical samples the TS emission is modified by the presence of increasing decay paths, which in this case can be related to the increased number of defects expected in historical samples.

5 Conclusion

In this work, we have shown how it is possible to provide clear insights into the emission mechanism of the zinc white pigment by analysis of the emission intensity as a function of the fluence and of the nanosecond and microsecond emission decay kinetic. With respect to traditional steady-state PL spectroscopy analysis, our approach provides valuable information for a clearer attribution of the emission paths that could be extended to the analysis of the wide class of semiconductor luminescent pigments. In the case of the selected historical samples, we report weak, but detectable modifications in the microsecond TS emission with respect to those observed in the control sample. These changes could be ascribed to a greater concentration of crystal defects, typically expected in samples produced with the imperfect synthesis and grinding processes available at the turn of the twentieth century. More interestingly, whereas the peculiar NBE emission of pure ZnO can be ascribed to direct free-exciton recombination, in historical samples, where ZnO is mixed with a complex organic matrix, the mechanism responsible for the NBE emission shows a substantial change. We hypothesize that the detected variations of the NBE emission in historical samples could also be influenced by the presence of zinc carboxylates, which are well known to introduce characteristic groups on the surface of ZnO particles [43]. Zinc stearate is usually associated with degradation process in painted layers, and its effect on the physical and chemical stability of oil paint layers is a major issue [44, 45]. To better investigate this issue, we plan to study the interaction binder pigments in artificially aged samples through the PL emission, to probe the photophysical effects of degradation.

Acknowledgements Authors wish to thank the Central European Research Infrastructure Consortium (CERIC-ERIC) for measurements and analyses of FE-SEM and Francesca Gherardi from Chemistry Department of Politecnico di Milano for measurements and analyses of FTIR spectroscopy. We are grateful to Lucia Toniolo from Chemistry Department of Politecnico di Milano for providing us historical samples. Research was partially funded by the Italian Ministry of Education, Universities and Research within the framework of the JPI Cultural Heritage JHEP Pilot call through the LeadART project 'Induced decay and ageing mechanisms in paintings: focus on interactions between lead and zinc white and organic material'.

References

1. G. Osmond, Zinc white a review of zinc oxide pigment properties and implications for stability in oil based paintings. AICCM Bull. **33**, 20–29 (2012)
2. G. Buxbaum, *Industrial Inorganic Pigments, 281* (VCH, Weinheim, 1993)
3. D.B. Faloon, *Zinc Oxide: History, Manufacture and Properties as a Pigment* (Van Nostrand, 1925)
4. A. Moezzi, A.M. McDonagh, M.B. Cortie, Zinc oxide particles: synthesis, properties and applications. Chem. Eng. J. **185186**, 1–22 (2012)
5. F. Casadio, V. Rose, High-resolution fluorescence mapping of impurities in historical zinc oxide pigments: hard X-ray nanoprobe applications to the paints of Pablo Picasso. Appl. Phys. A **111**, 18 (2013)
6. V. Capogrosso, F. Gabrieli, S. Bellei, L. Cartechini, A. Cesaratto, N. Trcera, F. Rosi, G. Valentini, D. Comellia, A. Nevin, An integrated approach based on micro-mapping analytical techniques for the detection of impurities in historical Zn-based white pigments. J. Anal. At. Spectrom. **30**, 828–838 (2015)

7. P.A. Rodnyi, I.V. Khodyuk, Optical and luminescence properties of zinc oxide (review). Opt. Spectrosc. **111**, 776–785 (2011)
8. U. Özgür, D. Hofstetter, H. Morkoc, ZnO devices and applications: a review of current status and future prospects. Proc. IEEE **98**(7), 1255–1268 (2010)
9. C.W. Litton, D.C. Reynolds, T.C. Collins, *Zinc Oxide Materials for Electronic and Optoelectronic Device Applications* (Wiley, Hoboken, 2011). doi:10.1002/9781119991038
10. Ü. Özgür, Y. Alivov, C. Liu, A. Teke, M.A. Reshchikov, S. Doğan, V. Avrutin, S. Cho, H. Morkoc, A comprehensive review of ZnO materials and devices. J. Appl. Phys. **98**, 041301 (2005)
11. A. Alkauskas, M.D. McCluskeyn, C.G. Van de Walle, Tutorial: defects in semiconductors—combining experiment and theory. J. Appl. Phys. **119**, 181101 (2016)
12. N.Y. Garces, L. Wang, L. Bai, N.C. Giles, L.E. Halliburton, G. Cantwell, Role of copper in the green luminescence from ZnO crystals. Appl. Phys. Lett. **81**, 622–624 (2002)
13. T.M. Børseth, B.G. Svensson, A.Y. Kuznetsov, P. Klason, Q.X. Zhao, M. Willander, Identification of oxygen and zinc vacancy optical signals in ZnO. Appl. Phys. Lett. **89**, 262112 (2006)
14. C. Clementi, F. Rosi, A. Romani, R. Vivani, B.G. Brunetti, C. Miliani, Photoluminescence properties of zinc oxide in paints: a study of the effect of self-absorption and passivation. Appl. Spectrosc. **66**, 1233–1241 (2012)
15. M. Thoury, J.P. Echard, M. Réfrégiers, B. Berrie, A. Nevin, F. Jamme, L. Bertrand, Synchrotron UV–visible multispectral luminescence microimaging of historical samples. Anal. Chem. **83**, 1737–1745 (2011)
16. L. Bertrand, M. Réfrégiers, B. Berrie, J.P. Échard, M. Thoury, A multiscalar photoluminescence approach to discriminate among semiconducting historical zinc white pigments. Analyst **138**, 4463–4469 (2013)
17. T. Schmidt, K. Lischka, W. Zulehner, Excitation-power dependence of the near-band-edge photoluminescence of semiconductors. Phys. Rev. B **45**, 8989–8994 (1992)
18. H. Shibata, M. Sakai, A. Yamada, K. Matsubara, K. Sakurai, H. Tampo, S. Ishizuka, K. Kim, S. Niki, Excitation-power dependence of free exciton photoluminescence of semiconductors. Jpn. J. Appl. Phys. **44**, 6113 (2005)
19. S. Lettieri, V. Capello, L. Santamaria, P. Maddalena, On quantitative analysis of interband recombination dynamics: theory and application to bulk ZnO. Appl. Phys. Lett. **103**, 241910 (2013)
20. S. Mosca, T. Frizzi, M. Pontone, R. Alberti, L. Bombelli, V. Capogrosso, A. Nevin, G. Valentini, D. Comelli, Identification of pigments in different layers of illuminated manuscripts by X-ray fluorescence mapping and Raman spectroscopy. Microchem. J. **124**, 775–784 (2016)
21. S.E.J. Bell, E.S.O. Bourguignon, A. Dennis, Analysis of luminescent samples using subtracted shifted Raman spectroscopy. Analyst **123**, 17291734 (1998). doi:10.1039/a802802h
22. I. Osticioli, J. Raman Spectrosc. **37**, 974980 (2006)
23. F. Rosi, M. Paolantoni, C. Clementi, B. Doherty, C. Miliani, B.G. Brunetti et al., Subtracted shifted Raman spectroscopy of organic dyes and lakes. J. Raman Spectrosc. **41**, 452458 (2010). doi:10.1002/jrs.2447
24. RRUFF Project website. http://rruff.info (2016)
25. Raman Spectroscopic Library. http://www.chem.uc.ac.uk/resources/raman (2016)
26. V.A. Solé, E. Papillon, M. Cotte, P.H. Walter, J. Susini, A multiplatform code for the analysis of energydispersive X-ray fluorescence spectra. J. Spectrochim. Acta B **62**, 6368 (2007)
27. D. Comelli, A. Nevin, A. Brambilla, I. Osticioli, G. Valentini, L. Toniolo, M. Fratelli, R. Cubeddu, On the discovery of an unusual luminescent pigment in Van Gogh's painting 'Les bretonnes et le pardon de pont Aven'. Appl. Phys. A **106**, 25–34 (2012)
28. G. Verri, C. Clementi, D. Comelli, S. Cather, F. Piqueé, Correction of ultraviolet-induced fluorescence spectra for the examination of polychromy. Appl. Spectrosc. **62**, 1295–1302 (2008)
29. G. Osmond, J.J. Boonc, L. Puskard, J. Drennana, Metal stearate distributions in modern artists' oil paints: surface and cross-sectional investigation of reference paint films using conventional and synchrotron infrared microspectroscopy. Appl Spectrosc. **66**, 1136–1144 (2012)
30. L. Robinet, M.C. Corbeil, The characterization of metal soaps. Stud. Conserv. **48**, 23–40 (2003)
31. J.J. Boon, J. van der Weerd, K. Keune, P. Noble, J. Wadum, Mechanical and chemical changes in old master paintings: dissolution, metal soap formation and remineralization processes in lead pigmented ground/intermediate paint layers of seventeenth century paintings, in *13th Triennial Meeting Rio de Janeiro 22–27 September 2002: ICOM Committee for Conservation*, ed. by R. Vontobel (James & James, London, 2002), pp. 401–406
32. E. Erdem, Microwave power, temperature, atmospheric and light dependence of intrinsic defects in ZnO nanoparticles: a study of electron paramagnetic resonance (EPR) spectroscopy. J. Alloys Compd. **605**, 34–44 (2014)
33. A.B. Djurišić, Y.H. Leung, Optical properties of ZnO nanostructures. Small **2**(8–9), 944–961 (2006). doi:10.1002/smll.200600134
34. N.S. Han, H.S. Shim, J.H. Seo, S.Y. Kim, S.M. Park, J.K. Song, Defect states of ZnO nanoparticles: discrimination by time-resolved photoluminescence spectroscopy. J. Appl. Phys. **107**, 084306 (2010)
35. K. Kodama, T. Uchino, Thermally activated below-band-gap excitation behind green photoluminescence in ZnO. J. Appl. Phys. **111**, 093525 (2012)
36. F. Fabbri, M. Villani, A. Catellani, A. Calzolari, G. Cicero, D. Calestani, G. Calestani, A. Zappettini, B. Dierre, T. Sekiguchi, G. Salviati, Zn vacancy induced green luminescence on non-polar surfaces in ZnO nanostructures. Sci. Rep. **4**, 5158 (2014)
37. J.V. Foreman, J.G. Simmons, W.E. Baughman, J. Liu, H.O. Everitt, Localized excitons mediate defect emission in ZnO powders. J. Appl. Phys. **113**, 133513 (2013)
38. Z.G. Wang, X.T. Zu, S. Zhu, L.M. Wang, Green luminescence originates from surface defects in ZnO nanoparticles. Phys. E Low-Dimens. Syst. Nanostruct. **35**, 199 (2006)
39. M. Lorenz, R. Johne, T. Nobis, H. Hochmuth, J. Lenzner, M. Grundmann, H.P.D. Schenk, S.I. Borenstain, A. Schon, C. Bekeny, T. Voss, J. Gutowski, Fast, high-efficiency, and homogeneous room-temperature cathodoluminescence of ZnO scintillator thin films on sapphire. Appl. Phys. Lett. **89**, 243510 (2006)
40. C. Ton-That, L. Weston, M.R. Phillips, Characteristics of point defects in the green luminescence from Zn- and O-rich ZnO. Phys. Rev. B **86**, 115–205 (2012)
41. S.A. Studenikin, M. Cocivera, Time-resolved luminescence and photoconductivity of polycrystalline ZnO films. J. Appl. Phys. **91**, 5060–5065 (2002)
42. B.K. Meyer, H. Alves, D.M. Hofmann, W. Kriegseis, D. Forster, F. Bertram, J. Christen, A. Hoffmann, M. Strassburg, M. Dworzak, U. Haboeck, A.V. Rodina, Bound exciton and donor-acceptor pair recombinations in ZnO. Phys. Stat. Sol. **241**, 231–260 (2004)
43. A.K. Radzimska, T. Jesionowski, Zinc oxide—from synthesis to application: a review. Materials **7**, 2833–2881 (2014)
44. J.J. Hermans, K. Keune, A. Van Loon, P.D. Iedema, An infrared spectroscopic study of the nature of zinc carboxylates in oil paintings. J. Anal. At. Spectrom. **30**, 1600–1608 (2015)
45. G. Osmond, B. Ebert, J. Drennan, Zinc oxide-centred deterioration in 20th century Vietnamese paintings by Nguyen Trong Kiem (19331991). AICCM Bull. **34**, 4 (2014)